ISTANBUL TECHNICAL UNIVERSITY ★ GRADUATE SCHOOL

IN-FLANGE DEROTATOR DESIGN AND CONTROL

M.Sc. THESIS

Ali Cem ÜNAL

Department of Mechanical Engineering

System Dynamics and Control

DECEMBER 2020

ISTANBUL TECHNICAL UNIVERSITY ★ GRADUATE SCHOOL

IN-FLANGE DEROTATOR DESIGN AND CONTROL

M.Sc. THESIS

Ali Cem ÜNAL
(503171624)

Department of Mechanical Engineering

System Dynamics and Control Program

Thesis Advisor: Prof. Dr. İlker Murta KOÇ

DECEMBER 2020

ISTANBUL TEKNİK ÜNİVERSİTESİ ★ LİSANSÜSTÜ EĞİTİM ENSTİTÜSÜ

FLANŞ İÇİ DEROTATOR TASARIMI VE KONTROLÜ

YÜKSEK LİSANS TEZİ

Ali Cem ÜNAL
(503171624)

Makina Mühendisliği Anabilim Dalı

Sistem Dinamiği ve Kontrol Programı

Tez Danışmanı: Prof. Dr. İlker Murat KOÇ

ARALIK 2020

Ali Cem Ünal, a M.Sc. student of İTU Graduate School student ID 503171624, successfully defended the thesis/dissertation entitled “IN FLANGE DEROTATOR DESIGN and CONTROL”, which he/she prepared after fulfilling the requirements specified in the associated legislations, before the jury whose signatures are below.

Thesis Advisor :	**Prof. Dr. İlker Murat KOÇ** İstanbul Technical University	.....
Jury Members :	**Prof. Dr. İlker Murat KOÇ** Istanbul Technical University	.....
	Assoc. Prof. Dr. Ayhan KURAL Istanbul Technical University	.....
	Dr. Onur KESKİN Isik University	.....

Date of Submission : 03 December 2020
Date of Defense : 21 December 2020

To my family,

FOREWORD

I would like to represent my gratitude to Prof. Dr. İlker Murat KOÇ for leading me during the thesis period and his excellent academical guidance during my graduate study.

I would like to express my special thanks to Assist. Prof. Onur Keskin for believing in and supporting my academic work, and supplying ever possible facility for me.

I am thankful to Presidency of the Republic of Turkey Presidential Strategy and Budget (Undersecretariat of state planning organization) for their vision.

I wish to express my gratitude to Atatürk University Astrophysics Research and Application Center (ATASAM) and director of the center Dr. Cahit Yes¸ilyaprak. for their support.

Finally, I would like to thank my parents who always have been there for me, unconditionally.

December 2020 Ali Cem ÜNAL

TABLE OF CONTENTS

Page

ABBREVIATIONS

M1, M2, M3 **:** Respectively: first, second and third telescope mirrors

M_1, M_2, M_3 **:** Respectively: first, second and third derotator mirrors

M_{13} **:** Used to call the monobloc of M_1 and M_3

FoV **:** Considered field of view

2D, 3D **:** To spot the difference between plane ray tracing (2D) and space ray tracing (3D)

DAG **:** Turkish acronym for Eastern Anatolia Observatory (Dogu Anadolu Gözlemevi)

Lat **:** DAG telescope latitude

CF **:** Carbon fiber

DoF **:** Degree(s) of Freedom

X, Y, Z **:** Derotator reference axis (telescope axis)

FEM **:** Finite element method

aO **:** Active optics

AO **:** Adaptive optics

SYMBOLS

$\mathbf{T_{earth}}$	**:** Respectively: earth rotation period in s and its rotational speed in rad/s
$\boldsymbol{\omega_{DRT}}$	**:** Derotator rotational speed in rad/s
$\boldsymbol{\omega_{FoV}}$	**:** Field of view rotational speed in rad/s
CTE, α	**:** Coefficient of Thermal Expansion in ˚C
Alt	**:** Altitude angle in rad
Az	**:** Azimuth angle in rad
dx	**:** Displacement error along X axis
dy	**:** Displacement error along Y axis
rx	**:** Angular misalignment around X axis in rad
ry	**:** Angular misalignment around Y axis in rad
ρ	**:** Density in kg/m^3
E	**:** Young modulus in N/mm^2
ν	**:** Poisson's ratio

LIST OF TABLES

Page

LIST OF FIGURES

Page

IN-FLANGE DEROTATOR DESIGN AND CONTROL

SUMMARY

The field rotation effect can be described as observing the gyration of an object with the pupil of a telescope around the optical axis under the influence of the latitude of the observatory while the telescope is following that astronomical object. This is possible as a result of the alt-azimuthal mount of the telescope.

It is essential to correct and compensate the rotation of the optical field caused by the earth's rotation during the monitoring of the astronomical object. The image can be rotated electronically in many devices. If the image rotated electronically, some pixels are loose and some parts are blurred on the final image. Since every pixel carries important information, such operation is not convenient. This problem is solved by rotating the image mechanically before it reaches to the camera.

Derotator is a class of devices that is used to correct the optical field rotation. In a telescope of a Ritchey-Chretien, Nasmyth configuration, the device must be integrated between the scientific instruments and the M3 mirror. Derotator class devices are categorized by their sizes, mirror configurations and their locations. This study is about K-mirror configuration, cantilever design and in flange located field derotator.

Cost of the free space on the Nasmyth platform and the derotators for each scientific instrument are very important, integrating one derotator in the central hole of the telescope fork is important for both technologically and economically. This study shows the designing and controlling an in-flange field derotator which is designed for a 4m altitude-azimuth type ground telescope.

In this way, optical configuration of the device is selected for maximizin field of view. Mirror sizing is done by ray tracing method and maximum mirror sizes are found according to the available space. A special method is used for lightweighting the mirrors. Semi-kinematic joints are designed for mirrors. These joints prevent creating internal stress for the mirrors. Micrometers are adapted to the joints for accomplishing alignment.

Material selection is done by using Ashby cahrts. Materials are eliminated with the help of the filtering such as availability, cost and manufacturability. A cad design is developed regarding the technical specifications. Housing panels are optimized in the cad desing for minimum deflection. Center of gravity is shifted for the optimum location.

The cad design is improved by using Ansys. Iteration method is used in order to achieve optimum mechanical model. Full system is analyzed, all deflection and internal stresses are controlled. Since the working temperature has 30°C ΔT, materials compatibility is verified. The alignment procedure is developed. The control system is developed in the light of the available telescope documents. Performance of the controller is tested for 2 different temperatures, 2 diffrenet loading case and 7 diffrenet speeds. The results are presented by simulations.

FLANŞ İÇİ DEROTATOR TASARIMI VE KONTROLÜ

ÖZET

Teleskop astronomik bir nesneyi takip ederken, teleskopun coğrafi koordinatına ve nesnenin gökyüzü koordinatına bağlı olan optik eksen etrafında nesnenin döndüğünü görür. Bu etkiye alan dönüşü denir ve alt-azimut konfigurasyonunda olan teleskoplarda bu etkiyi görmek mümkündür.

Astronomik gözlem için bir nesnenin izlenmesi sırasında dünyanın dönüşünden kaynaklanan optik alanın dönüşünü düzeltmek ve telafi etmek esastır. Eğer bu etki düzeltilmeden görüntü teleskop kamerasına iletilirse, uzun pozlama yapılan durumda çıktı görüntüsünde bulanık alanlar meydana gelir ve bilimsel araştırmalar açısından kabul edilemez olur. Elde edilen her bir karenin dijital olarak döndürülme olanağı da vardır. Fakat dijital olarak döndürülen görüntülerde piksel kayıpları ve bulanık alanlara rastlanacağı için çıktı görüntüsünde bilgi kayıpları meydana gelir. Her bir piksel bilgi taşıdığı için bulanık veya kayıp piksel durumları da bilimsel araştırmalar açısından kabul edilemez durumlardır. Karşılaşılan bu problemin çözümü görüntüyü mekanik olarak döndürmektir.

Derotator, optik alan dönüşünü düzeltmek için kullanılan bir cihaz sınıfıdır. Kendi içerisinde ayna kombinasyonuna, cihazın boyutlarına, yapısına ve yerleştirildiği konuma göre sınıflara ayrılır. Nasmyth konfigürasyonu olan bir Ritchey-Chretien teleskopunda, böyle bir cihaz bilimsel aletler ile M3 aynası arasına entegre edilmelidir. Bu teze konu olan derotator ise, ankastre tasarıma sahip olup K tipi ayna dizilimine sahiptir. Konumlandırıldığı yer ise teleskop çatalının içidir.

Nazmit platformundaki boş alanlar çok kıymetlidir. Eğer her bir bilimsel ekipmanın girişine bir mini derotator koyarsanız hem alan maliyetiniz artar hem de her cihazın derotatorları için bir para ödemis¸ olursunuz. Eğer teleskop merkezi deliğine bir derotator entegre ederseniz ve görüntüyü bilimsel ekipmanlara bu şekilde yollanması hem teknolojik hem de ekonomik açıdan önemlidir. Bu çalışma, 4m altitude-azimut tipindeki DAG teleskopu için tasarlanmıs¸ flanş içi derotator tasarımını ve kontrolünü göstermektedir.

DAG Teleskobu gözlemevi binası Erzurum Karakaya tepelerinde yer almaktadır. Buradaki rakım olarak 3170 metredir ve meteorolojik bulgular doğrultusunda astronomik gözlem açısından oldukça elverişlidir. Burada dünyada sayılı coğrafyada yapılabilen kızılötesi bölgede gözlem yapılabilmektedir. DAG Teleskobu görsel ve yakın kızılötesi dalgaboylarını kapsayacak şekilde gözlem yapabilme yeteneğine sahiptir. En büyük aynasının çapı 4 metredir. Bu boyutlar ile Türkiye'de yer alan en büyük teleskoptur ve boyutları açısından değerlendirildiğinde ise orta boy teleskop sınıfına girer.

Teleskonun yeteneklerini arttıran en önemli özelliklerden bir tanesi de adaptif optik sisteme sahip olmasıdır. Bu sistem atmosferdeki türbülans etkilerini çok büyük oranda ortadan kaldırmak amacıyla tasarlanmıştır. Bu etkiler basit olarak şöyle açıklanabilir;

bulunduğunuz konumdan uzak bir noktaya baktığınızda gözlemnen nokta ile gözlemci arasında bir sıcak hava haraketi varsa gözlemci gözlemlediği noktayı bulanık görür. Haraket eden hava gözlemlenen noktadan gelen ışığı kırar ve gözlemciye bozuk görüntü ulaşır. Adaptif optik sistemi ileri teknoloji optik teknikler sayesinde bu kırılmaları büyük oranda düzelterek türbülansın etkilerini ortadan kaldırır. Böylece, teleskobun kamerasındaki görüntü atmosfer dışında yer alan uzay teleskoplarının topladığı görüntüye benzer olur. Dag teleskobunda kullanılan bir başka ileri teknoloji ürünü ise bu tezin konusu olan flanş içi derotatordür.

Derotator tasarlanırken ilk olarak cihazın optik konfigürasyonuna karar verildi. Derotatorun yerleştirileceği yer açısından sabit faktör olarak ankastre tasarıma sahip olması gerekiyor olmasıdır. Bu tasarım şartı sebebi ile bir kaç optik konfigürasyon elendi. Optik düzen açısından eleme sonucunda en önemli adaylar Dove prizması ve K tipi ayna yerleşimidir. Ankastre tasarım sonucu sistemde sehim oluşumu kaçınılmazdır. Bu durum cihazın tasarımında tanımlanacak olan serbestlik derecesinin önemini arttırmıştır. Daha fazla serbestlik derecesi elde edebilme açısından ve daha hafif yapısı sebebiyle K tipi ayna yerleşimi tercih edilmiştir.

Ayna yerleşimi belirlendikten sonraki aşamada cihazın görüş alanını en üst seviyede tutabilmek için mevcut alana göre ayna boyutlandırması yapılmıştır. Boyutlandırmadaki amaç ayna yüzeyini olabildiğince arttırmaktır. Ayna boyutlandırması 2 boyutlu ışın izleme yöntemi kullanılılarak yapılmıştır. Bu aşamada Matlab program kullanılmıştır. Teleskop tarafından gelen ışığın çapı teknik şartnamede belirlendiği gibi sabittir. Işın izleme yöntemi ile belirlenen alana konulabilecek ayna boyutları belirlenmiş ve derotator çıkışındaki görüş alanı hesaplanmıştır.

2 boyutlu ışın izleme yöntemi basit olarak şöyle tarif edilebilir; giriş tarafındaki aynanın kritik noktalarına ışın göndererek yansıması hesaplanır. Yansıyan ışınları karşılayabilecek boyutta bir ayna seçilir. Eğer ikinci ayna belirlenen alana sığmıyorsa birinci aynanın açısı veya boyutları değiştirilir. İkinci aynadan yansıyan ışınlar hesaplanır ve üçüncü aynanın yeri ve oryantasyonu belirenir. Eğer üçüncü ayna belirlenen alana sığmıyorsa ikinci ve birinci aynalar tekrar ayarlanır. Son olarak, üçüncü aynadan çıkan yansıma hesaplanır. Bu yansımanın çapı görüş açısını belirler. Tasarlanan derotatorün görüş açısı 7 ark saniyesidir. Böylece aynaların oryantasyonları ve büyüklükleri belirlenmiş olur.

Boyutlandırılan aynalar rijit yapısını koruması çok önemlidir. Ayna yüzeyindeki deformasyonlar yansıyan ışınların yönlerini değiştireceğinden, çıkış tarafında elde edilen görüntünün kalitesini ve görüş açısını direkt olarak etkiler. Bu etkiler göz önünde bulundurularak aynalar özel bir yöntemle hafifletilmiştir. Böylece aynaların kendi ağırlı sebebiyle oluşan yüzey deformasyonu azaltılmıştır. Ayrıca, ankastre dizayna sahip olan derotator gövdesine daha az yük eyki edeceği için gövdenin sehimi de azalmıştır.

Ayna üzerindeki bir başka önemli nokta ise sıcaklık değişimidir. Aynaların malzemesi sıcaklık değişimlerinden en az etkilenecek şekilde seçilmiştir. Endüstride en çok kullanılan Zerodur isimli malzeme seçilmiştir. Bu malzeme oldukça rijit bir yapıya sahiptir ve aynaların üretimi açısından talaşlı imalata uygun bir malzemedir. CTE değeri çok düşük olduğundan derotatorün çalışma sıcaklığı göz önüne alındığında şekil değiştirmesi göz ardı edilebilecek kadar az miktardadır. Böylece aynadan geçen görüntünün bozulması olabilecek en az seviyeye indirgenmiştir.

Aynaların altına özel bir yapıştırıcı ile peddler yapıştırılmıştır. M1 ve M3 aynalarında bu pedler içerisinde mikrometre de bulunan yarı kinematic eklemleri oluşturur. Aynaların altında 3 adet ped bulunur. Her bir pedin yüzey tasarımı farklıdır; düz noktasal delik ve v kanalı şeklinde şekillere sahiptirler. Bu farklı şekillerin her biri farklı bir eksende serbestlik derecesi verir. Böylece aynalara sıcaklık farkından oluşan boyut değişimleri sebebiyle meydana gelen gerilmeler iletilmez.

Eklem sisteminde yer alan mikrometreler pedleri iter ve sistemde kullanılan 3 adet yay karşı kuvvet oluşturur. Böylece ped ve mikrometre ucundaki küre arasında büyük bir sürtünme kuvveti meydana gelir. Aynalar yere 90 derece açıyla durduğu pozisyonda bile yer çekimi etkisinden kaynaklı haraketlerin önüne geçilmiş olur. Mikrometreler ayrıca aynaların oryantasyonlarını ayarlamaya yardımcı olur.

M2 aynasıda ped sistemi vardır fakat mikrometreler yoktur. Bu ayna taşıyıcı paneline klemp ile bağlıdır. Bu paneller de gövdeye 3 ayrı mikrometre ile bağlıdır. Bir önceki paragrafta anlatılan sistemden tek farkı boyut olarak daha büyük olmasıdır. Ayrıca, M1 ve M3 aynalarının taşıyıcısı da aynı yöntemle gövdeye bağlanır. Toplamda 12 adet mikrometreli sistem yer almaktadir. Bunalrın üçü M1 aynasının altında, üçü M3 aynasının altında, üçü M2 aynasının taşıyıcısında ve son üçü de M1 ve M3 aynalarının taşıyıcısında yer alır.

Taşıyıcı paneller ve gövde karbonfiber kompozit panellerden oluşmaktadır. Kompozit panellerin içi bal peteği şeklinde alüminyum malzemeden mal edilmiştir. Optik hassasiyeti koruyabilmek için panellere açı verilmemiştir ve yüksek hassasiyette imal edilmişlerdir. Bu düz panaller birbirlerine vida bağı ile bağlanırlar. Gövdenin tasarımında atalet momentleri göz önüne alınmış ve derotatorün taradığı her açıda dik konuma yakın duracak şekilde en az bir panel denk getirilmiştir. Böylece gövdenin sehimi azaltılmıştır.

Tasarım bilgisayarlı katı model yardımıyla yapılmıştır. Olabildiğince az parça ve hafifletilmiş parçalar kullanılmıştır. Ağırlık merkezi bilgisayarlı katı model yardımıyla en ideal konuma kaydırılmıştır. Tasarım aşamasında üretim sonrası montaj ve hizalama konuları da göz önünde bulundurulmuştur. Gövdenin kapakları çıkarılıp takılabilir şekilde dizayn edilmiştir.

Malzemelerin bulunabilirlik, maliyet ve üretilebilirlik açısından filtrelenmesi ile malzeme seçimi yapılmıştır. Temas halinde olan parçaların malzemelerinin CTE değerlerinin uyumluluğuna dikkat edilmiştir. Örneğin yarı kimetaik eklem sisteminde invar kullanılmıştır ve karşıt ağırlık yapı çeliği seçilmiştir.

Cihazın ayarlanma kabiliyetini arttıkmak için ayar flanşı eklenmiştir. Bu flanş yere parallel ve dikey eksenlerde öteleme haraketi yapabilmektedir. Bu haraketi farklı diş özelliklerine sahip vidalar ile yapabilmektedir. Ayrıca ayar flanşını taşıyıcı flanşa bağlayan 3 adet küresel yatak sistemi vardır. Böylece ayar flanşının referans yüzey ile arasındaki açı ayarlanabilmektedir.

Bilgisayarlı katı model tasarımı Ansys programı kullanılarak geliştirilmiştir. Tasarımı en uygun şekilde hafifletebilmek için iterasyon yöntemi kullanılmıştır. Çalışma sıcaklığı 30^0C ΔT değerlere sahip olduğu için malzeme uyumluluğu Ansys ile doğrulanmıştır. Optik hizalama ve ayarlama prosedürü geliştirilmiştir. Kontrol sistemi, mevcut teleskop belgeleri ışığında geliştirilmiştir. Kontrolcünün performansını görebilmek için benzetim yöntemiyle görseller hazırlanmıştır ve 21 adet deney yapılmıştır.

1. INTRODUCTION

In astronomical observations, the exposure time varies. In order to get a detailed observation on the science target, astronomers prefer long exposure to gather all possible data from the target celestial object. The fact that the EMCCDs frame rate are above 1kHz; the image gathered results in a superposition of the images during the observation (due to the star's trajectory and the earth's rotation). Thus, the final image results in an elliptical shape rather than a circle; derotator, by compensating between the trajectory and Earth's rotational effects, eliminates this effect and provides with the real shape of the target.

1.1 Purpose of Thesis

The purpose of this thesis is designing and controlling an in flange optical field derotator system for 4 meters DAG Telescope. In-Flange Derotator KORAY (K-mirror OpticalRelAY) is designed, analysed and manufactured to meet the specifications of DAG telescope. DAG telescope, situated at Erzurum/Karakaya summit at 3150m altitude, is the first Turkish optical telescope with VIS(Visible) and IR (Infrared) observation capability. DAG, designed by Turkish engineers at FMV Isik University, is also the largest telescope (4m diameter) in Turkey and in European continent. Being one of the 2023 vision projects; the first light of DAG is expected to take place in 2021. This purpose brings some real-life challenges such as design limitations, material selection, budget, electronic integration. The study explains design steps and solution of the challenges.

1.2 Literature Review

Derotator systems are the known devices in astronomy and optics. The idea is coming out on 1955 [1]. It was used for measuring the contrast rendition of optical systems. Then the first patent about this topic is giving on 1957 [2]. The idea is improved during

years and derotator is adapted to another systems. In the year 1978 derotator was used for hologram interferometry and speckle photography of rotating objects [3].

The image can be rotated digitally after camera capture it. For instance, it can be done with even cellphones. However, it is not possible yet for some cases. Ground based optical telescopes are using very complex imaging systems. If the image is rotated after it captured, there will be data loss and it is not sufficient way for scientific researches. Derotators mechanically rotates the image before it captured. This is the way the problem is solving even today. There are different optical configurations for derotators such as delta prism [4], dove prism [5] ...

K-miror configuration can be categorized by the location of the derotator. ELT telescope has a big size derotator and it is placed on the nasmyth playform of the telescope [6]. Small derotators can be placed on the optical tables, before the scientific instruments. This study is about the k-mirror design derotator which is placed in the telescope fork hole.

The idea of manufacturing an in flange derotator to serve all astrophysical instrumentation on the Nasmyth Platform of DAG telescope was published on 2018 [7] by team that I am part of as a full-time engineer at OPAM (FMV Isik University Center for Optomechatronics Research & Application Commercial Enterprize). It is a unique idea because it has never been done before. There are patent applications which are waiting for release; eu EP18020210.3, eu EP180202209.5, PCT/IB2019/054009.

1.3 The Dag Telescope

Astronomical observations have been conducted by the faculty at Erzurum Atatürk University Turkey since 2007. The first project was the development of a scientific research 50 cm diameter telescope. As the studies and observations return good results, building a larger telescope is decided (4m in diameter)[1]. Since then, the DAG project (Dogu Anadolu Gözlemevi, East-Anatolian Observatory) was born. Seeing[2] [8]

[1] The advantage of a larger telescope diameter is the fact that it can receive much more amount of light. Indeed, this quantity is proportional to the surface of the entrance pupil, that is to say to the diameter of the primary mirror M1.

[2] The seeing is the value of the mid-height width of the point spreading function (PSF) which indicates how much a point image of a star is spread. The usual measuring unit of seeing is second of arc.

measurements are undertaken on the Karakaya site since February 2010, then in January 2012 the DAG project is accepted by the Turkish government.

a) b)

Figure 1.1: a) Observatory Location b) visual from site

The optical design is done by the collaboration of OPAM and HEIG-VD (Haute Ecole d'Ingénierie et de Gestion du Canton de Vaud /Switzerland) and the telescope tender was appointed to AMOS. AMOS is a company specialized in the design of devices and systems Opto-mechanics, in fields such as astronomy and space. The telescope Factory Acceptance Tests are performed on November 2019, the transportation is expected to take place by December 2020, and the first light is expected to take place on the last quarter of 2021.

1.3.1 Optical configuration

In order to avoid spherical and coma aberrations, the optical configuration is based on the Ritchey-Christian type, that is why the primary mirror (M1) and the mirror (M2) are hyperbolic. This type of telescope is particularly suitable for wide field observation. Its design is relatively compact and its off-axis performance are excellent. However, this type of telescope is relatively rare due to the high cost of manufacturing the primary mirror. The Ritchey-Chrétien design is mainly found in professional observatories such as the Keck, VLT, Gemini observatories or some space telescopes such as Hubble or Herschel.

1.3.2 Types of Mounting

It is good to mention basis of the telescopes before going deeper. There are two main types of mountings[3]; the alt-azimuthal and the equatorial.

[3] The type of mounting is the way the telescope tube can be oriented, or the arrangement of its motion axes.

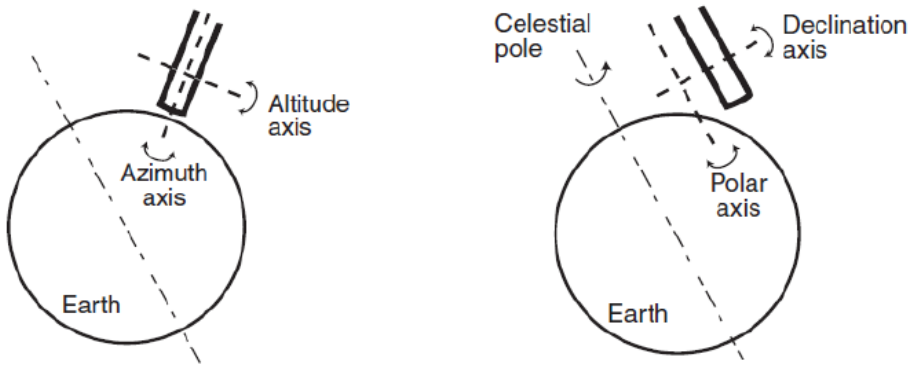

a) b)

Figure 1.2: a) Alt-azimuth mounth and b) equotorial mounth

The main advantage of alt-azimuthal mount is its simplicity for implementation and it is often used for large telescopes. However, it is necessary to slave the two-telescope axis for compensation rotation of the earth (altitude axis as well as the azimuth axis). In addition, the alt-azimuthal mount induces a rotation of the observed field[4].

The equatorial mount offers a considerable advantage; because the polar axis is parallel to the axis of rotation of the earth, it is sufficient to only slave the polar axis when the declination axis is fixed to compensate the effect of the rotation of the earth. Therefore, there is no rotation of the field. On the other hand, the assembly is substantially larger, and therefore more expensive for a given mirror diameter. This type of mounting is often reserved for modest sized telescopes.

From the point of view of the observer (figure 1.3), it can be seen that with an alt-azimuthal mount, the trajectory of the star follows a curve. In fact, while following the star along its trajectory, the azimuth movement must be synchronized with the elevation. In addition, the driving speed is variable and depends on the position on the celestial vault, or the direction of sight of the telescope.

With an equatorial mount, because one of the axes (the polar axis) is collinear with the axis of the celestial north pole, the trajectory of the star looks like a horizontal line. Once the declination is fixed, only the right ascension must be slaved in position at the constant angular velocity of one revolution for 24 hours.

[4] The phenomenon will be explained in the next section.

1.3.3 Telescope characteristics

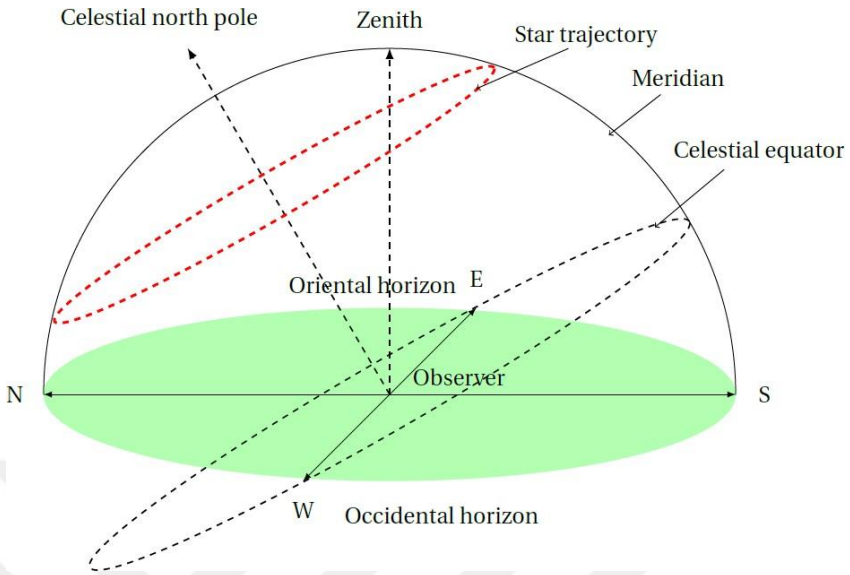

Figure 1.3: 3D representation of stars observation

As it can be seen on the figure 1.4, the DAG telescope has an alt-azimuthal mount. Its configuration is Nasmyth type. In other words, the flat telescope mirror M3 is placed along the optical axis at the height of the elevation axis of the telescope. That allows to send the beam to a Nasmyth platform or to the other.

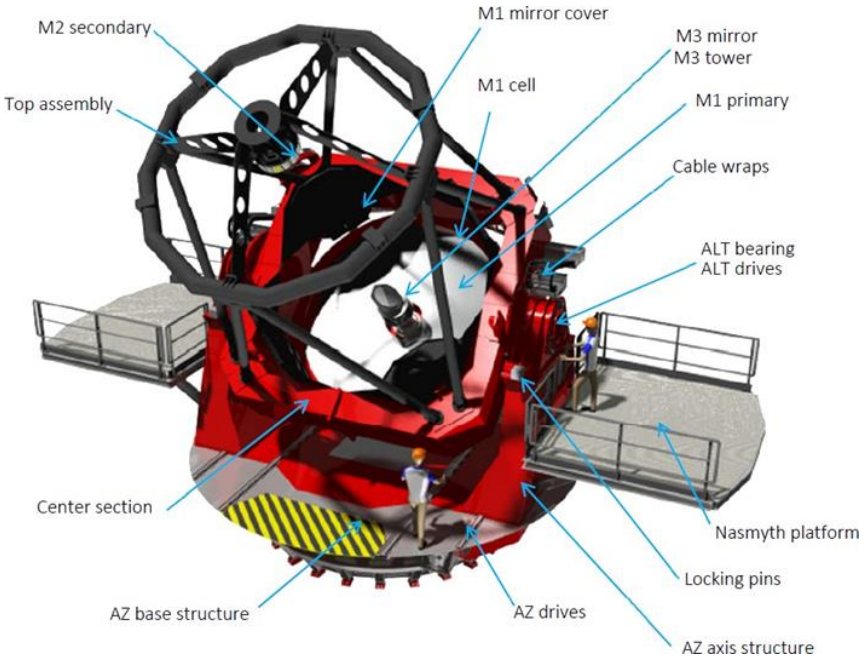

Figure 1.4: DAG telescope

The main mirror has a diameter of 4 m and a focal length of 56 m. In order to compensate for the aberrations of the wavefront due to atmospheric perturbations, the DAG is equipped with an adaptive optics system under the appointed tender to OPAM. The national adaptive optics system that is built and successfully delivered to ATASAM is called "TROIA" that stands for "TuRkish adaptive Optics system for Infrared Astronomy" (AO)[5] [8]. An active optics system (aO)[6] is used on M1 to compensate the main deformations (weight of elements, vibration, bending). The availability of both aO and AO makes DAG unique in the world at 4m class telescope league. The DAG Telescope can be seen on figure 1.4. The telescope is composed of two platforms on both sides of the fork. The design is implemented for the ability of reversing the M3 position via a special hexapode (built to accommodate M3) and send the beam to the other side of the fork. This feature makes possible to have two foci. They can be sent to two platforms which are equipped with different instruments.

The telescope is designed to work in the visible as well as in the infrared (IR) side. One of the foci is be adapted to a field up to 7 arcmin and it is be equipped with the derotator which is the object of this report and also it is used for observations up to a field of 24 arcmin.

1.4 Observation of Astronomical Objects

1.4.1 Optical beam rotation

The first thing to do is keeping the celestial object stationary with respect to the sensor which is tracking the celestial object. For the DAG Telescope, it is achieved by having position control of the telescope motors[7]. Motor control is carried out by control electronics and software in order to process the regulation from the target object or from a guide star[8].

---

[5] In astronomy, adaptive optics is the system that compensate the noise due to atmospheric disturbances.

[6] Active Optics compensates for the gravity effects of the telescope during alt-azimuthal movements.

[7] Control of elevation and azimuth.

[8] The observed celestial object is not necessarily visible to the naked eye. the bright star is used as a target, compensate the atmospheric optical aberrations with the adaptive optics system in order to sharpen the image and compensate for the aberrations.

During the monitoring operation, it can be seen that, the observed object rotates around the optical axis. Thediagram figure 1.5 shows this effect. The result of this rotation is highlighted on figure 1.6 where the observed object rotates with respect to the frame. The final rendering of such an acquisition is not exploitable because the final image is blurred (similar to a "shake" in photography).

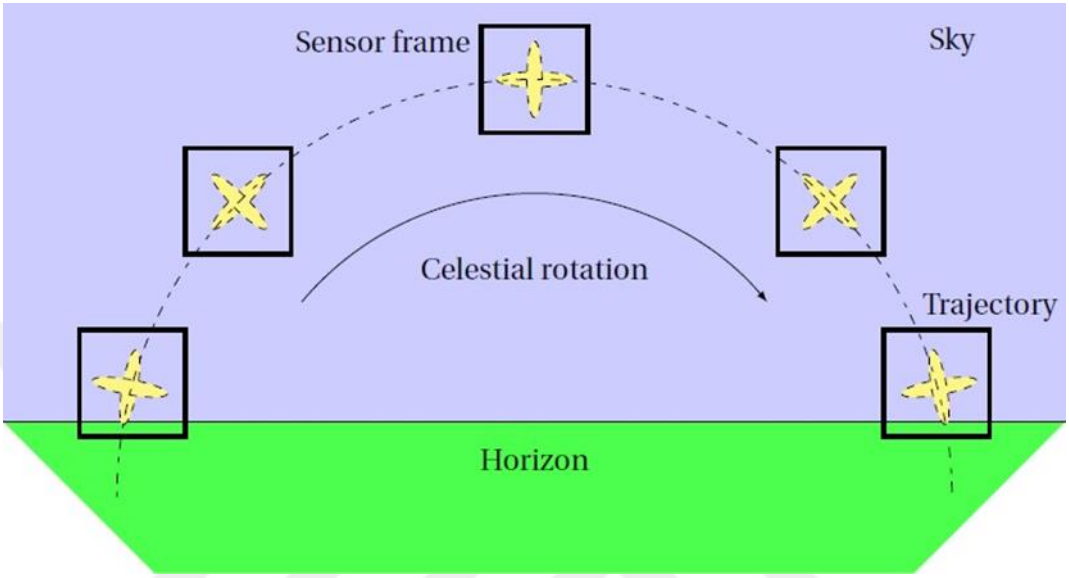

Figure 1.5: Observation of a celestial object

The image on the sensor can be described also.

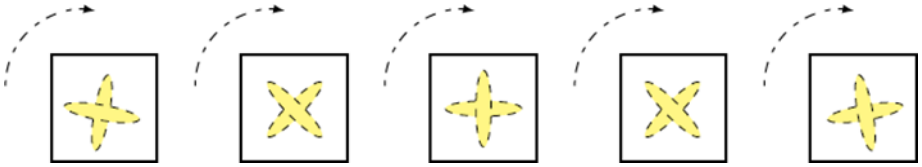

Figure 1.6: Object rotation in the sensor frame

The derotation, which is the subject of the next section, is the compensation of this earth rotation effect during an alt-azimuthal observation.

1.5 The Field Derotator

The concept of derotation is compensating the object rotation by placing a field derotator before the optical instruments. This field derotator rotates in the opposite way, so it immobilizes the image with respect to the sensor.

There are several solutions to rotate an optical beam. Here is a non-exhaustive list of the main systems used:

- **Rotation of the sensor:** This solution is mainly used for Cassegrain telescopes where the light is not sent to the Nasmyth planform but focused at the back of the M1 mirror allowing a single astrophysical instrument to perform scientific. This solution was not considered for DAG Telescope, because several instruments are installed on the Nasmyth platform. As the mechanical rotation requires physical attachment of the instruments to the telescope flange, this solution is obsolete for DAG.
- **Opto-mechanical derotation (K-mirror or Dove prism):** This solution is used to obtain the derotation of the image before reaching the scientific instruments. This technique has the advantage of not turning all the instruments and providing scientific observation capability to multiple instruments at the same time. It cna be said that the design is convenient for large telescopes.
- **Digital derotation (image processing):** This solution is the simplest one for implementation. Yet, this solution is not only resulting with a loss of resolution due to interpolation of the pixels, but also the fine scientific details of the image would disappear around the target object. Thus, it is limiting the ability of the instrumentation that cost millions of Euros (DAG telescope's extremely sensitive scientific instrumentation only at the IR Nasmyth platform is in the order of 11 M Euros). This solution was not considered for DAG Telescope because an optical derotation is needed in order to send the beam for multiple instruments.

1.5.1 State of the art

This section presents possible solutions for the derotation. After some researches on the subject, it has been found that the most common way to derotate is using prisms or mirrors.

1.5.1.1 Roof/Dove prism

The beam refracts on the input face, reflects on the hypotenuse face, then refracts again on the output face. A practical way of evaluating the optical effect of a Dove prism derotator is to unfold it to obtain the "tunnel diagram" of the prism (1.7). It can be seen

that; the prism is optically equivalent to a thick block rotated at least 45^0 with respect to the beam.

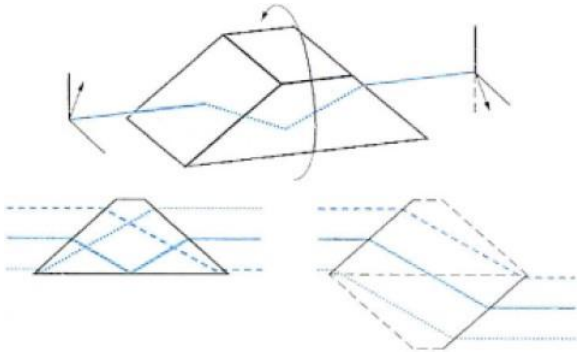

Figure 1.7: The Dove prism and its tunnel diagram [14]

An in-line optical derotator causes an image rotation of twice the speed of the derotator. This effect comes from the fact that this system is equivalent of a reflection on a flat mirror in rotation. Hence, in our case, the derotator must rotate in counterwise at half the speed of the field of view. Any optical system that causes an image inversion from top to bottom without inversion from left to right can be used as a derotator. The rotational speed of the field of view/derotator is the subject of the section 10.1.

1.5.1.2 Other prisms derotation techniques

There are several other prisms that can be used for field rotation. Here are a few examples.

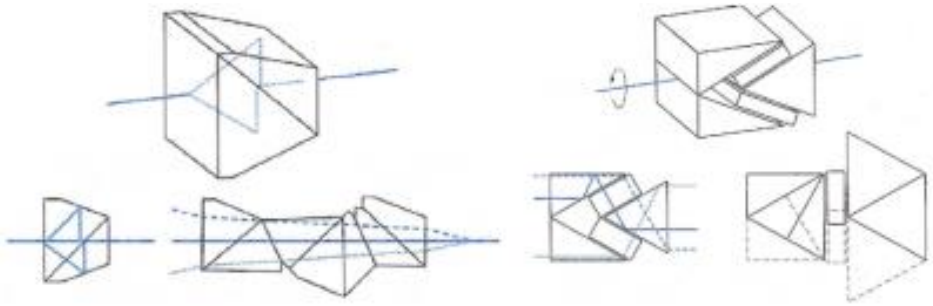

Figure 1.8: Pechan prism (left) and Rantsch prism (right) [14]

Since the beam is convergent, prism derotators would generate astigmatism and chromatism. This technique is therefore discarded.

1.5.1.3 The mirror derotator

Another interesting alternative is the mirror derotator. It has the advantage of being achromatic. However, it is not adapted to the design of the DAG because of its mechanical configuration. Further information about this device can be found in the reference [14].

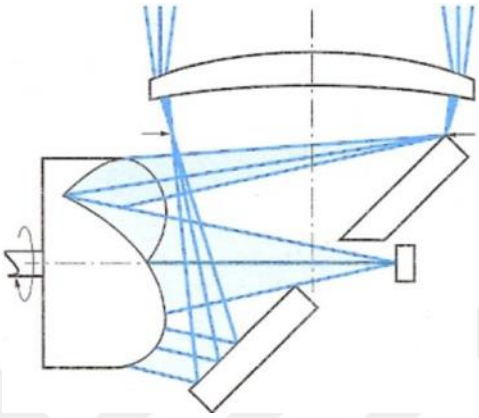

Figure 1.9: The mirror Derotator [14]

1.5.1.4 The k-mirror

The figure 1.10 shows the K-mirror principle. On this ray tracing, as for the prisms used for derotation, it is observed that the output image is inverted with respect to the object. This inversion is true only for the vertical direction. For the horizontal direction, the image is not reversed.

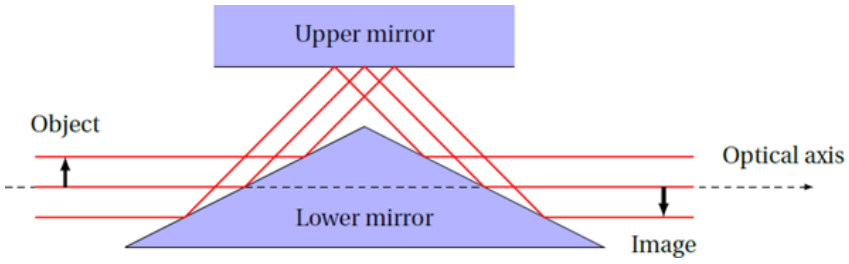

Figure 1.10: K-mirror Principle

For fixing the image with respect to the sensor, it is necessary to turn the K-mirror in the opposite direction twice slower than the rotation of the optical beam. This is explained by the fact this system is equivalent to turn a flat mirror by an angle θ; It leads the reflexion of the output ray to 2θ (for a fixed object, the image rotates twice faster than the derotator).

In our case, the derotation of the field of view is done by using a K-mirror. Despite the fact that the Dove prism is an attractive solution (regarding the cost and precision

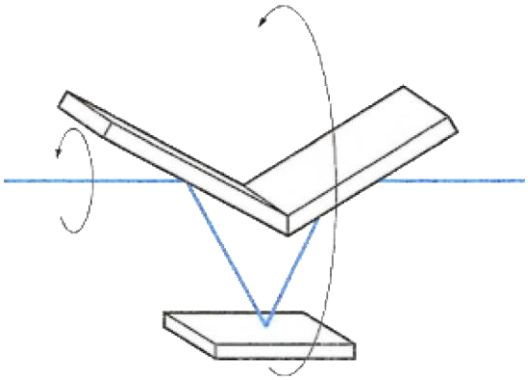

Figure 1.11: Principle of the K-mirror [14]

between faces), it generates chromatic aberration. The K-mirror is the only design that offers absolute achromatism as well as an absence of astigmatism.

2. TECHNICAL SPECIFICATIONS

2.1 System Technical Specifications

Contractual specifications are defined by the appointed tender.

- The derotator shall have 7 arc min field of view (FoV).
- The derotator shall correct the field rotation similar to the AO derotator.
- The derotator shall correct the field rotation with a rotational speed of maximum 0.18 deg/second (speed at 1 degree from the zenith, which is the closer the telescope will point towards the zenith).
- The derotator shall produce a maximal wavefront error on the image and pupil plane of 10 nm
- The beam lateral deviation measured at 100 mm from the exit surface of the derotator shall not exceed 1 μm for 180˚ rotation of the derotator
- The derotator does not have to rotate for the full 180˚ and a range of -60˚ to +60˚ from the home position (mirrors facing the zenith) is sufficient

2.2 Environmental Specifications

- Operational temperature: -15˚C to +15˚C
- Survival temperature: -30˚C to +30˚C
- Storage: same as survival temperature, with instantaneous gradients of 20˚C applied to the outside of the box as this could happen when the box is taken from a heated laboratory to the telescope
- Survival relative humidity: 2% to 90% for observation
- Operational relative humidity: 100% for observation

2.3 Location, Size and Volume

It has been stated that the allocated space in the Nasmyth flange is sufficient[9]. The derotator field of view should be maximized in function of the available space and mechanical considerations.

- The derotator shall be compatible with the following optical beam parameters:
- The center of M1 shall be approximately 100 mm after the new focal plane, allowing to locate a calibration source on-axis.
- The beams envelope at the entrance plane of the derotator is a disc of diameter 132.2 mm.
- A marging of 10 mm around the mirrors shall be considered to allow for the drop of optical quality on the mirror edges.
- There is no constraint on the diameter of the derotator. The higher M2, the shorter the whole optical combination, but at the cost of a higher susceptibility to flexure and vibration transmissions. We do not expect the derotator optical combination to be higher than approximately 500 mm.
- The length of the derotator optical combination should be not much longer than approximately 600 mm.

Overall, the idea is to keep the optical combination as compact as possible, allowing a possible use of off-the-shelf mirrors instead of custom manufacturing, and in any case, find an optical combination that minimize the overall size of the M1-M2-M3 mirrors.

2.4 Operation Specifications

- The derotator should operate with a horizontal axis
- The optical coatings should be protected silver and shall last for 10 years.
- The mechanical surface painting must not degrade for 10 years.
- 1^{st} eigen frequency should be below 60 Hz

[9] The available space is defined by the fork center hole diameter (580 mm)

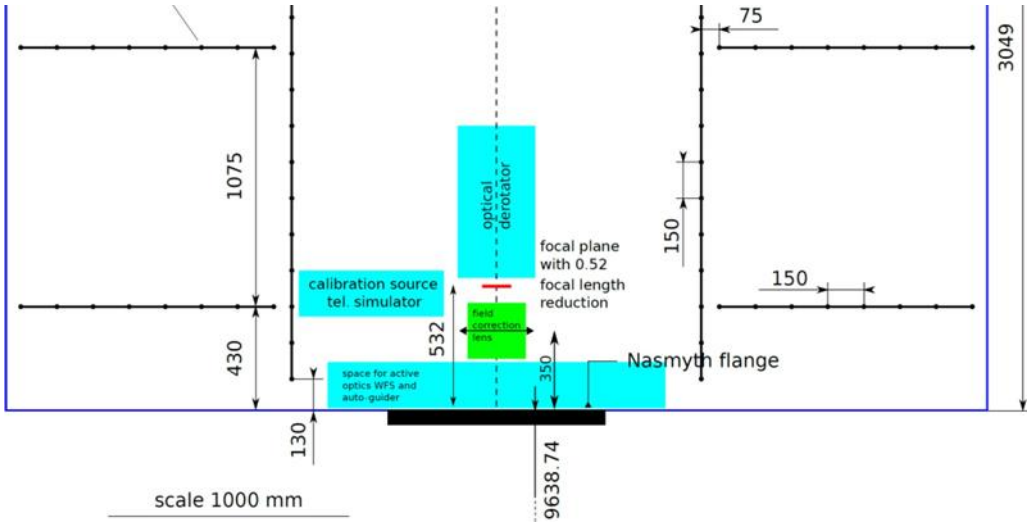

Figure 2.1: Top schematic of the Nasmyth platform

- Maximal deflection on the system should be below 250 µm
- Angular accuracy should be below or equal to $\pm 0.1^0$
- Wobble should be below or equal to ±1µrad
- Eccentricity should be below or equal to 250µM
- Mirror surface tolerance should be below or equal to ±250nm
- Optical axis shear should be below or equal to ±250µm
- Optical axis alignment should be below or equal to $\pm 1^0$

3. OPTO MECHANICAL MODEL

This chapter presents explains how does the setting system of the derotator work. Mirrors alignment precision is directly related with precision of the global assembly. In this way, a mirror setting systems are developed. Internal flexures are reduced as much as possible; the supports and housing are designed as rigid as possible. Hyperstatism is avoided and also the derotator rotational axis is aligned with the telescope optical axis. So, the system has ability of fine adjustment for collinearity. The idea is to enclose the K-mirror mount in the CF housing which has resistant to the thermal expansion in order to optimize the symmetrical mass equilibrium and stiffness. The lids are mounted on input and output faces of the housing to improve stiffness.

3.1 Mirror Adjustment Mechanisms

The mirrors are glued on pads and the pads are attached to semi-kinematic mounts. Semi-kinematic mounts are used in order to prevent hyperstatism and internal constrains. Each mirror has three mount attachment and each mount has one degree of freedom on different axis. Due to the fact that the derotator rotates, each of the semi-kinematic mount is axially pre-constrained by three springs.

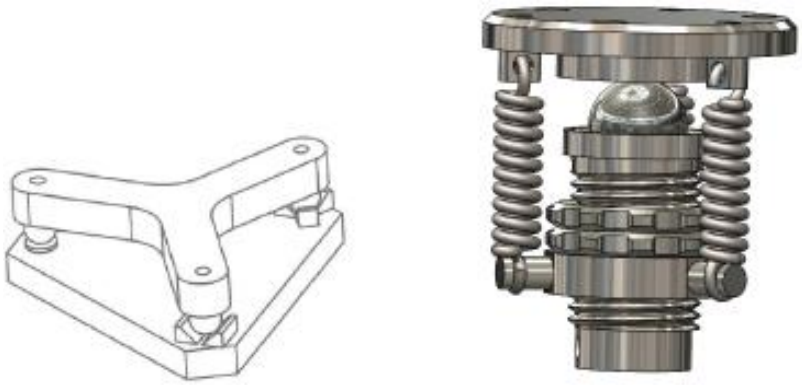

Figure 3.1: Semi kinematic mounts

The upper mirror is not directly attached to the CF structure. The mirror is clamped with spring preloaded pins on three semi-kinematic contact points.

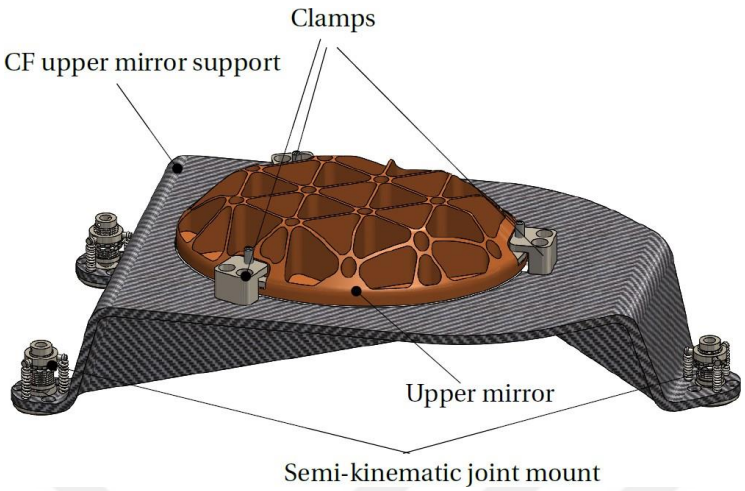

Figure 3.2: Upper mirror mount

The upper mirror mount assembly also has three attachment points. It is connected by semi-kinematic mount mechanisms to the housing. The mechanisms give the ability of tip and tilt adjustment ability to the upper mirror mount assembly.

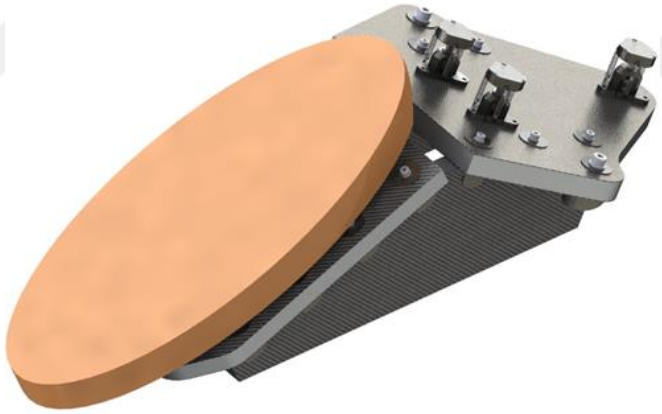

Figure 3.3: M1 and M3 mirrors sub-assembly

M1 and M3 mounts are connected to spring mechanisms which are manipulated by micrometers. Since M1 and M3 mirrors have three of those mechanisms, they have tip and tilt adjustment ability.

The lower mirrors mount is connected to the front and back CF panel on three points by spring mount mechanisms as same as upper mirror M2. The mechanisms give extra degrees of freedom

to the lower mirrors. Since fine adjustment of the lower mirrors is more complex then M2 mirror, this extra feature provides larger margin for the lower mirror assembly.

3.2 Setting Flange

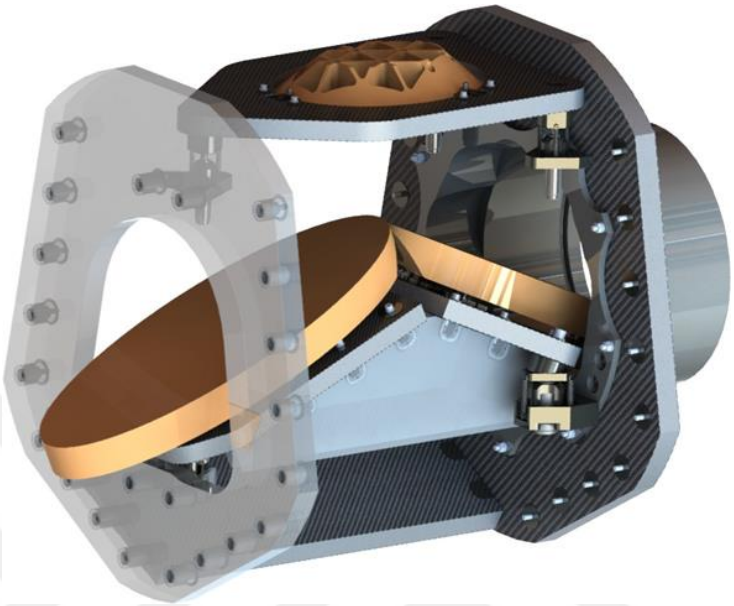

Figure 3.4: M1 and M3 mirrors sub-assembly

In real life, the K-mirror mount axis should be almost perfectly aligned on the optical axis as it is designed on paper. In way, the derotator axis should be adjustable along dx and dy axis and the rotation around them rx and rx. The following figure (3.5) shows these four degrees of freedom.

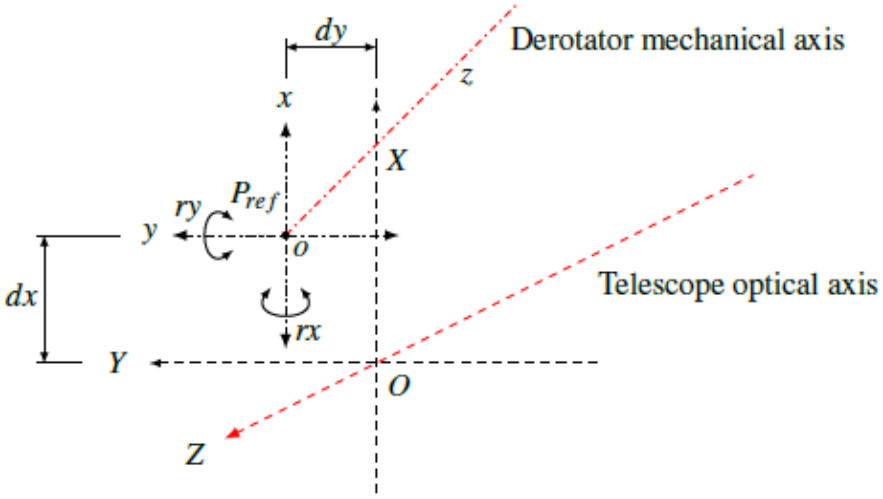

Figure 3.5: Derotator on the Nasmyth flange DOFs

In order to have such DoF, the setting flange is placed between the telescope fork and the K-mirror mount. The linear displacement is done by linear bearings are indicated as number 2 in the picture 3.6 and they are placed along X and Y axis. The setting manipulation is done by differential screws (shown as number 1 in the picture 3.6) in order to maximize the setting resolution.

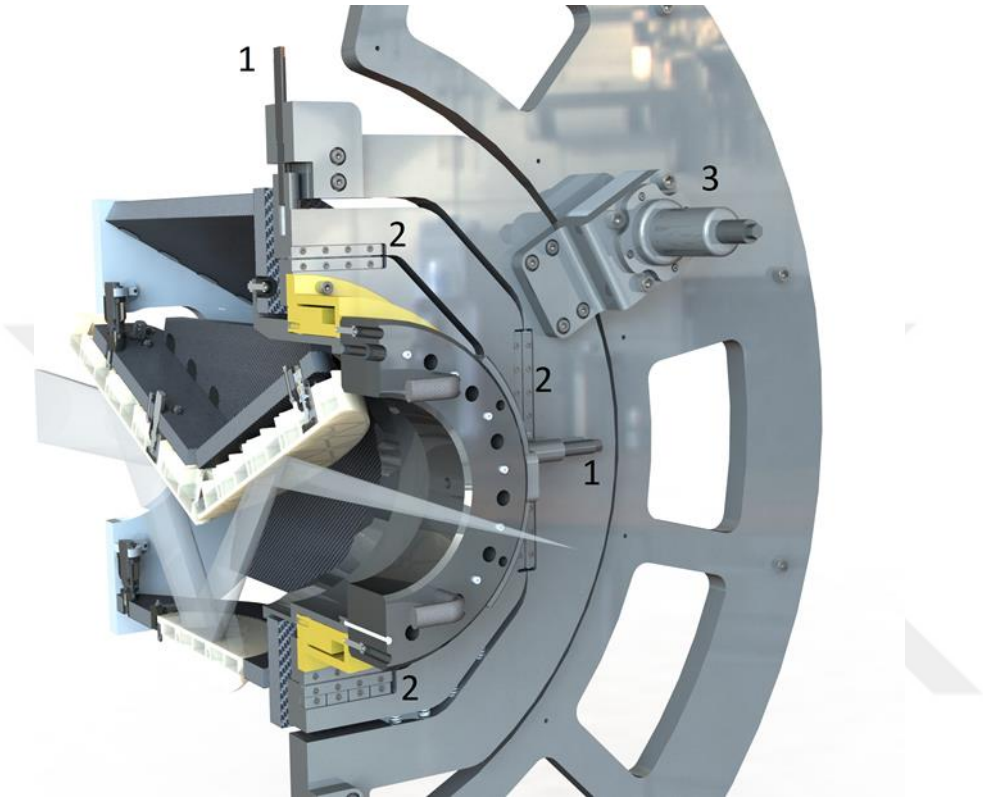

Figure 3.6: Setting system on the flange

Then, the setting flange is fixed on the derotator support on three points which are shown as number in the picture 3.6. Each of these points consist of ball joints where they allow tip and tilt adjustment to the setting flange on *X* - *Y* plane. Such adjustment capability is needed to set parallelism between the derotators optical axis and telescopes optical axis. Same as the linear bearing manipulation, differential screws are used to achieve enough setting resolution.

The figure 3.7 presents the setting flange assembly (number 2) on support flange (number 1). The support flange is the fix flange which provides the connection between telescope fork and the derotator.

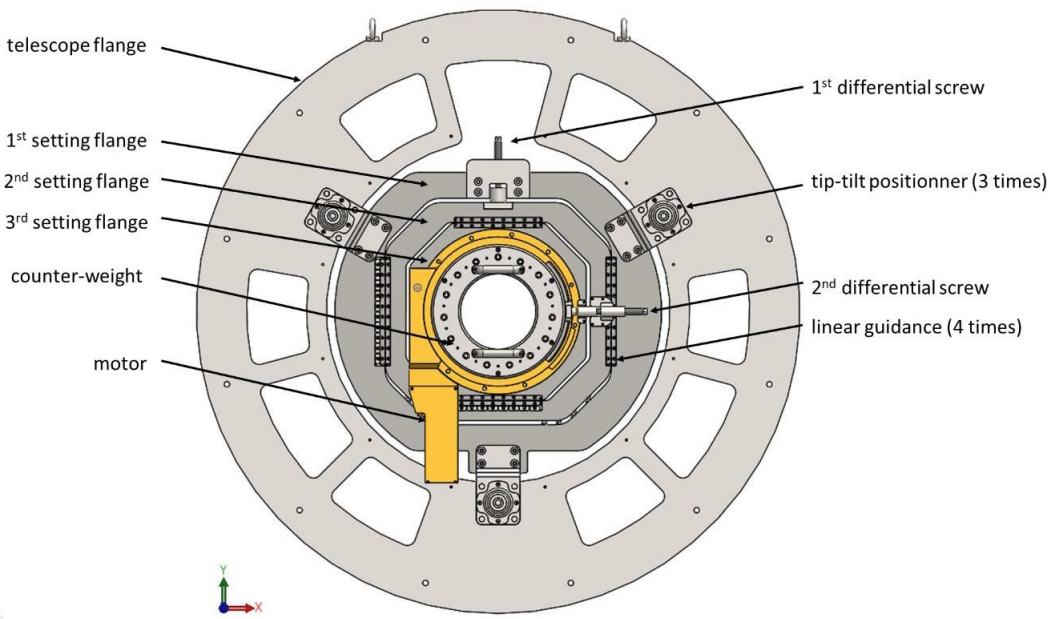

Figure 3.7: Setting flange

4. HOUSING DESIGN and COUNTERWEIGHT SIZING

This chapter is about housing design and its functionality. The housing has two functional roles; it covers the mirror mechanism and it is the skeleton of the system.

It is designed to work in the telescopes fork hole but having a cover on the mirrors is important. The cover provides a controllable volume for the mirrors. The derotator can be used on an optical bench for research and development. The cover blocks high percentage of undesired reflections by the matte black special coating. Besides, it also blocks direct contact to the mirror surfaces against undesired physical contacts.

4.1 Housing Flexure Estimation

An important point is the internal flexure of the housing. The housing flexure depends on the housing weight and its material stiffness. This section is dedicated to present housing flexure analysis. First the study has been realized with classical strength of materials and then with the FEM tool from Solidworks.

In order to estimate the structural stiffness, a simple model is considered. It is consisting of a carbon fiber cylinder with 560 mm in diameter, 8 mm thickness and 458 mm length. It is assumed that the internal equipment weight is 15 kg. For theoretical calculations, Pyrofil MS40-12M carbon fiber is considered as housing material. Material selection for housing is explained on section 8.1. The material has young modulus of 345000 N/mm2 but it is taken as 100000 N/mm^2 for computations with safety factor.

The deflection of the housing can be modeled as a deflected beam.

$$f_{max} = \frac{f l^3}{3 E I_v} \tag{4.1}$$

For a cylinder, the moment of inertia is

$$I_x = \frac{\pi(D^4 - d^4)}{64} \tag{4.2}$$

and with the parameters given we find $I_x = 528.5\ 10^6$ mm^4.

Figure 4.1 shows the case of the clamped beam with load F_{load} and the CF shell F_p mass forces.

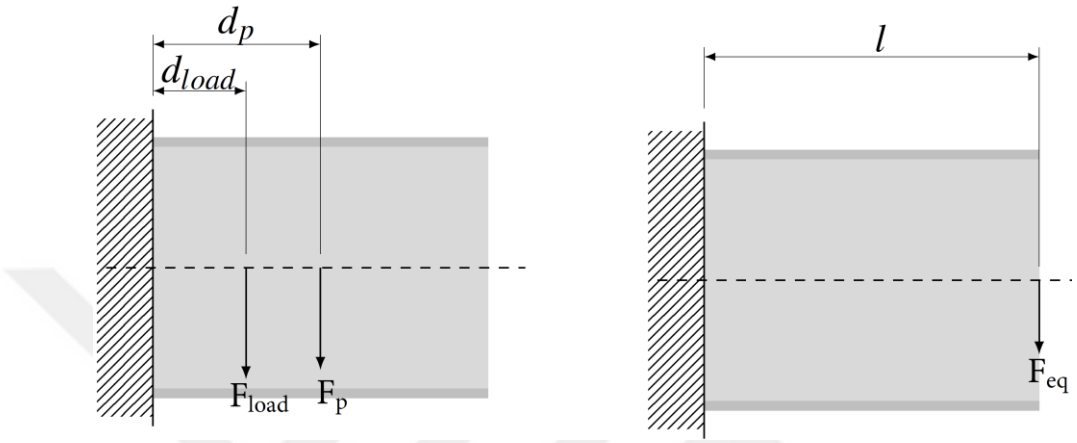

Figure 4.1: Clamped beam case (left) and equivalent force (left)

The moment equation can be written as;

$$F_{load} d_{load} + F_p d_p = F_{eq} l \tag{4.3}$$

It is assumed that the center of gravity is at the middle of the the housing length. Then, F_{eq} can be calculated as;

$$F_{eq} = \frac{g(m_1 d_1 + m_p l/2)}{l} = 136\ N \tag{4.4}$$

Knowing the housing length (l = 458 mm), bending can be calculated;

$$f_{max} = \frac{F l^3}{3 E I_x} = 0.08\ \mu m \tag{4.5}$$

It can be seen that the magnitude of the bending is negligible. However, by experience, when the ratio between the diameter and the length of the part is close to 1, shear displacement must be taken into account too. Using classical strength of materials, the shear deformation can be calculated;

$$\delta_{sh} = \frac{F_{eq} l}{AG} \tag{4.6}$$

where the shear modulus G is

$$G = \frac{E}{2(1+\nu)} = 39062.5\ N/mm^2 \tag{4.7}$$

where ν is chosen as 0.28. A is the area of the cross section.

$$A = \pi\left(\frac{D^2}{4} - \frac{d^2}{4}\right) = 13.84\ 10^3\ mm^2 \tag{4.8}$$

then,

$$\delta_{sh} = 0.11\ \mu m \tag{4.9}$$

And the total deflection can be estimated by summing the bending and shear values.

$$\delta_{tot} = f_{max} + \delta_{sh} = 0.2\ \mu m \tag{4.10}$$

4.2 First Design Approach

The skeleton consists of 6 carbon fiber panels. Its unique shape is formed to have high rigidity. Figure 4.2 show first the design of the housing.

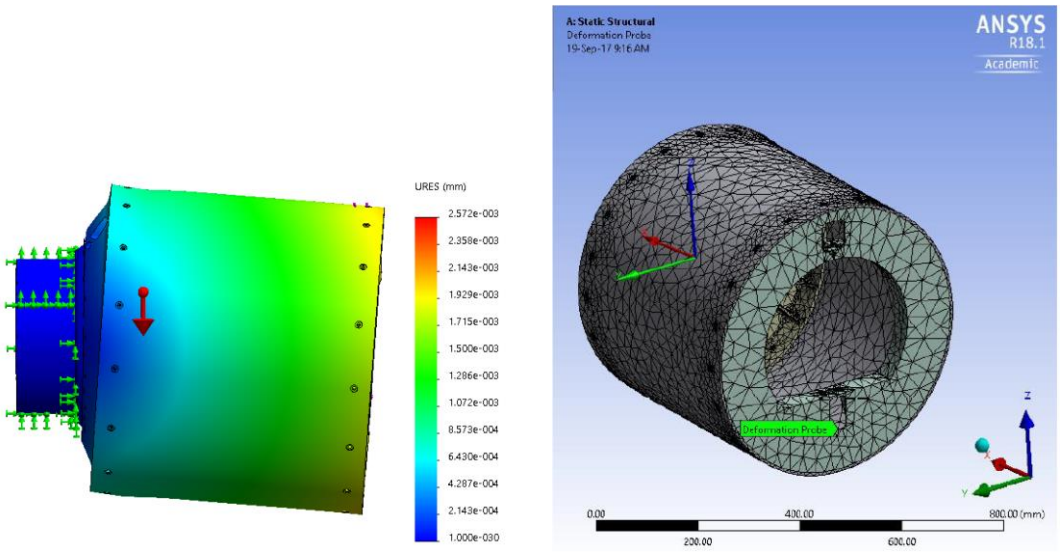

a) b)

Figure 4.2: Left, housing deflection (horizontally oriented) SW model. Right, ANSYS model

The most important design criteria are having less deflection as much as possible.Since the derotator has to have cantilever type of the connection to the flange, maximal deflection occurs on the back panel. The firs idea was making the housing as a cylinder.

There were some problems on this approach. Firstly, manufacturing such cylinder is very costly and almost not possible to manufacture a perfectly rounded cylinder from composite materials. Another weak point was connection of the front and back panels to the cylinder. Lastly, developing an alignment procedure is nearly impossible with the cylindrical housing.

4.2.1 FEM validation

Purpose of the analysis is to estimate the static flexure of the derotator with respect to different orientations. The analysis is repeated for every 45 degrees which means the flexure of the system is computed for 8 different orientations (0-315°). The orientation of 0 degrees is when the derotator lower mirrors are oriented horizontally and the upper mirror is parallel to the ZY plane.

The carbon fiber housing, invar housing sockets and lids are considered in the analysis. The external diameter of the housing socket is selected as the fixed face of the assembly and gravity is applied on all included components. The optical system which is inside of the CF housing is represented as a remote force which is distributed on the CF supports. The optical system's weight and center of mass are estimated with the Solidworks design. Since global coordinates are tilted on Z axis, a local coordinate system is defined to avoid errors in results. For this analysis Solidworks analysis tool is used.

Figure 4.3 shows how the housing deflection varies with its orientation. We can see that the peak deflection is D_{pp} = 0.66 µm. The maximal bending at the extremity of the housing is D_{max} = 2.6 µm.

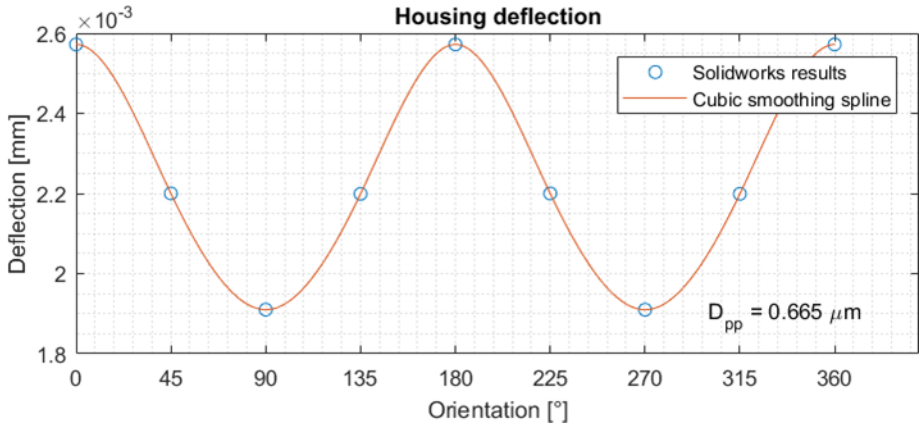

Figure 4.3: Housing deflection (SolidWorks)

In order to improve the validity of the study, the same analysis is repeated with ANSYS. The same remote force (150 N) is placed as the center of gravity of the internal assembly. The fixed part is identical as the previous analysis (outer diameter of the housing socket). Figure 4.2 shows ANSYS model and the location of the deformation tool.

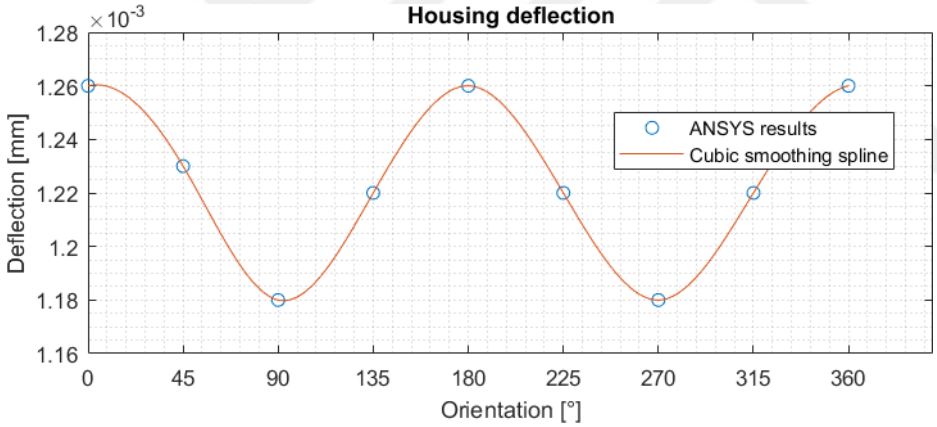

Figure 4.4: Housing deflection (ANSYS)

Figure 4.4 shows the evolution of the housing deflection with respect to its orientation. It can be seen that the computed peak deflection is D_{pp} = 0.081 µm. The maximal bending at the extremity of the housing is D_{max} = 1.26 µm.

4.3 Final Design

The design is evolved to its recent shape to overcome the previous problems. The flat panels are way easier for manufacturing and cheaper too. Thank to the connection

positions of the panels to each other, the rigidity criteria are successfully met. The detachable panels make possible to develop a fine alignment procedure.

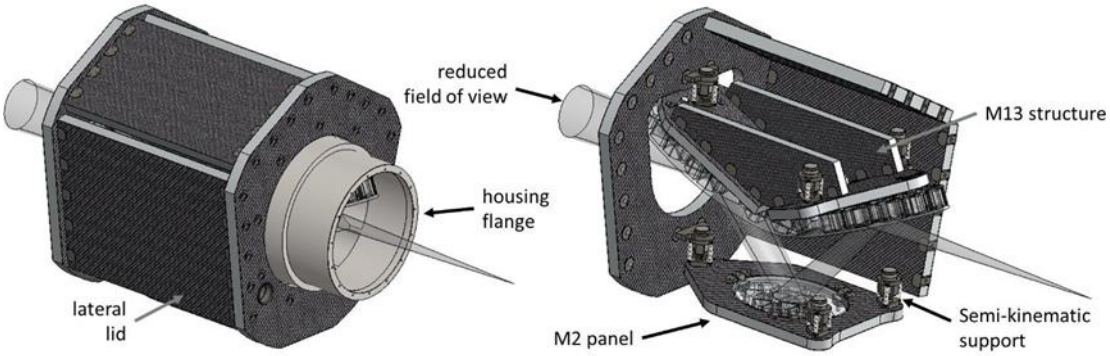

Figure 4.5: Housing structure

Figure 4.5 shows the K-mirror mount and an inside view without the carbon fiber housing lids. It allows to see the interface between mirrors and CF structure. M1 and M3 mirror are assembled a common structure. This M13 structure is mounted inside of the housing by 3 additional semi-kinematic support.

Semi-cinematic mounts are placed between mirrors and CF panels. The adjustment is made by hand turning each micrometer head passing through the carbon fiber panel.

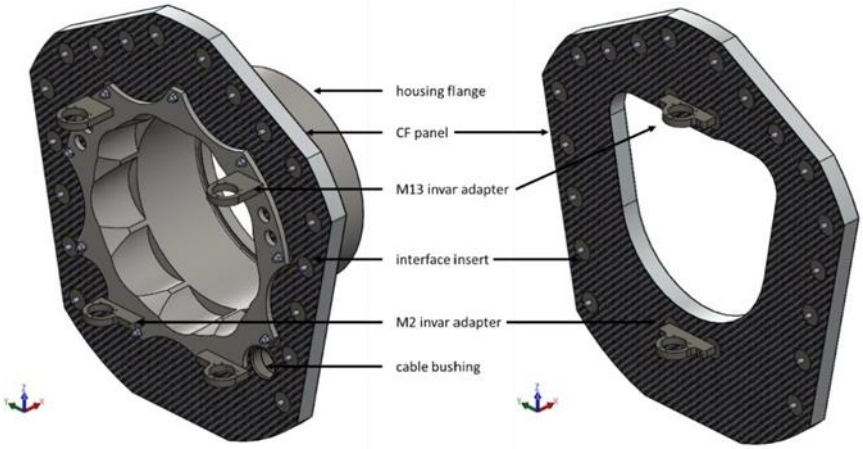

Figure 4.6: Input and output panels

The input side panel is screwed in the lateral lid to improve stiffness of the housing. The output side panel is mounted with the housing flange. Each panel contains Invar adapter to attach semi-kinematic mount.

4.4 Counterweight Sizing

Referring to the section 3, the mounted load on the rotating stage and on the flange must not exceed a certain cantilever load. It is a function of the load weight and the off-axis distance. In order to balance the system on the flange, a counterweight is attached on the opposite side of the housing. The idea is to place the centre of mass perfectly aligned with the screws that fix the derotator on the setting flange. This solution brings an advantage; the acting moment on the setting flange can be adjusted. The constrained flange is more stable and easier to design. However, the motor might not capable of handling with the applied moment and force, because the center of mass is not aligned with the motor. This point is investigated in the section 10.

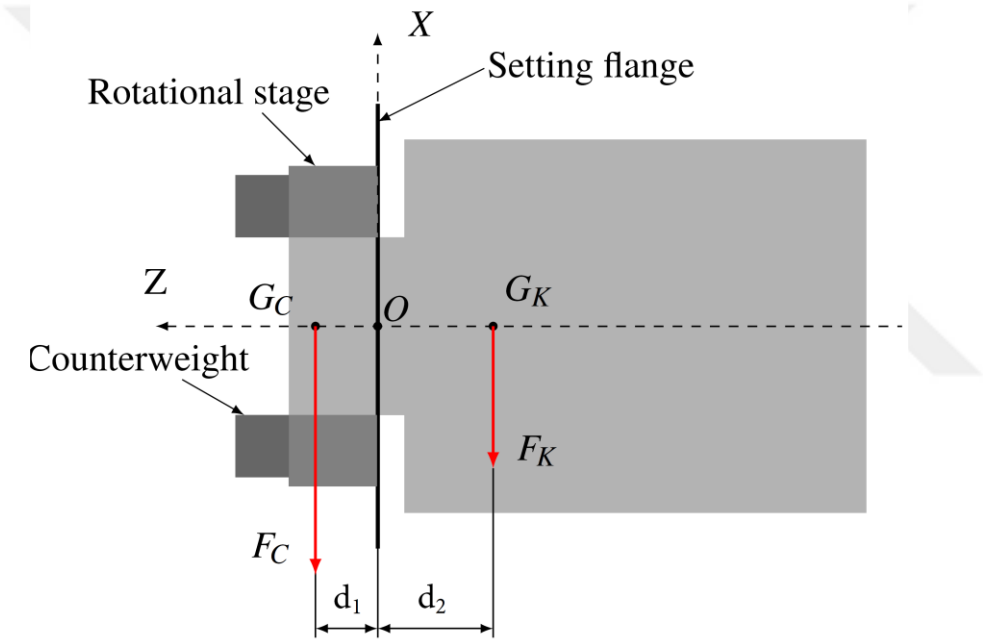

Figure 4.7: Counterweight sizing

In the solidworks mechanical design, the counterweight center of mass has been dimensioned to fit with the previous statement. It is found $m_{C\ opt}$ = 36 kg by iteratively changing counterweight size and displaying the center of mass of the assembly.

5. MIRROR DESIGN

This chapter is dedicated to explain mirror design. The starting point of the design is aiming to have such mirror shape which is as close as possible to off the shelf ones. The shape of the mirrors must be simple and its material should be machinable. The details of the material selection of the mirror are on the chapter 8.2

The first design idea was making the lower mirrors as one mono-block piece in order to avoid alignment problems. Such design is very useful for minimizing the displacements due to thermal effects. After discussions on this point with Schott, it is concluded that the manufacturability of design is not simple and more costly than it is expected. Another argument is with the mono-block solution, if there is a problem on one reflecting surface, the full part would be compromised. Ordering a spare part would be much expensive and maintenance process (e.g., coating) would be much complicated. As a result, the 2 lower mirrors solution has been selected.

The derotator mount should be as light as possible. So, mirrors must be light weighted. It is possible to decrease the mirrors mass up to 90% by milling like in the picture 5.1.

Figure 5.1: Light weighted mirror example

5.1 Optical Design Setup

The K-mirror mount is made up of three flat mirrors in a K layout as presented in the introduction. The following sketch shows the disposition of each mirror and the characteristic dimensions.

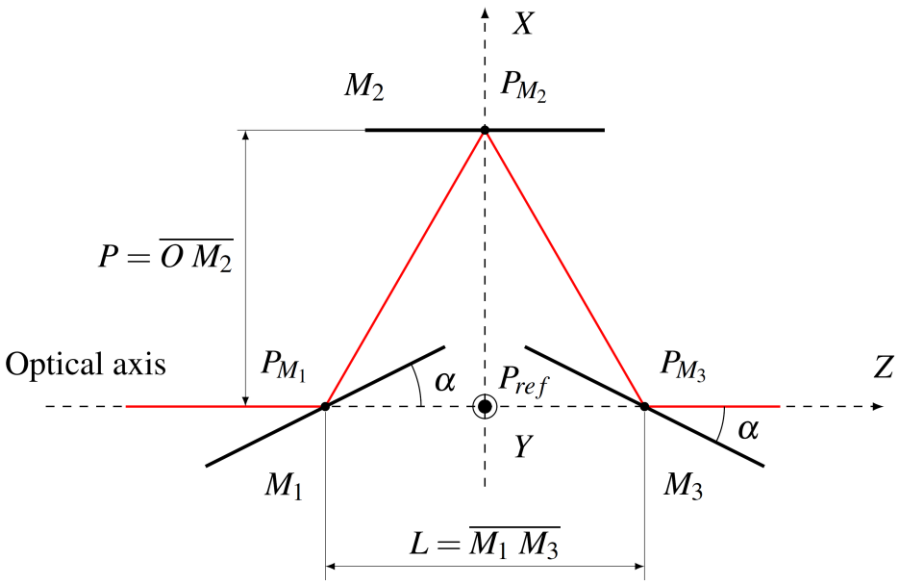

Figure 5.2: Derotator layout

As the available space is limited with Ø580 mm, P is maximized and set by the mechanical design. Then the system is under-determined. α and L must be chosen in order to minimize the cantilever and allow the 7 arcmin beam to pass through the system. After multiple iterative trials, the angle that offered the best compromise is $\alpha = 24^0$. Then L can be fixed.

P_{ref} is the reference point of the derotator. This the the intersection of the optical axis (Z) with the center axis of M_2 (X). It is used to reference M_1 and M_3 on the optical axis and the derotator with respect to the Nasmyth flange.

The lengths above and below the optical axis are not identical since the the beam is convergent. That means the mirror centers are not intersecting with the optical axis.

5.2 Mirrors Optical Dimensioning

Derotator mirrors dimensions are fixed by the 2D ray tracing model. This software computes elliptical mirrors dimensions (major and minor axis) according to a specified FoV, the angle of lower mirrors with respect to the optical axis, the available space diameter and the position of the derotator with respect to the Nasmyth flange face[10].

[10] At the beginning, this Matlab program has been developed for a fixed FoV of 5 arcmin. This is the reason why it does not allow to specify the maximal FoV as a result of the computation but as a parameter.

The field of view has been fixed at 7 arcmin due to the fact that, geometrically, more the FoV is wide, more the lower mirror is long and more the system will bend because of the cantilever.

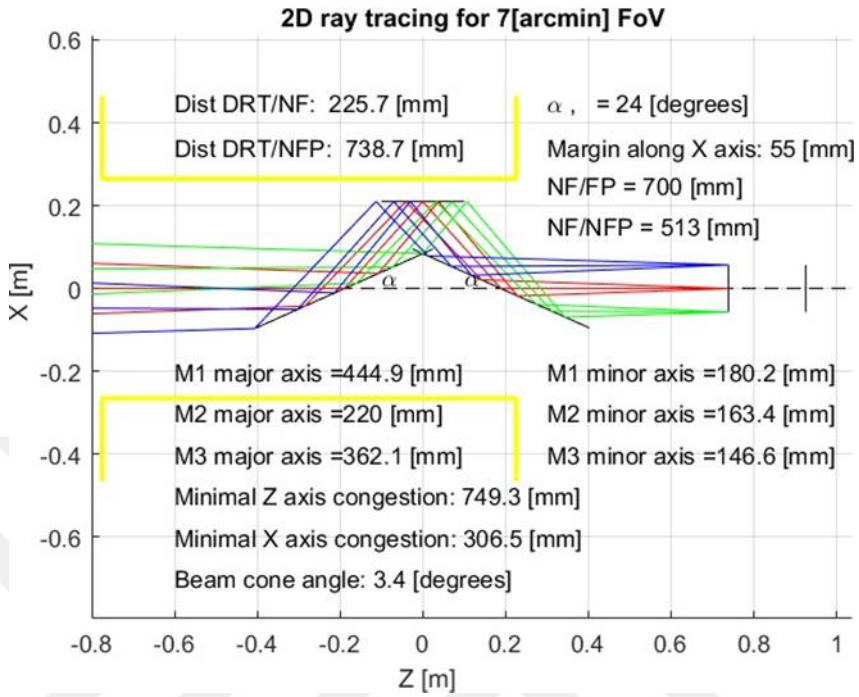

Figure 5.3: Ray tracing 2D

The construction dimensions will be a bit larger than calculated to allow adjustments margins (about 5mm on each side).

The two lower mirrors will be made in one piece to simplify adjustments and avoid misalignment between each of them.

As stated in the previous study [18], mirrors thickness should be 1/6 to 1/5 of the major axis of each one (largest mirror dimension).

5.3 Light Weighting

Schott can light weight the mirrors at a rate of 85% for Zerodur material. There is a trade of about the light weighting; more light weighting means more expensive to manufacture. This is due to the fact that it is riskier for the blank and longer to machine. The cost for light weighted design is about 10k CHF. It was resulted to make a self design by following recommendations of Schott. It is aimed to have a good ratio between the cost and the lightweight.

The lower mirror M_1 has 6.14 kg weight with bulk design. After light weighting it, the curremt design has 1.56 kg mass. It means the light weighting ratio is 74%.

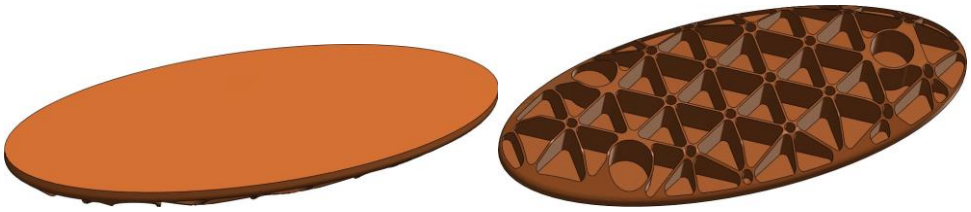

(a) (b)

Figure 5.4: Lower mirror, M1 reflecting face (a), back face (b)

The lower mirror M_3 full weight is 4.17 kg. With the current design, its weight is 1.13 kg (lightweight ratio 73%).

(a) (b)

Figure 5.5: Lower mirror M3 reflecting face (a), back face (b)

The lower mirror M_2 full weight is 3.23 kg. With the presented design, its weight is 0.78 kg (lightweight ratio 76%).

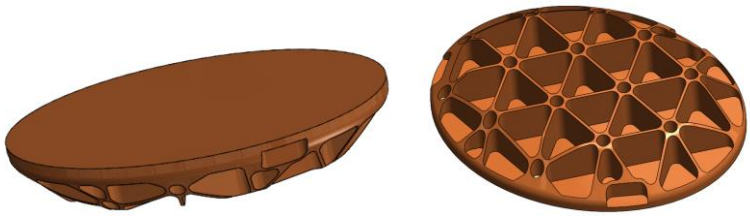

(a) (b)

Figure 5.6: Upper mirror M2 reflecting face (a), back face (b)

The average lightweight ratio is about 75%, which is lower than Schott number, but saves 10k CHF.

5.4 Mirrors Internal Flexures

The K-mirror is composed by 3 mirrors which are calling upper (M_2) and lower mirrors (M_1, M_3). Those mirrors are made with the same material which is Zerodur. In this

section the deflection of those mirrors is estimated with an analytical approach then consolidated with FEM.

5.4.1 Analytical approach

The "Field guide to opto-mechanical design and analysis" [19] proposes circular flat mirrors own-weight deflection calculus in function of their orientation.

For a plate mirror mounted laterally (axis horizontal) the deflection (δ_{Hrms}) is

$$\delta_{Hrms} = (a_0 + a_1\Upsilon + a_2\Upsilon^2)\left(\frac{2\rho r^2}{E}\right) \tag{11}$$

With

$$\Upsilon = \left(\frac{r^2}{2hR}\right) \tag{12}$$

Table 5.1: Miror variables

Variable	Explanation	Value	Unit
a_0	Cons. par.	0.05466	-
a_1	Cons. par.	0.2786	-
a_2	Cons. par.	0.110	-
ρ	Density	2530	kg/m^3
r	Half mirror diameter	$120\ 10^{-3}$	m
h	Mirorr thickness	$40\ 10^{-3}$	m
R	Mirror rad. Of curv.	inf	m
E	Zerodur Young mod	$91\ 10^9$	N/m^2

Where a_0, a_1 and a_2 have been chosen regarding the fixation system (three clamped points equally spaced ath the edge of the mirror).

For a mirror mounted axially (axis vertical) the deflection (δ_{Vrms}) is:

$$\delta_{Vrms} = C_{sp}\left(\frac{\rho g}{E}\right)\frac{r^4}{h^2}(1-\nu^2) \tag{13}$$

Where C_{sp} has been chosen for three points equally spaced at edge support constraint. It is taken as 1.356 and Poission's ratio is accepted as 0.24 for this case. This is varying in function of the support constraint type.

An error on a mirror surface is multiplied by a factor of two in the reflected wavefront. The overall rms self-weight deflection of a mirror mounted at an angle can be estimated by

$$\delta_{\theta rms} = \sqrt{\delta_{\theta-v}^2 + \delta_{\theta+H}^2} \tag{14}$$

With

$$\delta_{\theta-v} = cos(\theta)\delta_{Vrms} \tag{15}$$

$$\delta_{\theta-H} = sin(\theta)\delta_{Hrms} \tag{16}$$

Considering that the angle varies from 0 to 90^0, the overall rms deflection of the three mirrors with respect to the orientation are plotted.

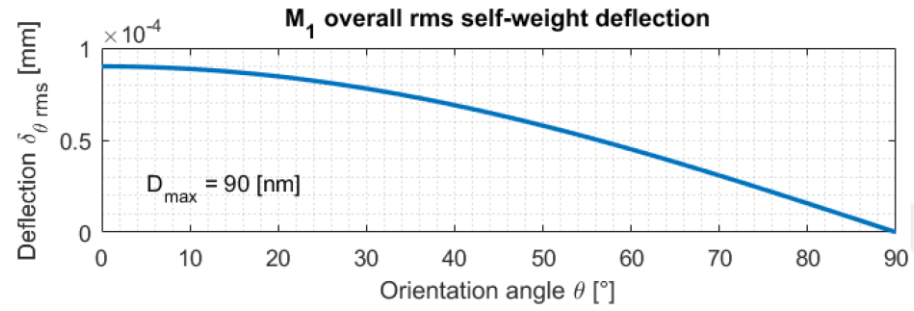

a)

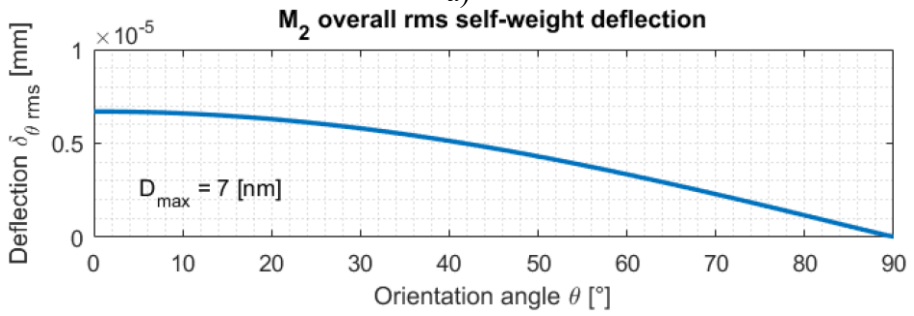

b)

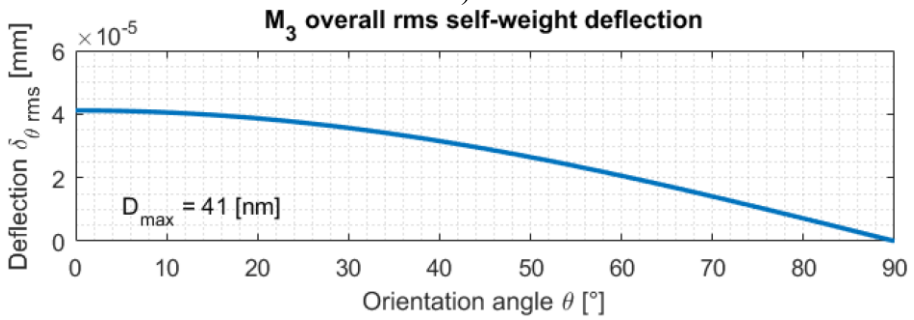

c)

Figure 5.7: a) M1 b) M2 and c) M3 deflections by self weight

It can be seen that the maximal computed rms deflection is about 90 nm for M_1, 7 nm for M_2 and 41 nm for M_3 and it decreases to 0 when the angle goes to 90^0.

5.4.2 FEM approach

FEM analyses of the light weighted models are aimed to see the deflection caused by their own weight. The purpose of this study is to get the order of magnitude.

Figure 5.8 shows the upper mirror deflections due to the gravity with respect to its orientation.

It can be seen that the peak to peak deflection D_{pp} is 57 nm and the maximal deflection D_{max} is 81 nm.

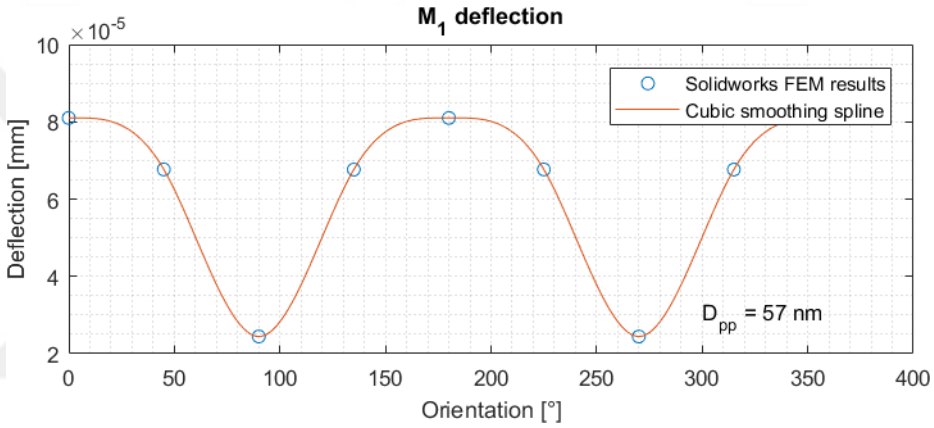

Figure 5.8: M1 under its own weight deflections

Figure 5.9 shows the upper mirror deflections due to the gravity with respect to its orientation. We see that the peak to peak deflection D_{pp} is 40 nm and the maximal deflection D_{max} is 54 nm.

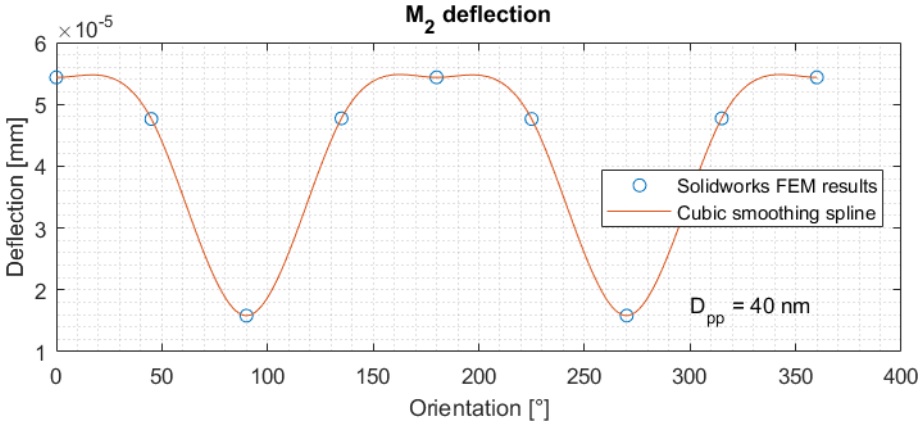

Figure 5.9: M2 under its own weight deflections

Figure 5.10 shows the upper mirror deflections due to the gravity with respect to its orientation. The peak deflection is about 23 nm and the maximal deflection D_{max} is 33 nm.

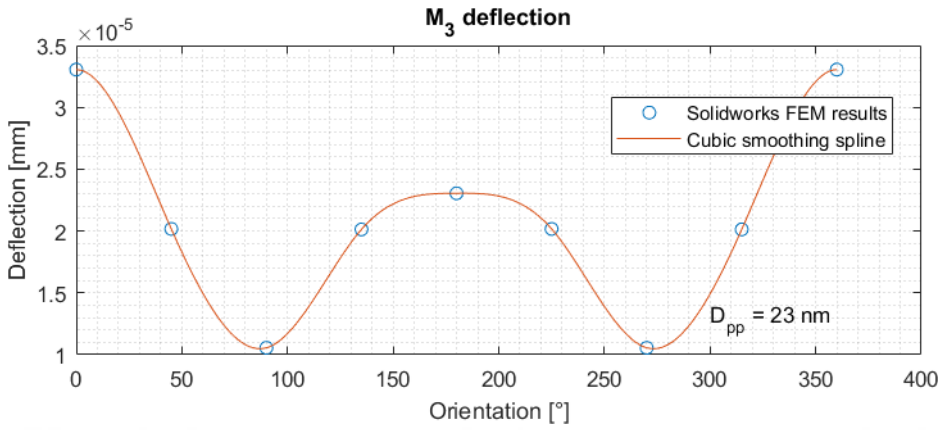

Figure 5.10: M3 under its own weight deflections

In order to improve the reliability of the study, the analysis is repeated with ANSYS too. The fixed faces are identical as the previous analysis.

Figure 5.11 shows the evolution of the housing deflection with respect to its orientation. The peak deflection D_{pp} is 77.1 μm. The maximal bending at the extremity of the housing D_{max} is 101.1 μm.

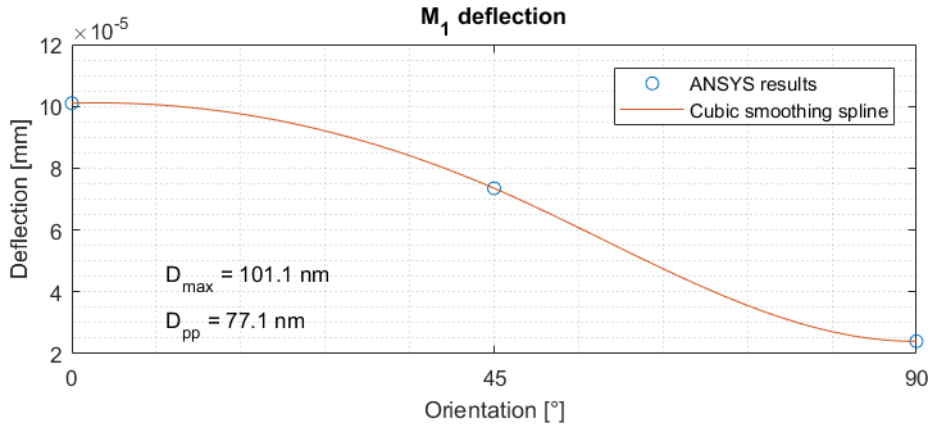

Figure 5.11: M1 deflection

Figure 5.12 shows the evolution of the housing deflection with respect to its orientation. The computed peak deflection D_{pp} is 32.1 μm. The maximal bending at the extremity of the housing D_{max} is 37.5 μm.

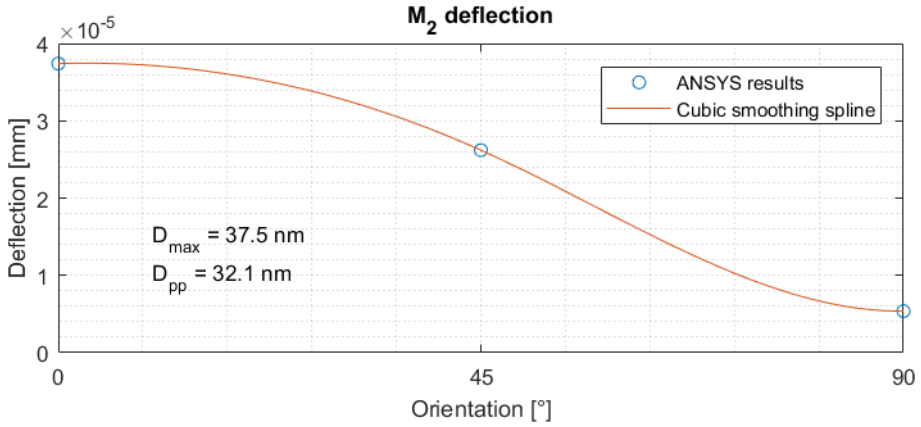

Figure 5.12: M2 deflection

Figure 5.13 shows the evolution of the housing deflection with respect to its orientation. The peak to peak deflection D_{pp} is 10.8 μm. The maximal bending at the extremity of the housing D_{max} is 16.2 μm.

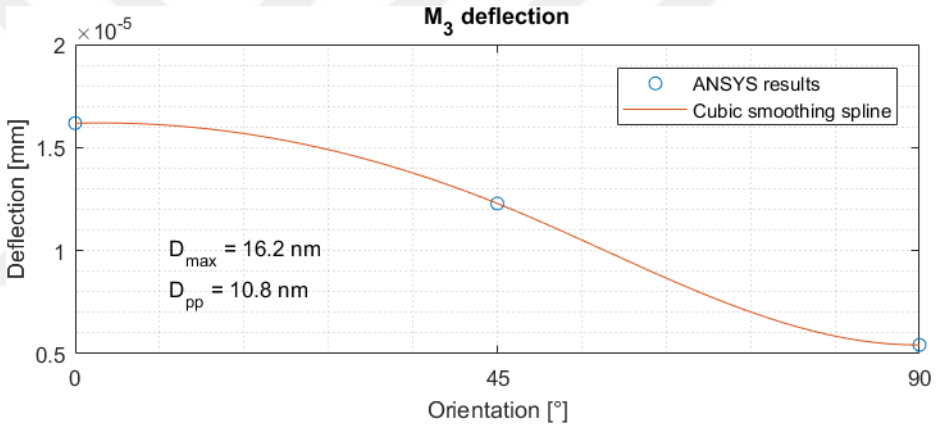

Figure 5.13: M3 deflection

The figures in this subsection show the success of the design by showing self deflection of the mirrors and their total deflections with housing.

5.5 Summary

The following table summarize the maximal deflection of each mirror from the analytical expressions and the values of our SW model (SW & ANSYS solvers).

Table 5.2 Deflection summary

Mirror	SW solver (nm)	Ansys solver (nm)	Analytic Value (nm)
M_1	81	101.1	90
M_2	54	37.5	7
M_3	33	16.2	41

The considered light range starts from 370nm, then it can be note that the mirrors deflection doesn’t exceed the shortest wavelength. Moreover, the deflection corresponds to a low spatial frequency which is quite easy to correct with the adaptive optics system.

6. MIRROR ATTACHMENT DESIGN

Mirrors mount is a critical element of the derotator. The global stiffness and precision depend on their positioning accuracy. Since these mirrors are flat, they must be adjustable for four degrees of freedom. As stated in the specifications, mirrors adjustments must be hand-controlled. Mirrors positioning alignments should be made from the Nasmyth platform.

Light weighted Zerodur mirrors are mounted on micrometer head to set alignment. Semi-kinematic mounts are placed between mirrors pads and micrometer head to prevent internal constrains as shown on the figure below. Since the housing rotates, each of the semi-kinematic mount is axially preliminary constrained with springs. Micrometer head adapters are mounted on invar support which are screwed in the carbon fiber housing structure.

There are three micrometer head per mirror to create an isostatic point-line-plane contact.

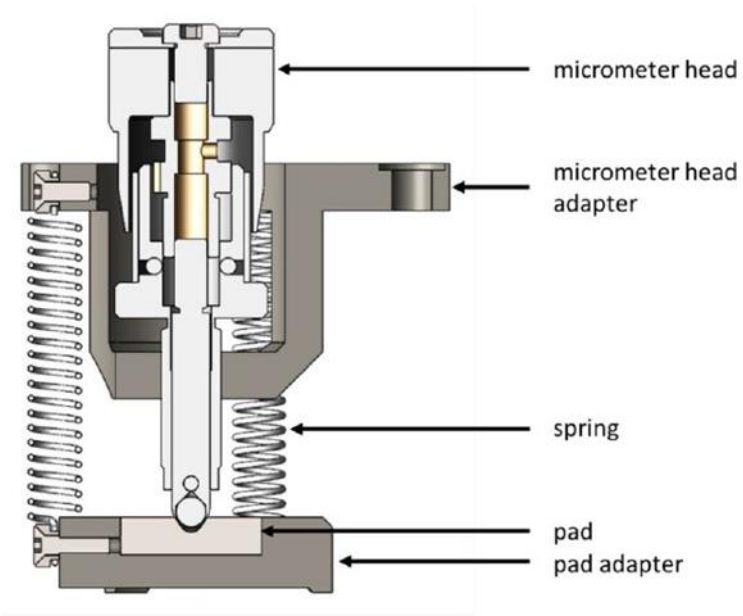

Figure 6.1: Mirror alignment system

Light weighted Zerodur mirrors are mounted on the micrometer head to set alignment as shown figure 6.2.

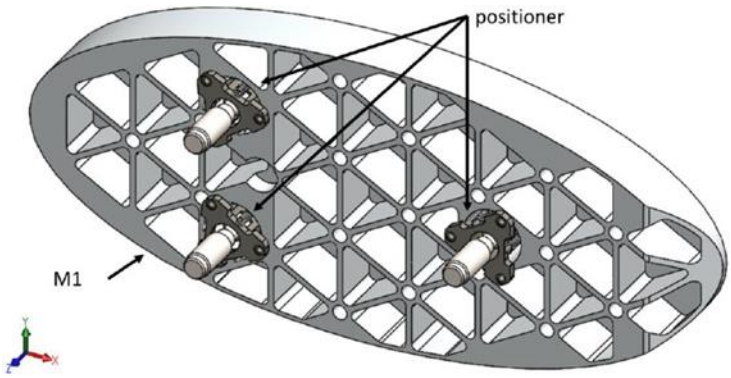

Figure 6.2: M1 and M3 fine alignment system

The M2 mirror is not directly attached to the actuators but on a CF structure. The mirror is clamped with spring plunger on 3 semi-kinematic contact points as shown below. To protect the mirror surface, holder surface get a PTFE impregnated of glass fiber tissue with thickness 0.12 mm.

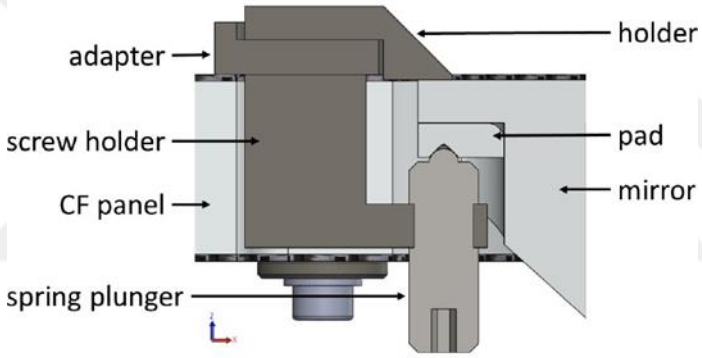

Figure 6.3: Mirror mount attachment

The M2 mirror angle is set with three semi-kinematic mounts fixed on the panel shown on Figure 6.4.

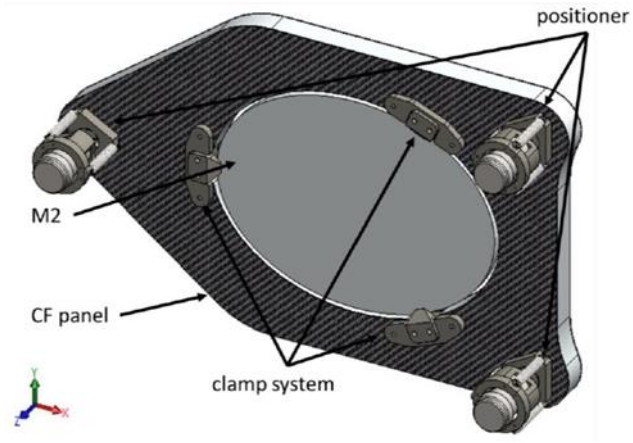

Figure 6.4: M2 allignment system

The mirror is clamped on the CF panel and the panel holds the housing by 3 mirror attachments.

6.1 Semi-Kinematic Module Principle

It is mentioned in section 3 that the mirror holders have semi-kinematic mount design to avoid hyperstatism and internal constrains due to the thermal expansion of mirrors or structure. This section presents the proposed solution.

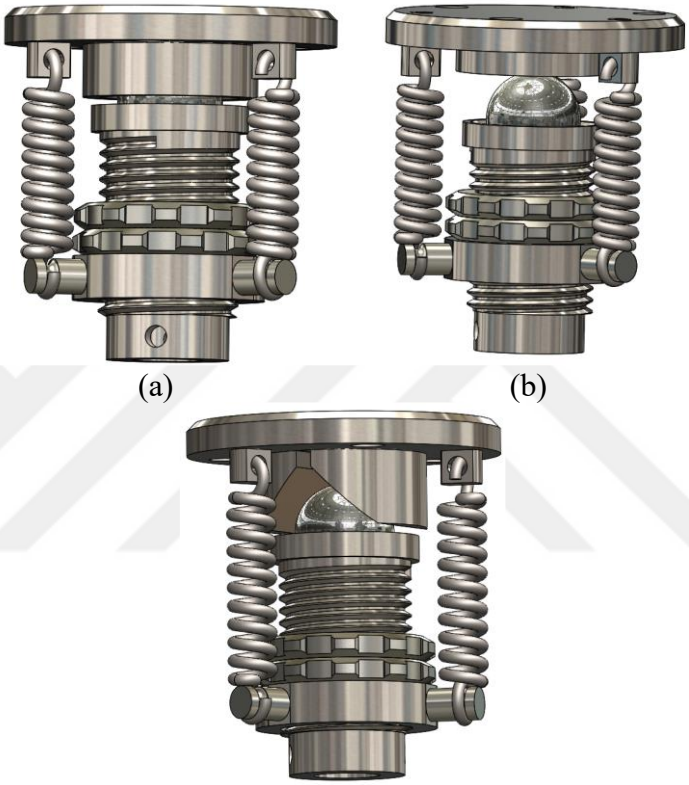

Figure 6.5: Semi-kinematic holder design a) pin hole, b) flat c) v channel

In order to simplify the computation, the three joints are considered as identical and take one third of the mirror mount mass, like the center of mass of the lower module is on the joints plane. In reality, minor number of other forces are acting on these joints but are ignored.

Estimating the maximal axial force, F_{pmax}, due to the gravity 14.7 N per joint (fixed by 1/3 of the lower mount weight) is found, the joint minimal axial stiffness k_{min} and the maximal axial peak to peak displacement d_{pp} with respect to the orientation can be estimated. Figure 6.6 shows the mechanism.

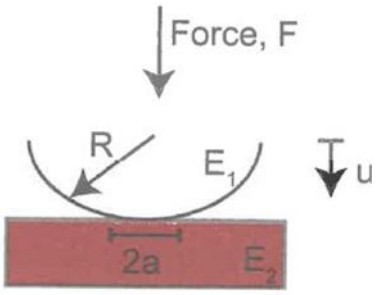

Figure 6.6: Preloaded ball deformation

$$u = 0.8\left(\frac{F^2 E_e^2}{R}\right)^{1/3} \tag{17}$$

$$a = 0.9(F\ R\ E_e)^{1/3} \tag{18}$$

$$k = \frac{dF}{du} = 1.875\left(\frac{R\ F}{E_e^2}\right)^{1/3} \tag{19}$$

$$E_e = \frac{1 - v_1^2}{E_1} + \frac{1 - v_2^2}{E_2} \tag{20}$$

$$\sigma_{c\ max} = 1.5\frac{F}{\pi a^2} \tag{21}$$

Where the variables are listed in the table below.

Table 6.1: Variable table

Variable	Value	Unit
E_1	650000	N/mm^2
v_1	0.24	-
E_2	650000	N/mm^2
v_2	0.24	-
R	6	Mm
F_{pc}	114	N

By inserting the numbers into equation 6.4, E_e can be found as following;

$$E_e = 2.9\ 10^{-6}\ mm^2/N \tag{22}$$

There are 3 springs mounted in parallel, so F becomes 3 times F_{PC}. The semi-kinematic stiffness can be calculated as;

$$k_{min} = 1.875\left(\frac{R\,F}{E_e^2}\right)^{1/3} = 117.17\ 10^3\ N/mm \tag{23}$$

$dF_{\max}$ is calculated as 29.43 N. It is defined by the peak to peak gravity force which acts on one of the joint of the mirror with respect to its orientation (which is estimated equivalent to 2/3 of the mirror gravity force). Then, the lower mount peak-to-peak displacement can be calculated as;

$$d_{pp} = \frac{dF_{max}}{k_{min}} = \frac{30}{117.17\ 10^3} = 0.26\ \mu m \tag{24}$$

Considering the stated hypothesis, figure 6.7 presents the axial displacement of each mirror mounted on semi-kinematic joints with respect to the mirror's orientation.

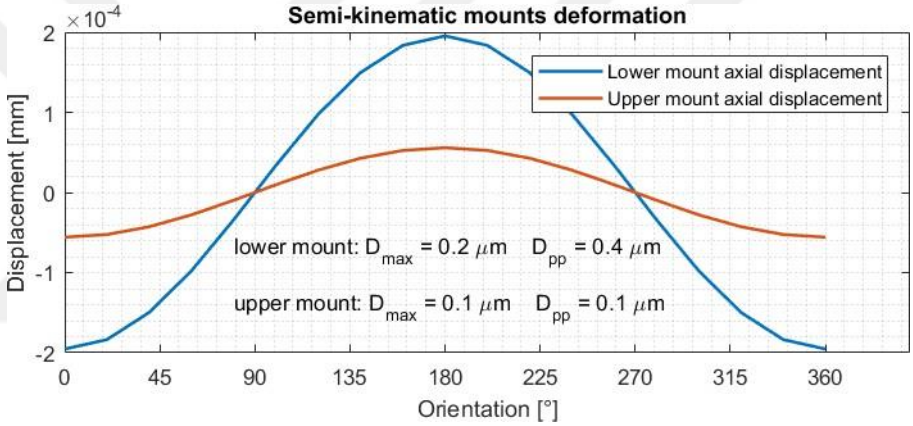

Figure 6.7: Semi-kinematic joint axial deformation wrt derotator orientation

Maximal lower mount displacement is about 0.2 μm and maximal upper mount displacement is about 0.1 μm.

The lower mount peak to peak displacement is about 0.4 μm. The upper mirror peak to peak displacement is about 0.1 μm. It can be said that this amount of error can be compensated by mirror the mirrors and the other optic instruments coming after the derotator.

7. SETTING FLANGE DESIGN

This section aiming to explain sub components and calculations made for the setting flange. Section 3 explains the functionality and role of the setting flange.

Figure 7.1 shows exploded view of 2 main adjustment mechanisms of the flange; dx-dy setting mechanism and rx-ry setting mechanism. Adjustment screws manipulate both of the systems. The rx-ry setting mechanism has also 3 ball joint system.

Figure 7.1: Flange components

The differential screw mechanisms slide the setting flange on x and y axis. The ball joints allow to adjust parallelism of the setting flange according to the reference surface.

7.1 The dx and dy Setting Mechanism

Differential screws are used to set these degrees of freedom. dx and dy DoF will be set using 2 differential screw modules. rx and r will be set using 3 ball joint modules that also integrate differential screws. Differential screw is made of two different diameter and pitch with same hand direction. This allows one part to be moved relative to the other with the pitch difference of 0.25mm as described below. Differential screw is manually adjustable with a standard hexagonal key.

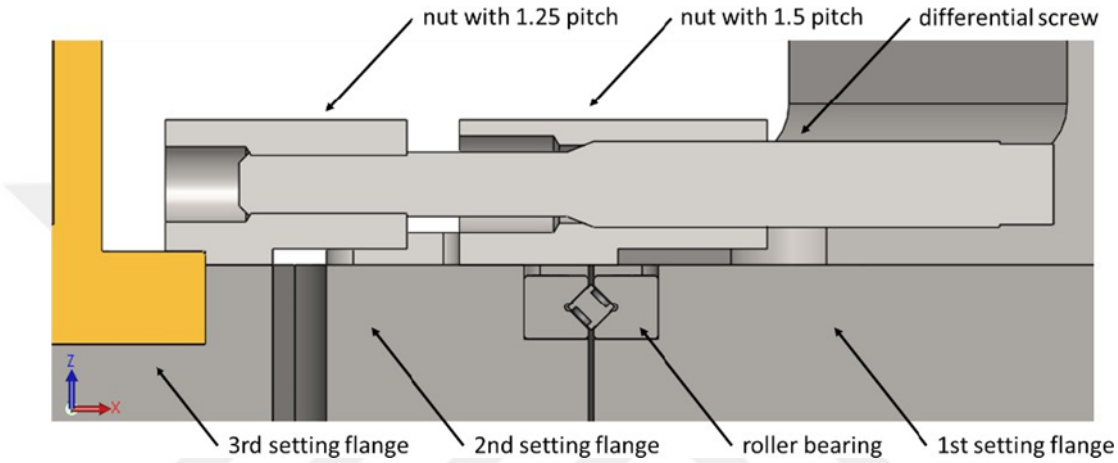

Figure 7.2: Differential screw mechanism

X axis linear bearings are fixed on the top and bottom of the setting flange in order to slide setting flange. *Y* axis linear bearings are fixed on the left and right side of the setting flange. By turning the differential screw, the derotator changes its position along the screw axis. The differential screws are preconditioned by springs. The aim of this, stabilizing the adjustment system. The setting flange can have 20 mm of translation on dx and dy axis.

7.2 The rx and ry Setting Mechanism

A support shaft is screwed in the support flange. Then a linear bearing is mounted on it in order to guide the setting flange. On the linear bearing is mounted an adaptor socket and a ball bearing. Then a carter is used to attach the ball bearing on the setting flange.

Figure 7.3 shows the mechanism by section view. The setting is drove by the differential screw (in the center). The center part of the differential screw in flexible in order to allow the alignment of the setting flange.

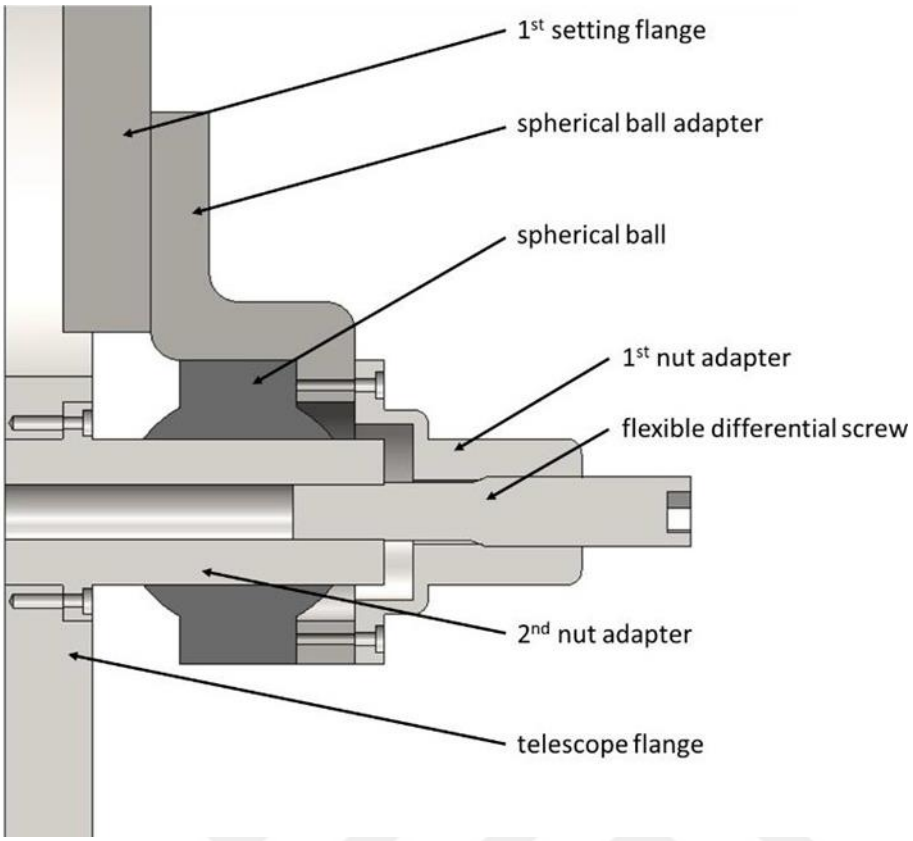

Figure 7.3: Differential screw

This mechanism is design to complete fine alignment after the derotator placed in the telescope fork hole.

7.3 Adjustment Screws Design

The idea is to have two different threads on a single displacement screw. One of the thread pitches is a bit smaller than the other. Then the difference of the two pitches is the new pitch of the screw. This solution will be use as precision actuators of the setting flange. The benefit of this technique is to support high load keeping high accuracy.

$$TP_{eff} = TP_2 - TP_1 \tag{25}$$

7.3.1 Setting resolution

Since the setting flange needs manipulators in order to set derotator alignment, the simplest solution is to use differential screws. Figure 7.4 shows the mechanism.

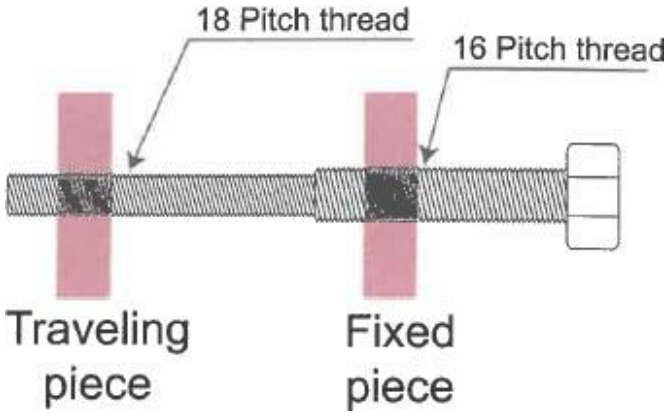

Figure 7.4: Differential screw

The idea is to obtain a setting resolution that is enough high to set the derotator axis on the telescope axis. Differential screws are used. For the calculations, it is state that 1 arcsec resolution is enough to set the parallelism.

If a standard metric fine pitch is chosen for the differential screw as following;

$$TP_{eff} = 1.25 - 1.0 = 0.25\ mm \tag{26}$$

And it can be assumed that the limit of resolution in rotation at the screw level is 3°, each step will make a displacement *d* of:

$$d = \frac{TP_{eff}}{360/3} = \frac{0.25}{120} = 2.08\ 10^{-3}\ mm \tag{27}$$

Then from the Solidworks design, the distance is measured as *l* between one setting point and the two others is 480 mm. The flange angular resolution can be calculated as the following;

$$Resolution = atan\left(\frac{d}{l}\right) = 0.248\ 10^{-3} deg. = 0.89'' \tag{28}$$

It can be said that the resolution of the system is quiet enough for fine alignment.

7.4 Ball Joint System Design

This mechanism allows to adjust flatness of the setting flange according to the reference surface. The side view of the ball joints and the length between them are illustrated in the figure 7.5.

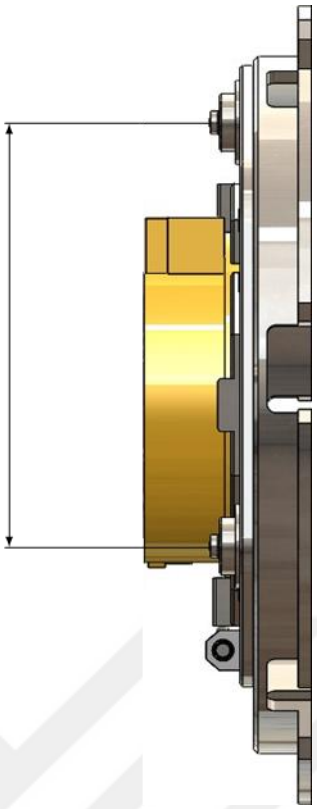

Figure 7.5: Length l

These modules must allow *rx*, *ry* and *dz* motion and stay as rigid as possible in the radial direction. Then, axially, the system must allow a setting stroke in order to set the flange alignment. The axial adjustment will be carried out by a differential screw.

7.4.1 Maximum axial load check

In order to control the screws size, the differential screws maximum axial and shear stress will be estimated.

First, the tensile strength is calculated:

$$\sigma_{tensile} = \frac{F_{load}}{A_s} = \frac{1250}{84.3} = 14.83\ MPa \tag{29}$$

Where F_{load} is axial load and A_s is the bolt smallest cross section area.

$$tan\emptyset = \frac{P}{d_2\pi} = \frac{1.75}{\pi\ 10.863} = 0.0813 \tag{30}$$

Where Ø is helicoidal pitch angle, P is the pitch and d_2 is the average diameter.

$$tan(\rho') = \frac{\mu}{cos(\alpha/2)} = \frac{0.0513}{\cos(1.048/2)} = 0.0592 \quad (31)$$

Where the α is the thread angle and μ is the coefficient of friction.

It is known that;

$$\mu = tan(\rho) \quad (32)$$

Then;

$$d_s = \frac{(d_2 + d_3)}{2} = \frac{10.863 + 9.853}{2} = 10.358\ mm \quad (33)$$

And

$$\tau = \frac{F\frac{d_2}{2}tan(\emptyset + \rho')}{\frac{\pi d_s^4}{32}}\frac{d_s}{2} = 3.42\ MPa \quad (34)$$

Where τ is the torsion, ρ' is calculation parameter in rad and d_3 is bolt smallest diameter. Then, the n equivalent stress can be calculated.

$$\sigma_{eq} = \sqrt{\sigma^2 + 3\,\tau^2} = 15.97\ MPa \quad (35)$$

The bolt is selected as M12 and 8.8 quality. Its yield strength is 640 MPa which is much larger than the stress applied on the bolt.

7.4.1.1 Strength check for the threads

The thread quantity can be found as the following;

$$z = \frac{m}{P} = \frac{20}{1.75} = 11 \quad (36)$$

Where m is the thread length. The load can be found by the formula as the following;

$$\sigma_{load} = \frac{F_{load}}{z\frac{\pi}{4}(d^2 - d_1^2)} \quad (37)$$

Where d_1 is the bolt shaft diameter.

Since σ_{yield} is 640 MPa, $\tau_{yield} > \sigma_{load}$ and it can be said that the threads are safe.

$$\tau = \frac{F}{z\pi d_1(a\ h)} = 0.577\ 640 = 369.28\ MPa \tag{38}$$

Where h is the thread height.

$$\tau_{yield} = 0.577\ \sigma_{yield} = 727\ MPa \tag{39}$$

Since $\tau_{yield} > \tau$ threads are safe.

7.4.2 Differential screw flexure control

This subsection is dedicated to control the dimensioning of the r_x and r_y setting module differential screw.

The starting point is having the hypothesis that the maximal axial stroke s_{max} between 2 modules is 2 mm. In this case the flange angle θ_{flange} can be calculated as following;

$$\theta_{flange} = arctan\left(\frac{s_{max}}{l}\right) = arctan\left(\frac{2}{480}\right) = 0.24^0 \tag{40}$$

The found angle is taken as the screw deformation. If it is assumed that one side of the screw is fixed, and the deformation is symetric, the screw deflection d_{screw} can be estimated by the formula below;

$$d_{screw} = \frac{l_{screw}}{2} tan\theta_{flange} = \frac{67}{2} tan(0.24) = 0.14\ mm \tag{41}$$

Where l_{screw} is the screw length. Figure 7.6 shows the deflection values.

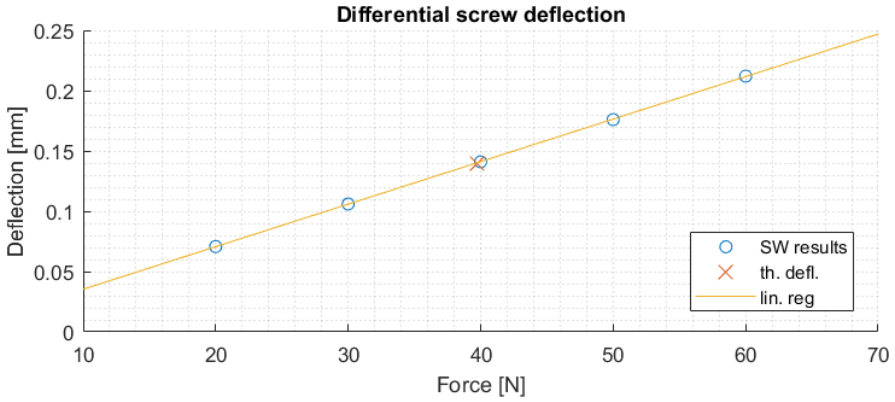

Figure 7.6: Differential screw deflection

Then, it can be check that if the deformation lower then the yield strength. One side of the screw is fixed and a perpendicular force F_{perp} is applied to the other.

It can be seen that the computed deflection (0.14 mm) is reached when the force is about 40 N. Figure 7.7 shows the solidworks model of the differential screw deflection model.

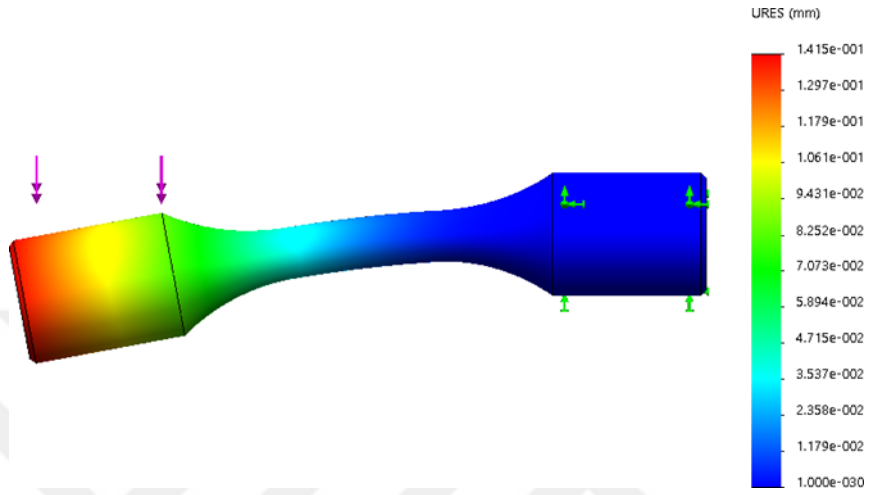

Figure 7.7: Differential screw deflection model

According to the fem analysis, with a load of 40 N, the maximal internal constaint is about 110.9 MPa. It can be concluded as the design is safe.

7.4.3 Support axis shear stress control

This subsection is dedicated to control the dimensioning of the r_x and r_y setting module flange support.

First, the theoretical shear stress that support each shaft making the hypothesis that the load is equally distributed is estimated.

According to the mechanical design, there are 3 shafts. Each one has an external diameter, d_{ext}, as 20mm and an internal diameter, d_{int}, as 13mm. Then we can compute the cross-section area which is called as A_{shaft}.

$$A_{shaft} = \frac{\pi}{4}(d_{ext}^2 + d_{int}^2)\frac{\pi}{4}20^2 + 13^2 = 181.42mm^2 \qquad (42)$$

Knowing that the load of the derotator, setting flange and motor is about 157kg.

The shear stress on each shaft can be estimated as the following;

$$\sigma_{shaft} = \frac{F_{load}}{3A_{shaft}} = \frac{m_{load}g}{3A_{shaft}} = \frac{157\ (9.81)}{3\ (181.42)} = 2.83\ N/mm^2 \qquad (43)$$

Typically, for standard steel $R_{eg} \approx 450$ N/mm2. Since $\sigma_{shaft} << R_{eg}$, it can be said that the design is safe.

8. MATERIAL SELECTION

This chapter is dedicated to describe the material selection. In order to achieve an optimal derotator structure, stiffness is a key element. However, it is not the only criteria; cost, feasibility, temperature dilatation, manufacturing processes and weight are critical points too.

Firstly, the material list is made to achieve best mechanical properties. CTE properties of the materials are very important because of the working and survival temperature specifications of the derotator. If the selected material couples cause internal stress by the thermal dilatation, it can be concluded with shifting optical axis.

Then, the list of materials is filtered according to availability and manufacturability. Since this device is actually manufactured, finding a manufacturer was pretty tough and the material list got narrowed also by manufacturers. Another real-life challenge was the total cost. Finally, the balance between cost and benefit is made and following sections explain all.

8.1 Material Choice for Housing and Its Miscellaneous Parts

This section is dedicated to compare different materials that could be used to design the housing. Since the housing holds all the optics, material choice of it is very critical. This is because it has direct effect on the image quality of the derotator. The cost and density ratios are based on equal axial strength.

As a first approach, criteiras are set for the materials. Low density and high strength materials are useful to be used. In this way, the material families are reviewed by using Ashby charts. It is understood that composites and metals are fit the requirements. Figure 8.1 shows that composite materials stiffness is close to the metals, however the density is significantly lower.

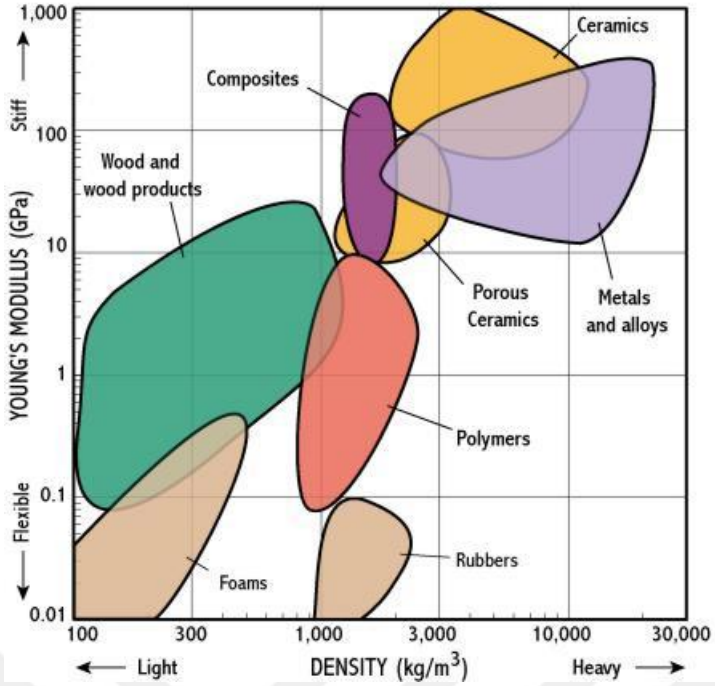

Figure 8.1: Young modulus, density Ashby chart

Table 8.1 shows the candidate materials for the housing. Carbon fiber has the lowest CTE, the lowest density and the highest Young modulus. It is technically the best choice accordingly.

Table 8.1: Material comparison

Material	$\rho(kg/m^3)$	$\alpha(K^{-1})$	E(GPa)	ν
Invar	8130	$2\ 10^{-6}$	145	0.23
Steel	7850	$11\ 10^{-6}$	210	0.3
Aluminum	2700	$23\ 10^{-6}$	70	0.34
Carbon Fiber	1800	$0.5\ 10^{-6}$	305	0.5
Titanium	4540	$8.5\ 10^{-6}$	110	0.34

However, its high cost in comparison with the other materials is a drawback. The also shows that Invar is a good candidate material for small parts.

The search of the manufacturers ended up with a company which works for Swiss Space Agency. It is decided that the housing panels is made of carbon fiber sandwich panels which has aluminum honeycomb. The panels are connecting to each other with screws and barrels which are made of Invar. The FEM analysis on chapter 9 confirms that there is no conflict between this material couple.

8.2 Material Choice for Mirrors

The material choice of the mirrors is very critical in terms of their optical performance. There are 2 main materials which are using for this purpose in industry; zerodur and ule.

Both of the materials have similar technical properties and they are trade marks too. Since the agreement is made with the mirro manufacturer Schott, the material is automatically selected as Zerodur. It has very low CTE which is close to zero in a certain temperature range and it has excellent properties to be selected as a mirror body. Table 8.2 states its main properties.

Table 8.2: Schott Zerodur properties

Properties	value	unit
ρ	2530	kg/m^3
E	91000	N/mm^2
ν	0.24	-
G	36700	N/mm^2
T	-	N/mm^2
R_m	-	N/mm^2
$R_{p0.2}$	-	N/mm^2
α	$0.05\ 10^{-6}$	K^{-1}
K	1.64	W/mK
c	821	J/kgK
E_0	-	V

8.2.1 Mirror coating

Usually mirror coatings are chosen according to the analyzed light spectrum. In this case, the coating is chosen as same as telescope mirrors coating which is aluminum.

The total reflectivity of the derotator, considering the average of the P and S polarisation directions for aluminium coating and silver coating. This is because the derotator mirrors cannot be easily removed (for periodic recoating), and the transmission in the visible domain must be as high as possible in order to get enough photons for the AO system wavefront sensor. Protected silver is the obvious choice. The average P+S polarisation reflectivity for each mirror, when considered in normal incidence, shall follow the curve shown in Figure 8.2.

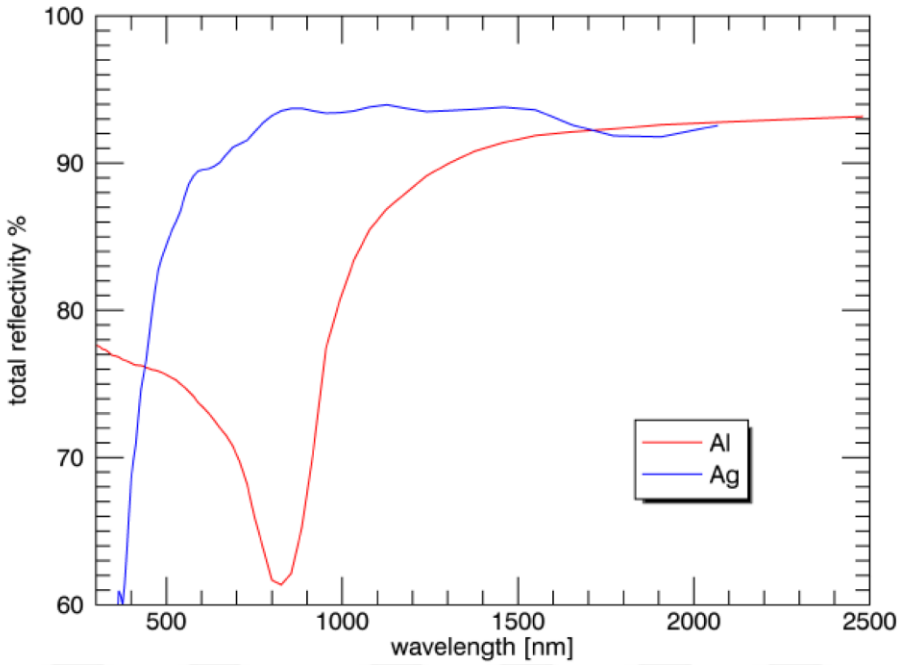

Figure 8.2: Total transmission for aluminium and silver coating

Total transmission of the derotator for aluminium and silver coating, considering the incidence angles are taken into account. Also, the silver coating specification for each mirror for in normal incidence is considered.

8.3 Material Selection for Miscellenious Parts

Invar has good mechanical properties and it is a good couple with carbon fiber housing. However, there are another alternative material for flanges and housing socket.

Flexure materials are recommended such as Stainless steel, Titanium, Invar 36, Beryllium copper, aluminium (6061-T6).

Table 8.3 Material comparison

Properties	403 Steel	AMS 329	S235JRG2	AISI 1213
ρ	7800 kg/m^3	7800 kg/m^3	-	7800 kg/m^3
E	210GPa	- N/mm^2	210GPa	200GPa
ν	0.27	-	0.28	0.29
G	76GPa	- N/mm^2	79GPa	80GPa
T	- N/mm^2	- N/mm^2	7800 N/mm^2	- N/mm^2
R_m	- N/mm^2	620 N/mm^2	360 N/mm^2	385 N/mm^2
$R_{p0.2}$	- N/mm^2	620 N/mm^2	235 N/mm^2	240 N/mm^2
α	4.4 10^{-6}K^{-1}	14.4.10^{-6}K^{-1}	11 10^{-6} K^{-1}	11.5 10^{-6} K^{-1}
K	- W/mK	- W/mK	14 W/mK	51.9 W/mK
c	460 J/kgK	460 J/kgK	440 J/kgK	472 J/kgK

8.3.1 Housing socket and setting flange

It is decided to make the setting flange and the housing socket from the same material in order to have harmony between the parts. In this way, the workshop confirms the availability and manufacturability of the parts with S355.

8.3.2 Support flange

The support flange has 1.44m diameter and it limits the manufacturability. 1.5714 which is a hardening steel is adviced by the workshop because of its availability for the size of the support flange. Besides, it has good machinability and cheaper than the other alternatives i.e., S355.

There is big pro of using S355 and 1.5714 which is corrosion. Parts of the derotator should be insensitive to corrosion. So, all the parts are zinc plated.

8.3.3 Counterweight

Counter weight material is chosen as 1.0038 steel because it has high density. This feature helps to reach desired weight with minimal volume. and easy to supply.

8.4 Summary

Tthe materials that stand out with lowest CTE are Zerodur, Carbon Fiber, and Invar. A low CTE module and a high young module are guidelines for the housing part as they reduce the deformation and stress that could create a mirror misalignment and a wavefront error. Since the mirrors are very critical in terms of flatness, they are be made of Zerodur. CF gets the highest ratio Young modulus by density; it is technically the material used for the biggest parts of the housing. As Invar is less expensive than other low CTE parts it is chosen for contact adapter between mirror and CF parts.

Steel is chosen for the largest part that could cost more due to greater weight. The chosen steel maximizes stiffness and minimize CTE.

Table 8.4 Material list

Material	Component	CTE	E (GPa)	Density (kg/m^3)
Steel protected with zinc passivated (S355)	Flanges, nuts, adapters, differential screws	11 10^{-6}	210	7800
Inglidur J / RN33	Spherical ball, flange bearing	-	-	-
Hardened tool steel (1.2842)	Linear bearing	11 10^{-6}	210	7610
Carbon fiber with aluminum honeycomb	Housing panels	0.6 10^{-6}	260	1800
Invar protected with black chromium	Housng adapters	1.5 10^{-6}	140	8150
Zerodur	Mirrors	0.05 10^{-6}	90	2500

9. STRUCTURAL ANALYSIS

This chapter aims to provide thermal and structural analysis for Derotator housing under changing ambient temperature.

Derotator is designed in consideration of survival mode. It is defined between -30^0 C to $+30^0$ C. This condition is used for the evaluation of housing structural rigidity. The operational mode is defined between -15^0 C to $+15^0$ C. It is used for deformation examination of the housing which is important for the optical axis. All necessary internal components are covered for all analysis.

9.1 Geometry

The geometry is taken form the Solidworks model and imported to Ansys. The structure includes 417 parts. Figure 9.1 shows the original structure, part quantity information and coordinate system.

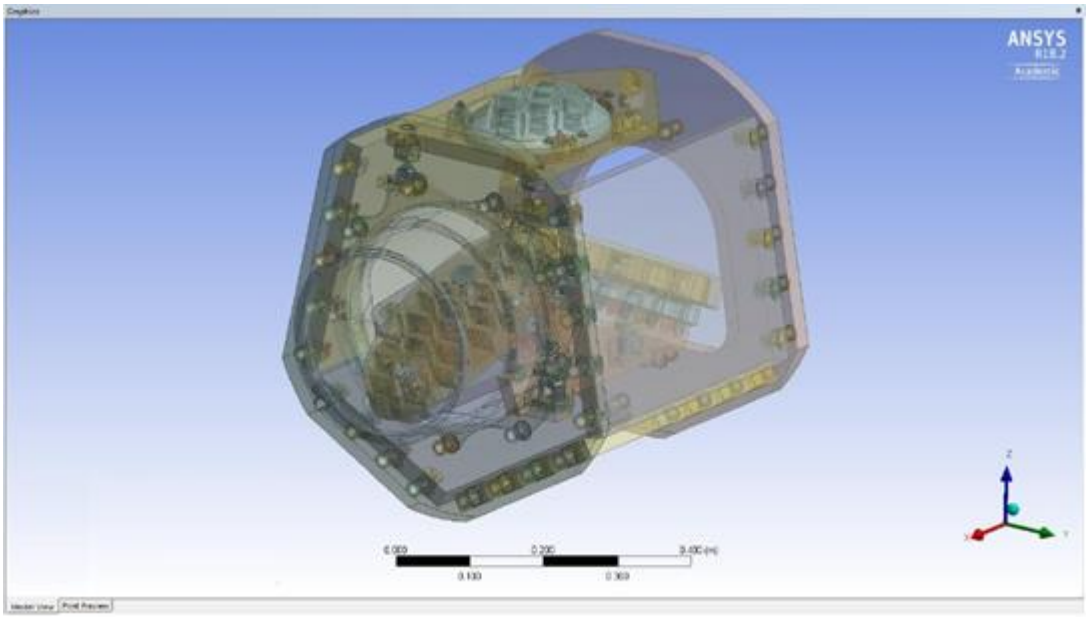

Figure 9.1: Analised Derotator structure

Since the analysis must be computationally economic, some parts are removed from the assembly. All the screws, washers, nuts and bushings are excluded from the analysis. The assembly has 307 parts to be analyzed.

The assembly includes minor simplifications. Figure 9.2 shows the carbonfiber sandwich structure is merged as one piece instead of three pieces. Thanks to that, thin layer surface calculations are eliminated.

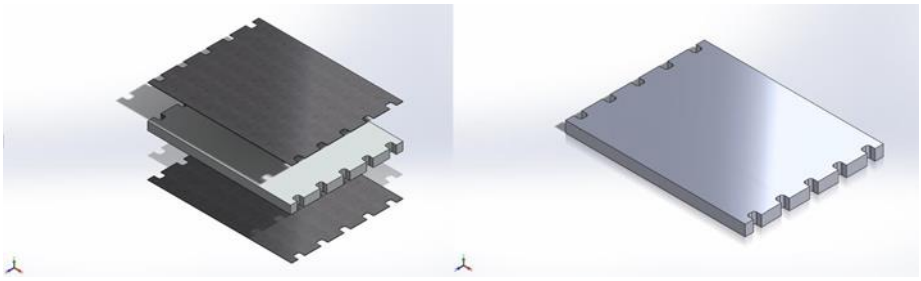

(a) (b)

Figure 9.2: a) Original part and b) simplified carbonfiber panel

Figure 9.3 shows another simplification has been done on the micrometer subassembly.

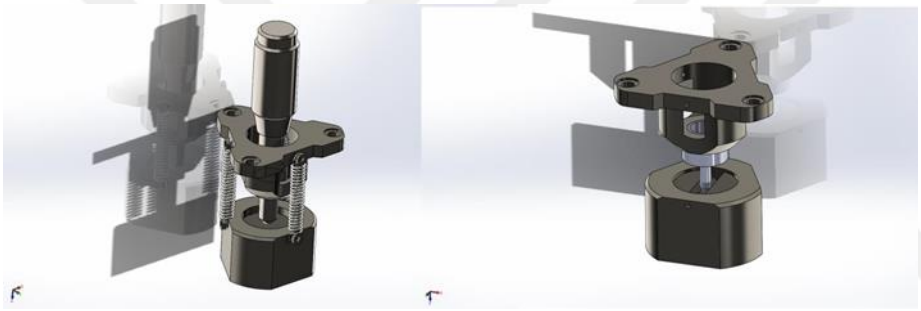

(a) (b)

Figure 9.3: a) Original part and b) Simplified micrometer subsystem

The subassembly is consisting of 3 tension springs, 6 connection parts and a micrometer. Since this subsystem is designed to be rigid, it is replaced with a rigid dummy part. The dummy part has the same mechanic function with the predecessor subassembly.

9.2 Ansys Model

The model includes standard earth gravity, fixed support and thermal condition. It is configured for different temperature scenarios. Initially, temperature difference is not applied to the structure. Then, two different temperature intervals are applied. The rotation of the device is considered. In this way, working temperature analysis is applied for 900 and 1800 angle which are the extremum points of the rotation.

The analysis includes 3008155 nodes and 1666889 elements for mesh evaluation. It is optimized for workstations ram capacity which is 32 GB.

The positive direction of the Z axis and the applied standard earth gravity. The blue part on Figure 9.4 shows the fix faces;

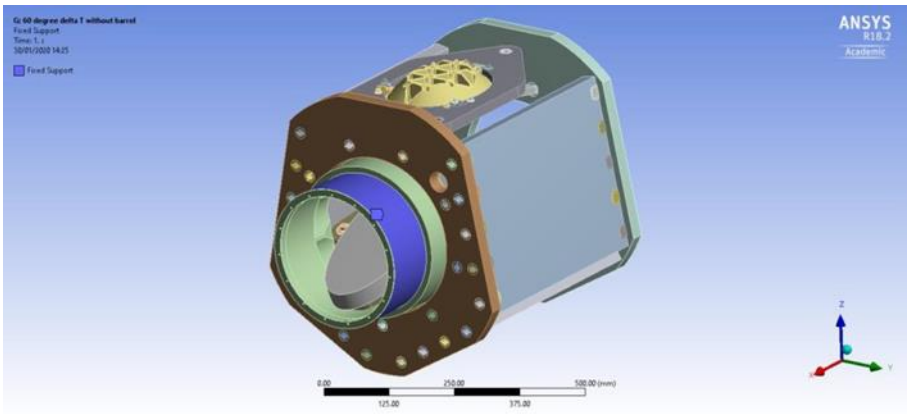

Figure 9.4: Fixed support

The red color regions on Figure 9.5 shows the parts which are affected by applied thermal condition;

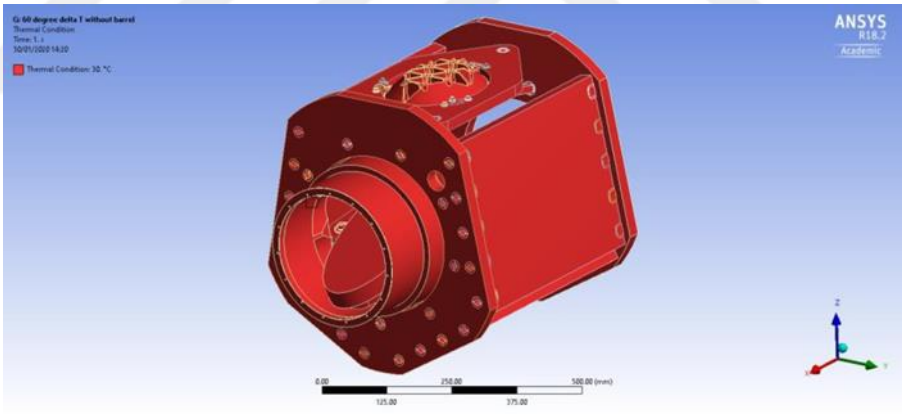

Figure 9.5: Applied temperature difference

Thermal difference values are taken for survival and working temperatures.

9.3 Solution

All the thermal tests are applied on the structure which is described on the previous section. Since the acceptance test procedure only concerns about the housing, the results and visuals are filtered accordingly.

Table 9.1 provides all the test results in megapascal. The results are representing the resultant deformations on three axes.

Table 9.1: Total deformation results

Properties	0^0 Rotation	90^0 Rotation	180^0 Rotation
Not applied	5.7 MPa	10.9 MPa	5.7 MPa
From -15^0 C to $+15^0$ C	16.7 MPa	18.1 MPa	14.3 MPa

Table 9.2 gives detailed directional deformation information on the operational mode. The results are in micrometer.

Table 9.2: Detailed deformation information

Plane	0^0 Rotation	90^0 Rotation	180^0 Rotation
X	7.3 μm	7.6 μm	7.5 μm
Y	13.4 μm	6.8 μm	12.4 μm
Z	6 μm	10 μm	6.7 μm

Table 9.3 shows the equivalent stresses according to the von-misses' criteria. The results are in MPa.

Table 9.3: Equivalent stress results

Thermal Condition	0^0 Rotation	90^0 Rotation	180^0 Rotation
From -15^0 C to $+15^0$ C	23.9 MPa	45.3 MPa	44.3 MPa
From -30^0 C to $+30^0$ C	45.5 MPa	52.2 MPa	49.6 MPa

All the results are explained detaily in the next section.

9.4 Discussion

Table 9.1 presents the deformation values for operational mode. Second line of table 9.1 is created to be a reference to make an easy comparison for the reviewer. It shows the theoretical values if the temperature doesn't affect the system. The third line shows the deformation on the operational mode. Since the system will not work in survival mode, it is not presented on Table 9.1. It is considered as an evaluation criterion for the structural rigidity on Table 9.3.

The highest deformation occurs on 90◦ rotation with amount of 18.1 micrometers. This is an expected case, since 90◦ is an extremum point.

Table 9.2 provides detailed deformation information for the operational mode. The highest deformation occurs on Y axis while Derotator is on the initial position. Since the Derotator is not symmetric, deformation values on 0 degree and 180 degree don't match but close to each other.

The deformation vectors on X, Y and Z plane are not perpendicular with each other. 90◦ rotation doesn't have individual extremum deformation values. However, it has biggest equivalent vector. The vector sum of each rotation is presented on table 9.1.

Table 9.3 presents the maximum equivalent stress developed in the housing. The first line presents the operational mode and the second line presents the survival mode. The highest deformation occurs on 90◦ rotation while the Derotator is in survival mode.

9.5 Conclusion

On this analysis, thermal and structural conditions are tested at the same time. Thermal conditions are taken as variable, but the loading parameter is considered as non-variable parameter due to the fix internal weight.

Table 9.1 shows the maximum total deformation as 18.1 micrometers. Since the evaluation criterion is 50 micrometers, it satisfies the expectation. On the other hand, 18.1 micrometer is low amount of deformation and it doesn't have a potential risk for the structural rigidity and optical performance.

The maximum stress acting on the housing is 52.2 MPa. It is fairly low amount of stress for the materials used in Derotator. The acting stress is lower than the yield stress of any material which are used for housing. It can be concluded that the maximum developed stress in the housing panels is not critical for rigidity.

10. MOTORIZATION

This chapter is explaining details about the rotational stage of the derotator. This stage is the center piece of the system and the sub-assemblies are coming together on this part. It means the rotational stage has also structural role on the derotator assembly.

10.1 Derotation Speed

K-mirror type derotators rotate the image twice as fast as its own rotation. By using this information, the derotator should rotate in the opposite direction of the rotation of field via half speed of it.

10.1.1 Parallactic angle

The parallactic angle is the orientation of the optical field, shown as q, which is the angle between the celestial meridian of the observed object and the arc connecting the zenith to the object [14].

Marke de Koe states in the study [10] that the field rotation speed for an alt-azimuthal mount is as a function of the telescope altitude angle, azimuth, the observer's latitude and the rotational speed of the earth.

$$\frac{dq}{dt} = \omega_{field} = -\omega_{earth}\cos(Lat)\frac{\cos(Az)}{\cos(Alt)} \qquad (10.44)$$

For DAG Telescope, the latitude is $39^0 47'00"$ N, and knowing the period of rotation of the earth T_{earth} is 23h 56m 4s, then ω_{earth} can be found as 72.92 10^{-6} rad/s. Then:

$$\omega_{field} = -72.92\ 10^{-6}\cos(39^0 47'00")\frac{\cos(Az)}{\cos(Alt)} \qquad (10.2)$$

So, the function for the specific parallactic angle is achieved.

$$\omega_{field} = 5.604\ 10^{-5}\frac{\cos(Az)}{\cos(Alt)}\ rad/s \qquad (10.3)$$

The variables are stated in Table 10.1 below.

Table 10.1: Statements

Variable	Explanation	Unit
ω_{field}	Field of view angle speed	rad/s
T_{earth}	Earth rotation period in sideral time	s
ω_{earth}	Earth rotation speed in sideral time	rad/s
Lat	Observer latitude	rad
Az	Observer object azimuth	rad
Alt	Observed object altitude angle	rad

The field rotational speed is displayed (figure 10.1) for an elevation between 0^0 and 85^0 and an azimuth angle range of 0^0 to 360^0. To facilitate understanding, the rotation speed is displayed in ^{0}/ s.

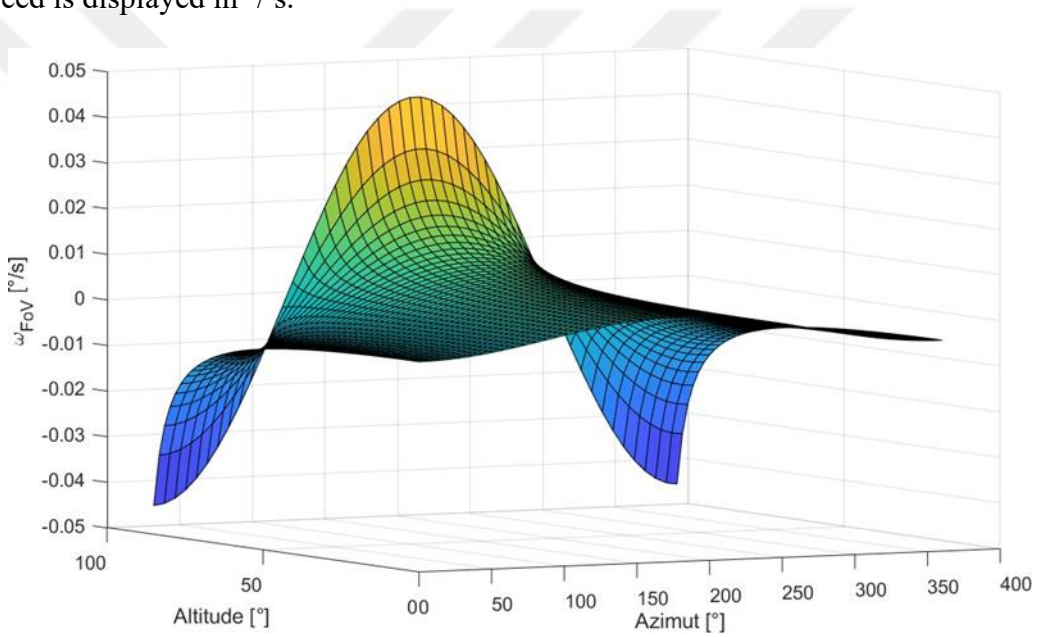

Figure 10.1: Field of view angular speed

For an elevation angle of 89.9^0, the maximal field of view rotational speed is 2.17^0/s.

10.1.2 Calculation of the derotator angular speed

The relationship between the rotation of the field and the derotator can be describe as;

$$\omega_{DRT} = -\frac{1}{2}\omega_{field} \tag{10.4}$$

It can be seen that the rotational speed of the derotator converges to infinity when the angle of elevation goes to the zenith. However, the angle of elevation can be very close to the zenith without exceeding the maximum rotation speed of the motor.

Figure 10.2 shows the derotator angular speed. For an elevation angle of 85^0, the derotator reaches a speed of 0.02^0/s and for angle of 89.9^0, the maximal rotational speed is about 1.1^0/s.

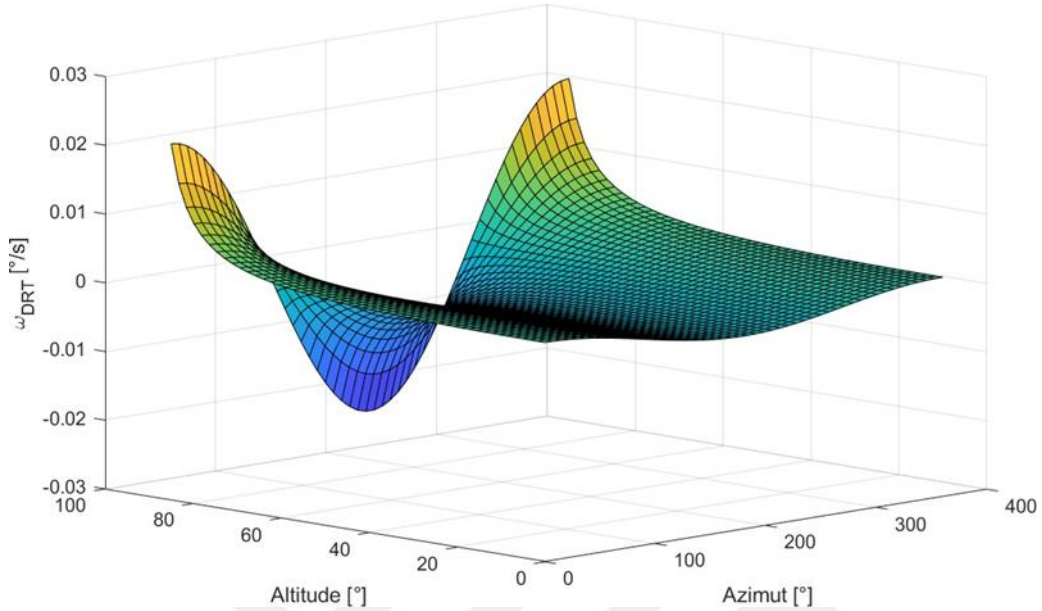

Figure 10.2: Derotator angular speed

From the point of view of the astronomers it can me more useful to see the field of view and derotator rotational speed with respect to the declination and time angle.

10.2 Rotational Stage

The first concern about the motor selection is the loading capacity. Since the optic path is directly affected by the rotational stage, the next concern is wobble and eccentricity. There are other concerns which are about accuracy, repeatability, minimum increment...

Newport is one of the best companies in Turkey which has support for its products. RV350HAHLT has enough loading capacity for carrying derotator, very low eccentricity and wobble which can be compensated by optics. Its minimum increment is enough to follow telecopes motion. Lastly, its accuracy and repeatability are good enough for the optical systems coming after the derotaton on the optical path. The table 10.2 summarizes its characteristics.

10.2.1 Off-axis maximum load check

This section is dedicated to estimate the maximum off-axis load Q_V that can be mounted on the RV350HAHLT. Figure 10.3 shows the visual of the motor.

Figure 10.3: Rv350halt

The datasheet states that the acceptable off-center load for a horizontal rotation axis is:

$$Q_v = \leq \frac{C_z/2}{(1 + D/a)} \tag{10.5}$$

Table 10.2 states the numerical values:

Table 10.2: Off-center load specs

Variable	Value	Unit	Explanation
D	0.0873	m	Cantilever (from the mechanical design)
a	0.1	m	Construction parameter
C_z	6500	N	Normal centered load capacity

The maximum off-axis load Q_{Vmax} is calculated as 1735 N, which is enough for carrying the system. The load of the derotator mount is about 1000 N which is 58% of the allowable load. It can be said that the selected component is safe for the design.

10.2.2 RV350HAHLT rotational stage specs

In order to explain the motor characteristics clearly, some definitions and important points are mentioned. This subsection is based on the information shared by the Newport Company via its web site [20].

10.2.2.1 Uni-directional repeatability

The uni-directional performance is presented on the figure 10.4. All measurements are done by approaching from the same direction and they are repeated five times. Each position is representing by the dots.

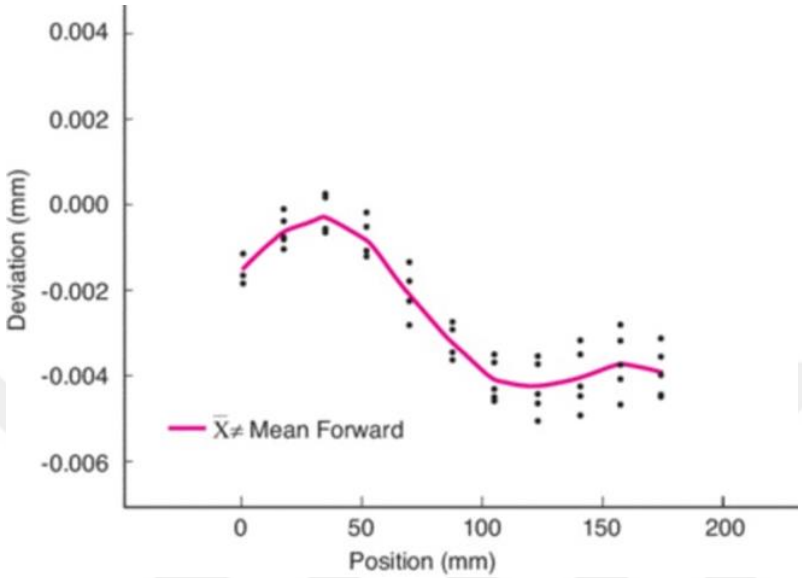

Figure 10.4: Uni-directional repeatability

10.2.2.2 Bi-directional repeatability

The bi-directional performance is represented on the figure 10.5. Ten data are recorded for each position; five for the forward and 5 for the reverse directions. Same as the previous figure, the dots represent the values at each position.

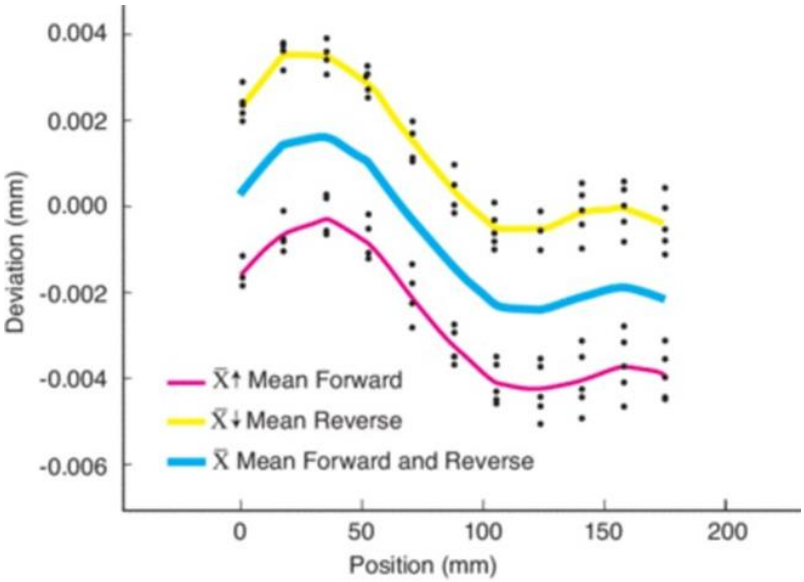

Figure 10.5: Bi-directional repeatability

11. ALIGNMENT-OPTICAL AXIS SETTING SYSTEM DESIGN

The derotator is made of two subsystems, the setting flange, and the housing. Derotator optical alignment is complicated due to the number of degrees of freedom.

The setting flange carry the housing and allow its alignment with 6 degrees of freedom. One of these degrees of freedom allows rotation of the housing along the optical axis by the motor. The housing contains the 3-mirror creating K-mirror structure that creates the field derotation.

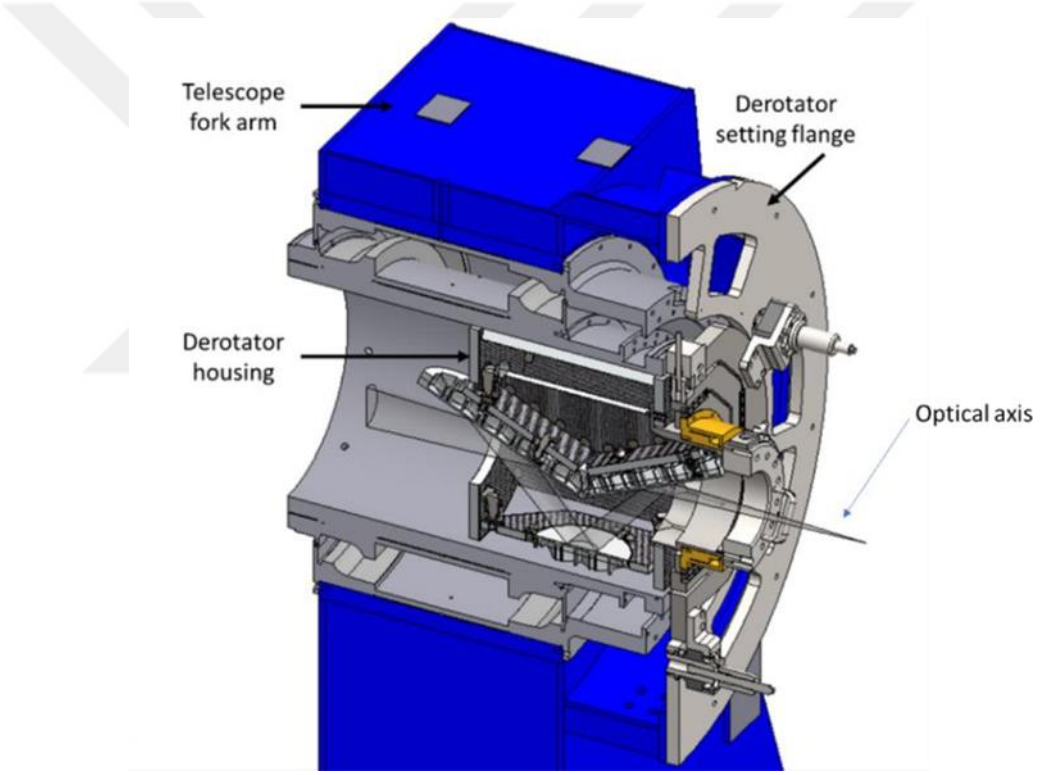

Figure 11.1: Derotator assembled on telescope arm

To make a proper alignment it is recommended aligning first mirrors into the housing. This structure is made of carbon fiber (CF) to improve stiffness and limit thermal dilatation. It contains 3 degrees of freedom (DoF) for each mirror and 3 additional DoF for the M1-M3 structure. Goal is to create an alignment of the 3 mirrors optical axis with the motor mechanical axis.

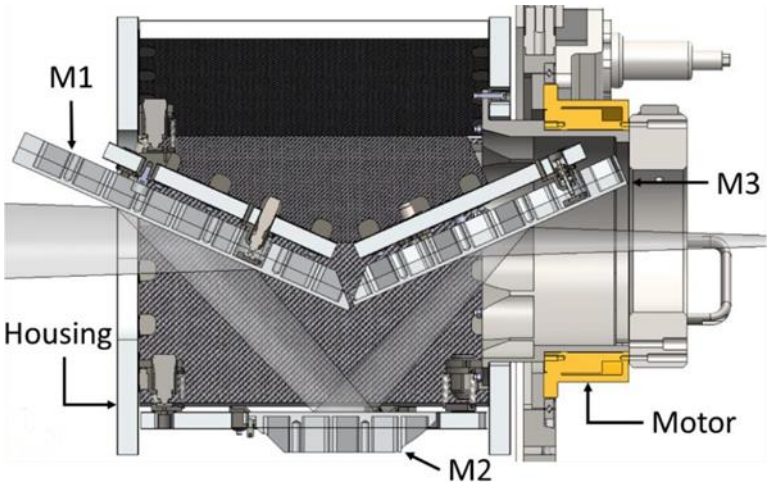

Figure 11.2: Cropped side view of derotator

Afterwards, the housing is assembled with the setting flange and its optical axis is aligned with the beam axis of the telescope.

11.1 Definition of Mechanical Axis

Mechanical axis is defined by the axis of rotation of the motor. It must be identified before defining the optical axis. Goal is to place a laser beam that will be coincident with the mechanical axis. Figure 11.3 show main elements of the setup.

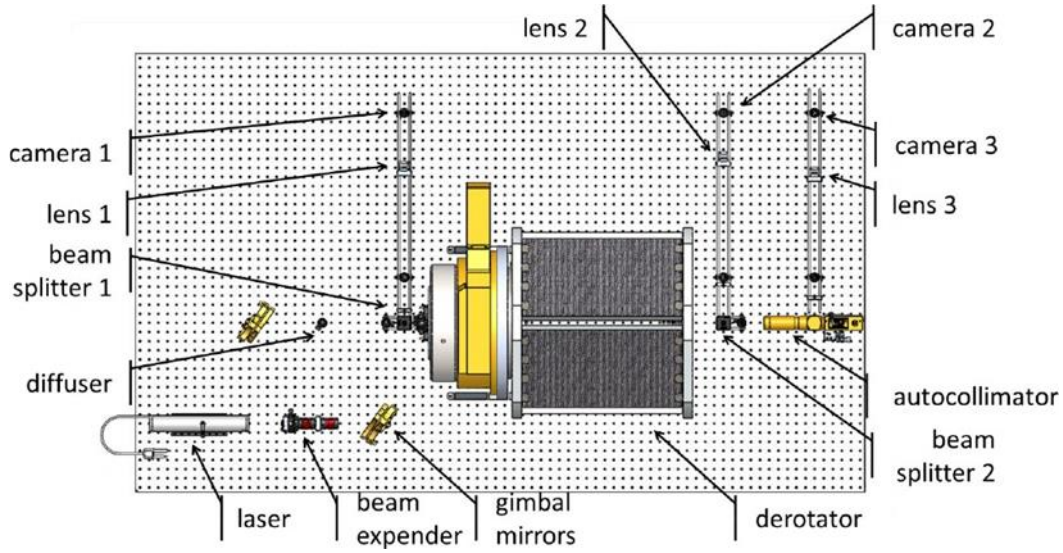

Figure 11.3: Top view of the alignment setup

Laser pass through a double beam expender that creates a collimated beam. Gimbal mirrors set position and angle of the laser beam. Two cameras observe respectively input and output laser position on reticle. An autocollimator measure laser angle on

the output side. Setup allow to place diffuser that prevent diffraction and neutral filter that prevent over-exposure on instrument. Figure 11.4 illusturates the setup.

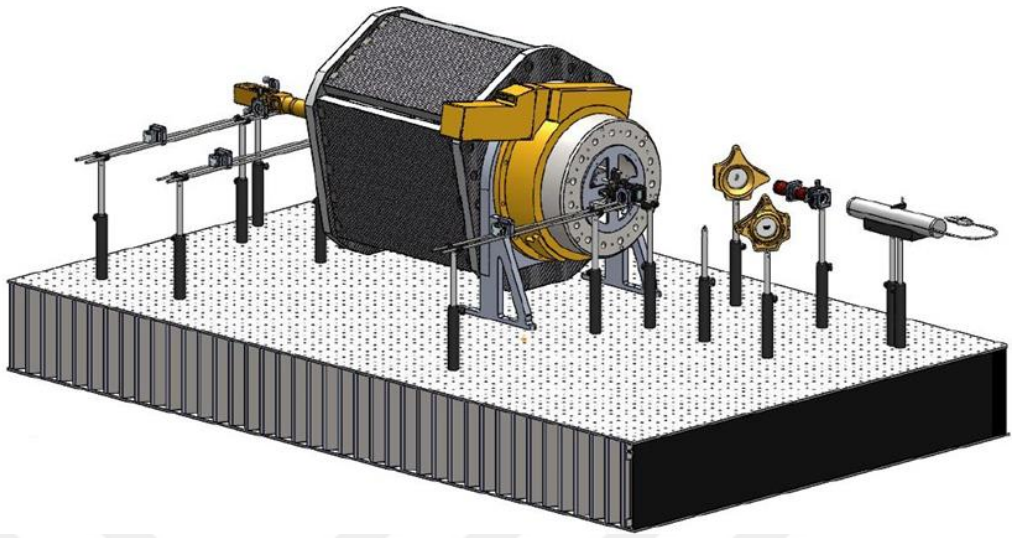

Figure 11.4: Tridimensional view of the alignment setup

Laser is a coherent light that could create diffraction. This effect can be minimized using thin glass element, large aperture, large beam, and diffuser. The first reticle is observed by refraction and have a reflective coating of 50%. The assembly of a thin plate like economy beam splitter 50/50 assembled with the reticle is an economic solution to observe this object (Thorlabs, EBS1). This allows to see laser refraction on the first reticle with the first camera. The second reticle is directly observed making focus on the second reticle with the second camera. Figure 11.5 shows the laser beam path and its relation with the setup.

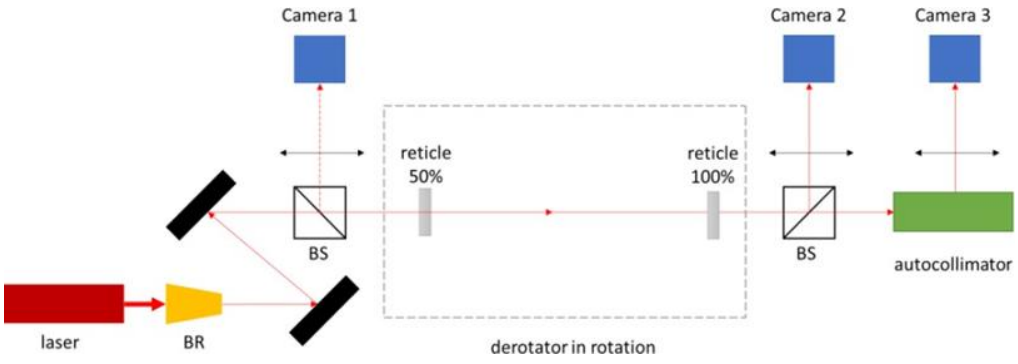

Figure 11.5: Sketch of the optical alignment system

Placing a reticle on the housing in rotation will make it rotate. If the reticle is not aligned with the axis of rotation, it is also translate describing a circle as shown in the Figure 11.6.

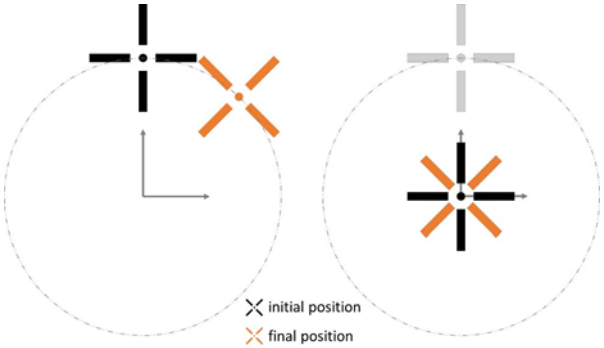

a) b)

Figure 11.6: a) Missaligned reticle and b) aligned reticle

Placing a reticle (R1DS2P, Thorlabs) on an XY translating mount (CXY1, Thorlabs; actuated by two 3/16-100" adjuster) will allow to place the reticle on the mechanical axis and define it at one point along this axis. Placing a second reticle with same method allows to define the axis. Mount are actuated by screw with 100 thread per inch and move of 254 µm per turn. This mount allows a reasonable precision of 10µm (more than 10^0). Figure 11.7 shows the two reticles and their adapter.

a) b)

Figure 11.7: a) Reticles and b) XY translating mount

Distance between the two reticles is 670mm and reticle lines are 10µm wide. The expected precision of this reference can be calculated as the following;

$$\alpha = atan\frac{2xh}{d} = 26.85\ \mu rad \qquad (11.1)$$

Figure 11.8 shows the rectile, support and adapter positions.

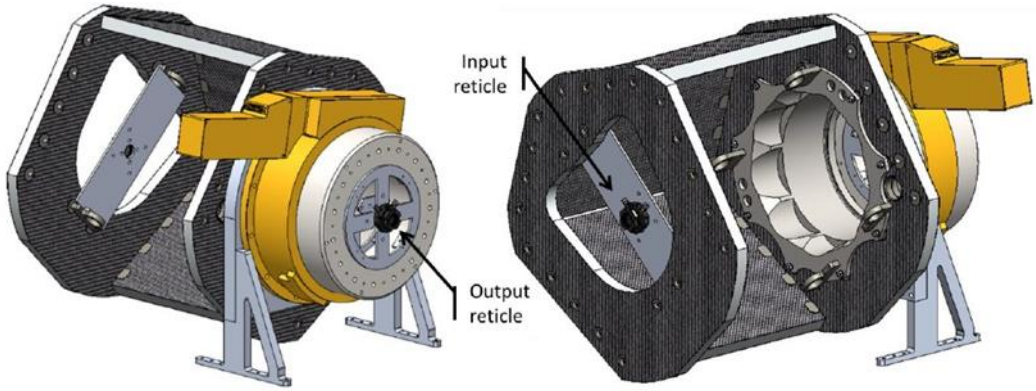

a) b)

Figure 11.8: a) Output rectile and b) input rectile

There is design proposal with Ximea camera MQ013RG-ON and convex lens. It has 1280x1020 pxl resolution nad pixel size is 5x5μm. Its rectile has 10 μm thickness and 10mm diameter.

Magnification is required for a good contract and resolution. So, M_1 should be equal or smaller then 0.5 for a rectile with fully imaged. For cross 4-pixel resolution, M_2 should be grater or equal to -4.

$$M = \frac{h_i}{h_0} = -\frac{d_i}{d_0} = \frac{f_0}{f_0 - d_0} \tag{11.2}$$

$$f_0 = -\frac{d_0}{1 - \frac{1}{M}} \tag{11.3}$$

Figure 11.9 shows the lens position and parameters for the calculations.

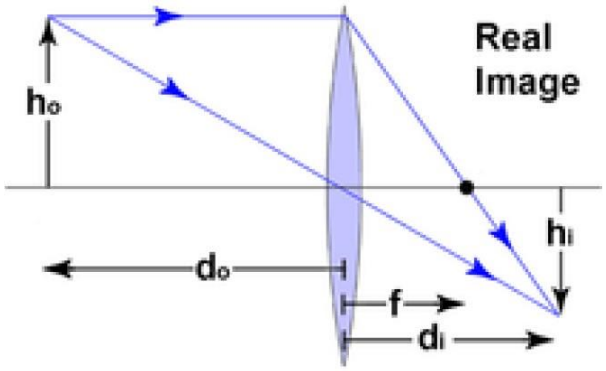

Figure 11.9: Sketch of thin lens image position and height

Considering the lens which is at distance -200mm from the input panel, $f_{i,1}$ becomes 66m and $f_{i,1}$ is 160mm. The distances are also calculated where $d_{i,1}$ is 100 mm and $d_{i,2}$ becomes 800 mm.

Improve precision of measure implies increase magnification. That can be done reducing object distance, but it increases image distance. Reduce image distance implies reduce focal length. In conclusion, the minimal focal length and object distance should be found during procedure as previous number are just an estimation taking care of optic table dimension.

A laser beam passing through the center of the two reticles create the reference of the mechanical axis. It is possible to align this laser with two gimbals mirror placed along the M3 side of the housing. Making focus of the camera on the reticles allow to see both target and laser beam. It is expected that the laser beam diameter is bigger than the target cross wide. To determine the center of the beam it is required to make an interpolation of the fundamental transverse Gaussian mode. Laser is coherent light and create wave interference. Measure can be improved using a moving diffuser that make light incoherent and digital image processing (FFT, blur effect, etc.). Figure 11.10 shows that this kind of treatment does not change the position measure by interpolation:

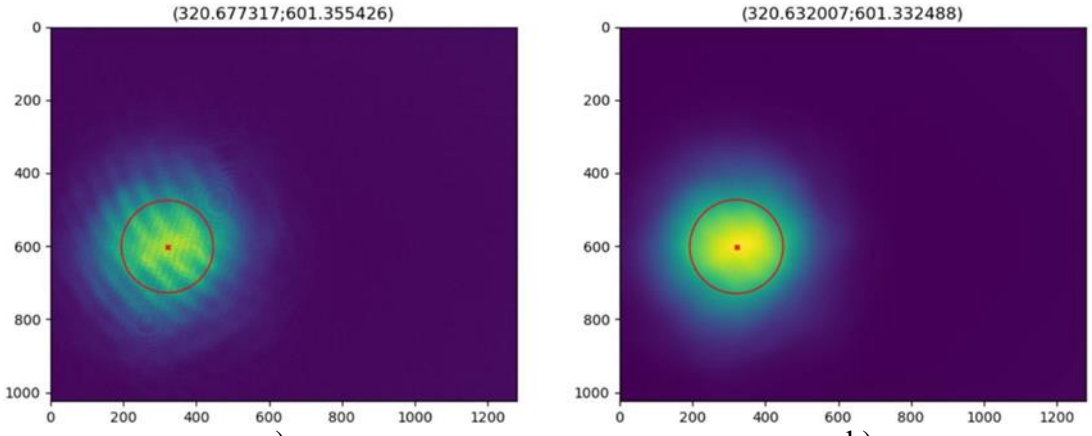

Figure 11.10: Laser footprint and centroid interpolation, a) without image processing b) with image processing

In this way, preliminary alignment is designed for adjusting the mechanichs and also the fine alignment is designed for catching the laser beam on the camera as it is described in this section.

11.2 Preliminary Alignment: Mechanical

11.2.1 M1-M3 structure preliminary alignment

The M1 and M3 mirror are assembled on an independent structure made of carbon fiber. Access to both mirror front side (surface) and back side (micrometer head) is required to do the preliminary alignment. Temporary support facilitate measure with the faro arm and allows access to both sides without moving the structure as shown in the Figure 11.11.

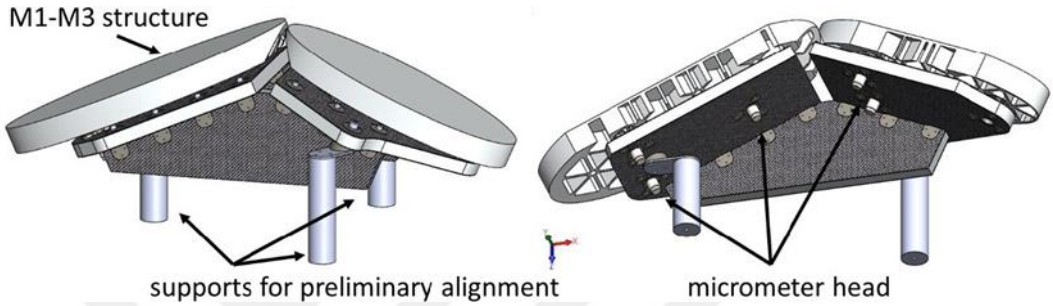

a) b)

Figure 11.11: a) Temporary supports b) micrometers

The angle of 132^0 between M1 and M3 is critical. Measure is realized comparing parallelism and distance between surface of the mirror and structure. Faro arm is used with touch detection probe to minimize impact of contact on the mirror surfaces. Measure is performed 10 mm from the edge of M1 and M3 mirror as shown in the Figure 11.12.

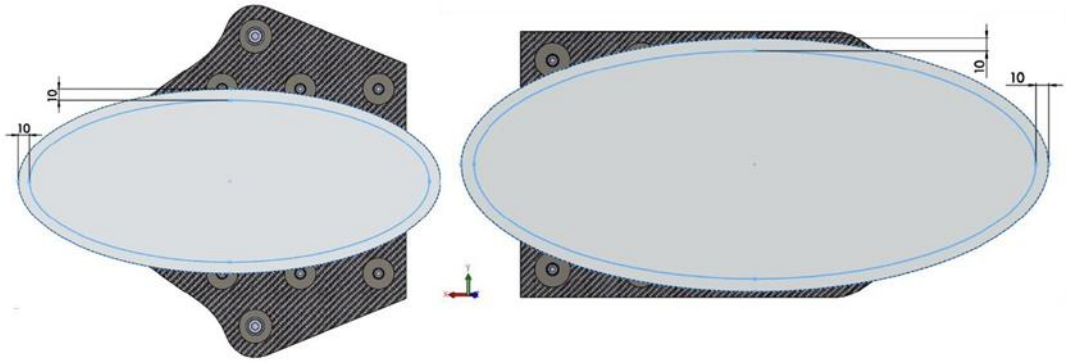

a) b)

Figure 11.12: 10mm measurable area on mirrors a) M3 and b) M1

This surface is additional in terms of optics beam reflection and not use in theory. This edge is required only in case of misalignment and then can be used as surface reference contact. Since probe diameter is less than 10 mm, it defines by itself during utilization the surface that can be touched.

The surface of insert shown below is made of Invar, coated with black chromium. Since they are assembled by gluing on the panels, they are used only as a pre-alignment. Accessible surface with faro arm has a flatness precision of 0.4 mm. The two triangular panels of the structure are machined after gluing to be assembled with an angle of $132^0 \pm 10^0$.

Power inspect software allows to measure parallelism and localization among others. Parallelism between inserts and corresponding mirror is measured with faro arm and adjusted with micrometer screw. As it is not possible to distinguish between tip or tilt misalignment, measure is made step by step using only one micrometer screw. Then localization is performed comparing distance between mirror and corresponding adapter plane. This measure is done moving each micrometer of the same quantity to preserve parallelism. Figure 11.13 shows one of the critical assemblies which must be assembled properly.

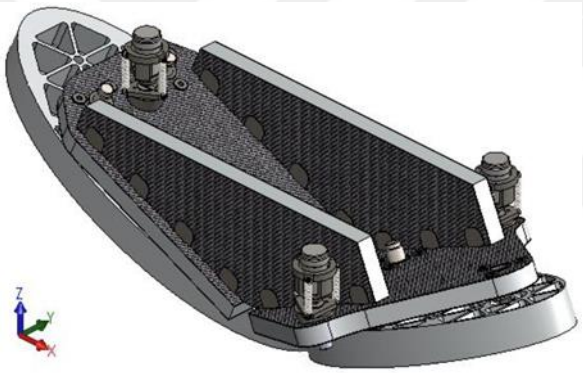

Figure 11.13: M1-M3 support with micrometer head and adapter

To make planes coincident it is required to compare parallelism then localization, in this order. It is required to repeat this operation several times to increase precision.

Tip-tilt alignment between mirrors is more important than their position at this step of the alignment. Following figure show that M1-M3 structure gets its own 3 micrometer screws that will catch up the position along the Z axis and the tip-tilt angle along the X and Y axis of both mirrors. As the beam diverges, misalignment in position along Y-axis and X-axis is catch-up by the 10 mm edge of mirrors, more it is ineffective on the misalignment of the beam.

To improve tip-tilt alignment between M1 and M3 it is required to compare measure with CAD models. Measuring a large amount of point on one mirror will allow to get high resolution on the measured surface and set it as reference to the CAD models.

Doing the same on the other mirror will allow to compare angle between measured surface and CAD model surface. Figure 11.14 shows the light beam passing through inside of the derotator.

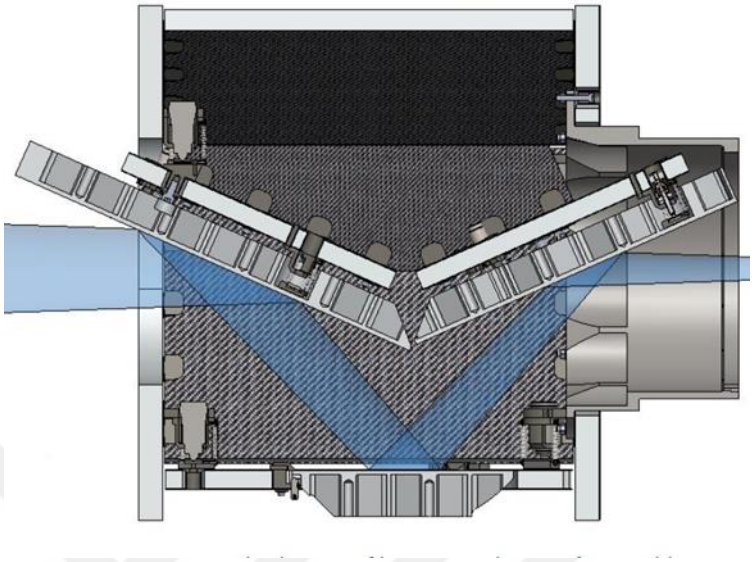

Figure 11.14: M1-M3 support with micrometer head and adapter

It is expected to get 6 µm repeatability with the current Faro Edge. That mean, repeatability of 0.1 µrad with 3 points of measure as the minimal diameter of the ellipse is 165 mm.

11.2.2 Complete preliminary alignment

Preliminary alignment is completed comparing the whole housing CAD model to the assembly. In a first time, M1-M3 structure is assembled and measured, then the same is done for the M2 mirror.

M1-M3 structure is assembled into the housing removing the input panel as shown in the figure below. This procedure required two to three people: one is holding M1-M3 structure and the other(s) one(s) screw adapters on the housing. It is important not to remove the output panel screwed on the hollow-shaft. As it is assembled into the motor, it defines the mechanical axis reference. Indicator or marking gauge placed on the side of a large panel measure the flexure due to weight of M1-M3 structure or mis-assembly.

Reference surface of the housing is described in Figure 11.15. Since the hollow shaft is manufactured by turning machines and assembled into the motor it is used as

mechanical reference with plane surface perpendicular to the optical axis, hole through the plane surface and inner cylindrical surface.

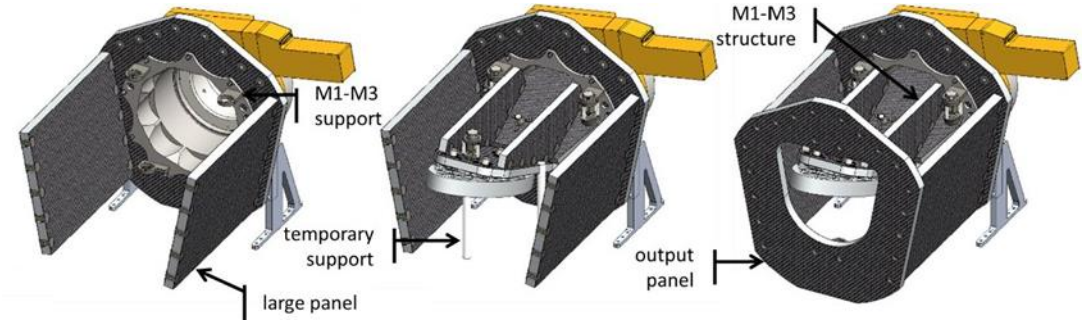

a) b) c)

Figure 11.15: a) Step1 initial housing assembly b) Step2 M1-M3 assembly c) Step3 front panel assembly

Accessing to hollow shaft reference surfaces with the faro arm it is required to temporary remove a large panel. All other accessible surface can be measured to improve fit between CAD model and assembly.

To adjust M1 and M3 mirror position little panel need to be temporarily removed where Figure 11.16 shows the structure. It is recommended removing them one by one to minimize stress and deformations to the housing.

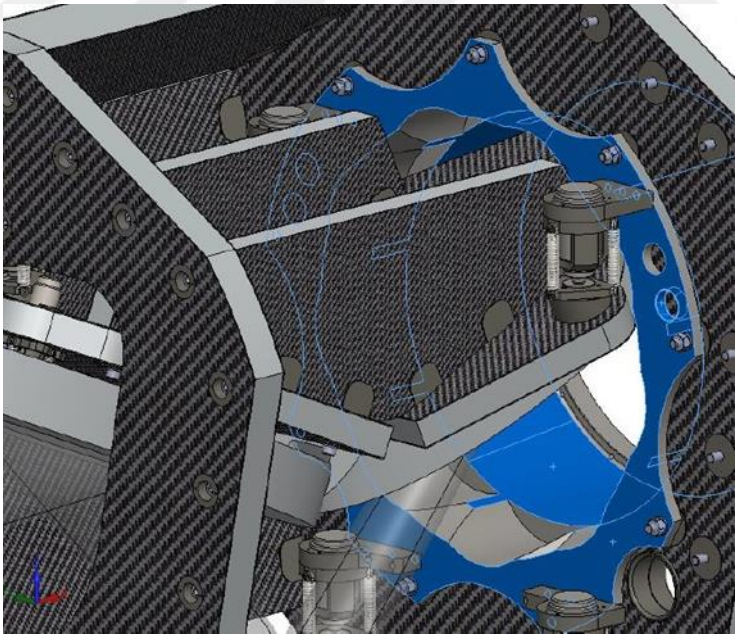

Figure 11.16: Hollow shaft reference surface in blue for planning reference

Parallelism and localization of M3 surface is compared with the CAD model. The micrometric screw of the M1-M3 structure is used since M3 mirror gets hard accessibility to DM22 micrometer head. If required M3 micrometer head still can be

used. Then, M1 surface is aligned with the CAD model thanks to its own micrometer head to not misaligned M3.

M2 mirror panel is attached to the housing by 3 screws. The back surface of M2 is previously measured and created into the CAD model. The alignment of M2 is done measuring the back surface as reference. Glue 3 reference spheres are incompatible with clutter inside the telescope flange and will create surface deformation. Measuring back surface thanks to reference surface should provide good repeatability even if the two plans are not parallel with reference surface marked.

11.3 Final Alignment: Optical

Mechanical axis is measured beforehand, without the M1-M3 structure into the housing and without moving the motor. The position has been measured by camera and angle by autocollimator. Goal is to reproduce the same alignment with the mirror inside the housing. It is recommended using M2 and M3 mirrors like gimbals to align the localization of the optical axis with the mechanical axis references.

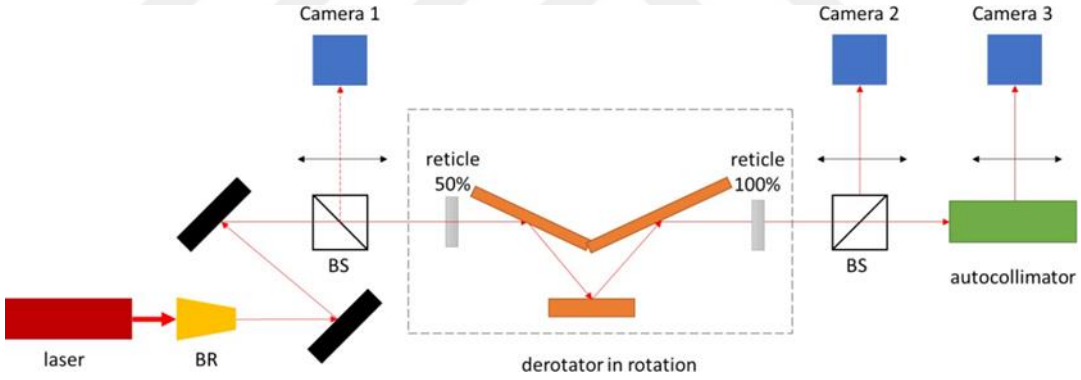

Figure 11.17: Sketch of the optical alignment system with K-mirrors

Optical axis position is performed with M2 and measured with CCD cameras. PSF of the laser is interpolated to improve precision of alignment and compared with the mechanical axis position measured in pixels.

Optical axis angle is performed with M3 and measured with autocollimator. Note that it will be impossible to correct the misalignment of mechanical axes references with mirrors. It is therefore important to align this reference as well as possible to make it precise.

12. CONTROL SYSTEM DESIGN

This section is dedicated to propose a derotator control system. First are stated informations that are required to compute the derotation speed.

- Telescope location latitude (constant)
- Earth (sideral) rotational speed (constant)
- Telescope elevation angle
- Telescope azimuth angle

It is also possible to replace the elevation and azimuth angles with the declination and time angle for computing the field of view rotational speed.

Then, we state informations that the TCS needs to properly control the derotator.

- Derotator absolute angular position
- Derotator maximal angular acceleration
- Motor maximal speed ($16^0/s$)
- Motor mechanical limits ($\pm 170^0$)

Technically, the derotator can cover an optical continuous derotation of $\pm 340^0$ thanks to the ratio of 2 between the object and the image. But basically, process should bring back the derotator to 0^0 when slewing and then start again the derotation for observation. Using this solution, the derotator will never reach the mechanical limit.

12.1 Controller

It is specified in the documents of the telescope system; the telescope is controlled by an industrial Beckhoff PC via Ethercat buses.

During the development of the derotator control system it was important to take into account wiring and control system. Therefore, it is logical to install the servomotor terminal directly in the cabinet which is on the Nasmyth platform which is on the

derotator side. However, the cable management and cabinets selection are not done yet. The Nasmyth platform has ongoing process for the placement of the optical devices and the surroundings. Figure 12.1 shows the specific locations on the telescope for such devices.

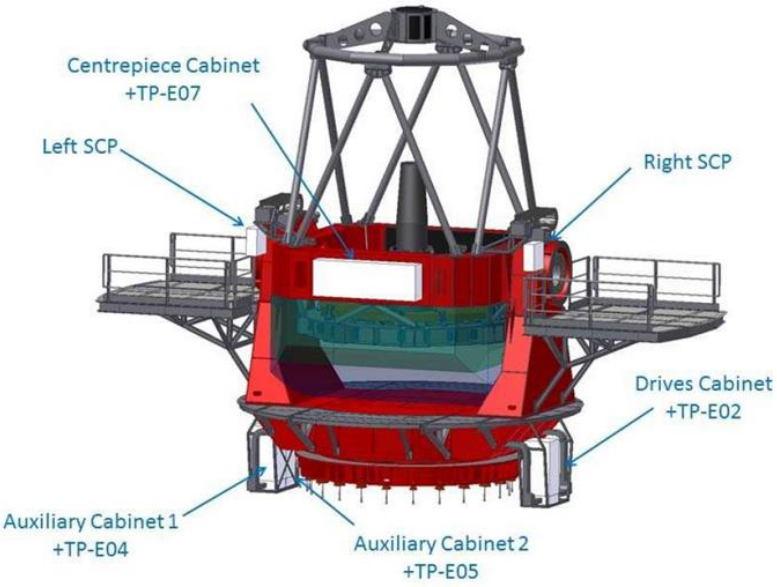

Figure 12.1: Cabinets location

The control system and the its cabinet will be placed underneath of the nasmyth platforms.

12.2 Power Interface

The derotator control electronics is dispatched in one cabinet, which will be located next to the derotator on the Nasmyth platform. A 1.6-meter-tall 19” aircooled cabinet is installed on the side of the derotator. The cabinet is composed with the chassis, with the Newport driver and the power supplies. Figure 12.2 shows the cabinet.

Figure 12.2: Novastar-cooled cabinet

The heat exchanger 19-inch 4HE integrated in the base of the cabinet has 3 fans pushing the air. Two thermostats will be installed to regulate the cabinet temperature. A 19-inch 1HE is used for the thermal control of the cabinet. It is connected to the heat exchanger in the bottom of the cabinet. This ESO control unit has power consumption of 6W.

Motor RV 350 HAHLT from Newport is a rotational stage used to rotate the housing containing mirrors. This motor is powered by a driver from XPS series. The main cable requires 100-240 VAC; 60/50 Hz; 10-6.9 A; 750W. The controller should be connected to a power installation that incorporates appropriate protection devices. To get an appropriate interface during observation an ethernet RJ45 connection to transmit OPC communication is required. To perform maintenance another power supply should be available to use a laptop directly near to the driver with the housing.

12.3 System Architecture

Figure 12.3 represents the system of the DAG that is in contact with derotator control system (DCS). The telescope supervisor (TSV) send information such as position of the celestial object to the DCS to control position and speed of the rotational stage.

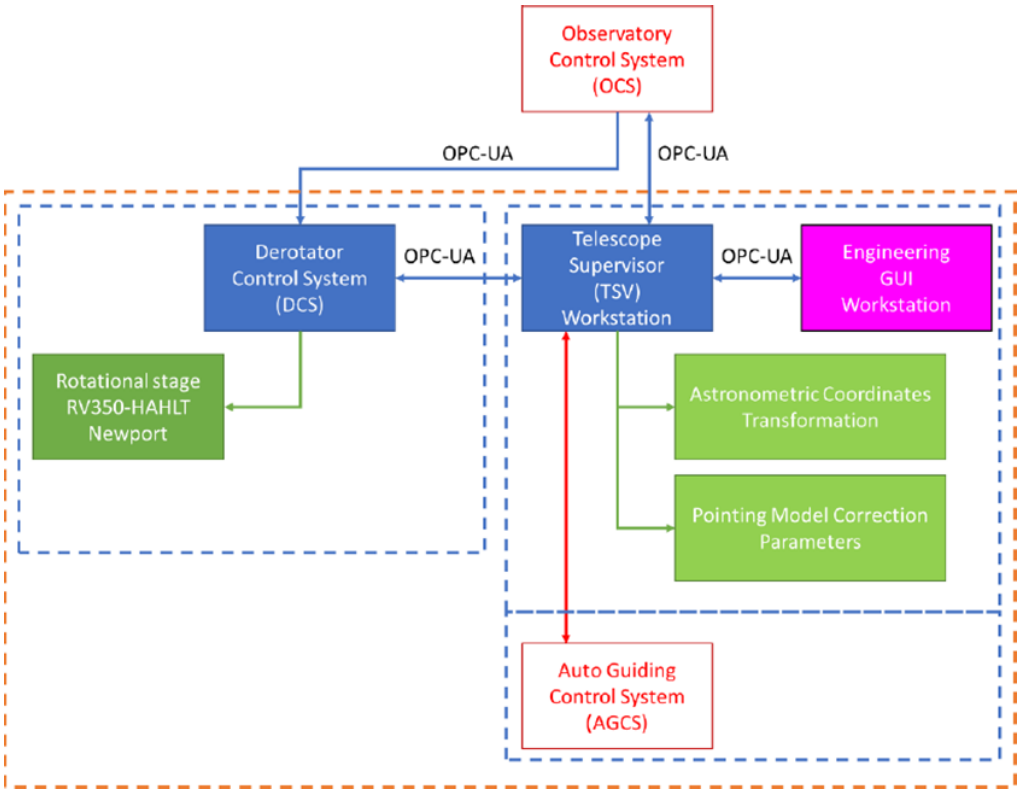

Figure 12.3: System diagram

12.4 System Function

Figure 12.4 shows the sub function of the derotator system using FAST method.

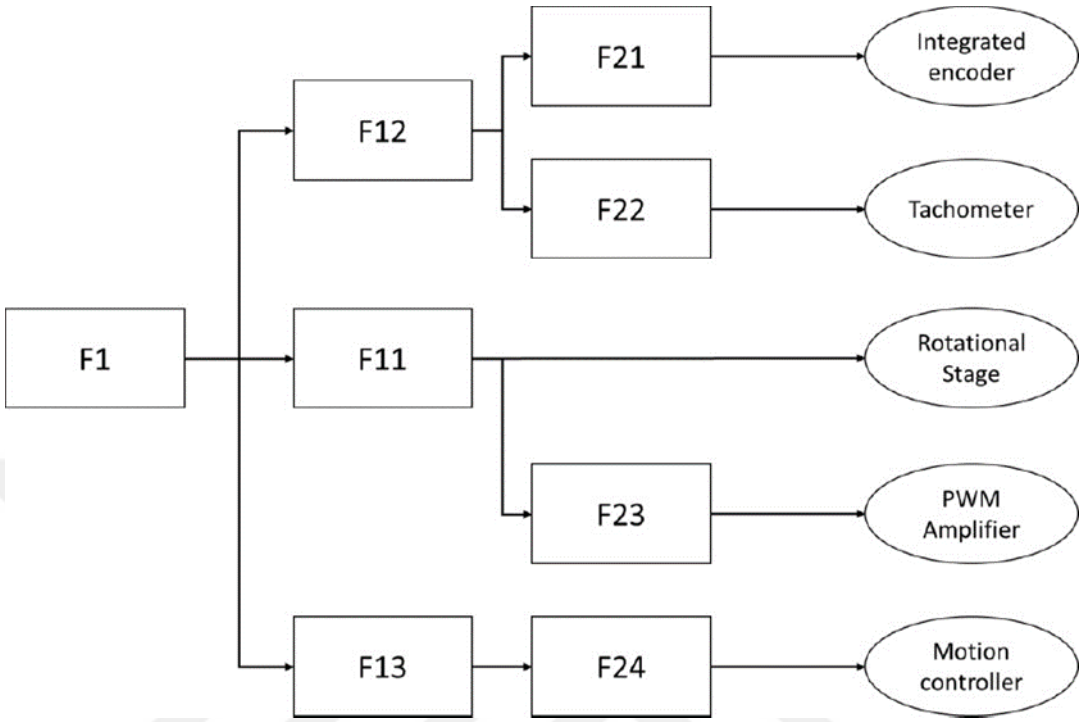

Figure 12.4: Functional analysis of the derotator

12.5 Fault Tree Analysis

Figure 12.5 shows a fault tree analysis for a corrupted image produced by KORAY system.

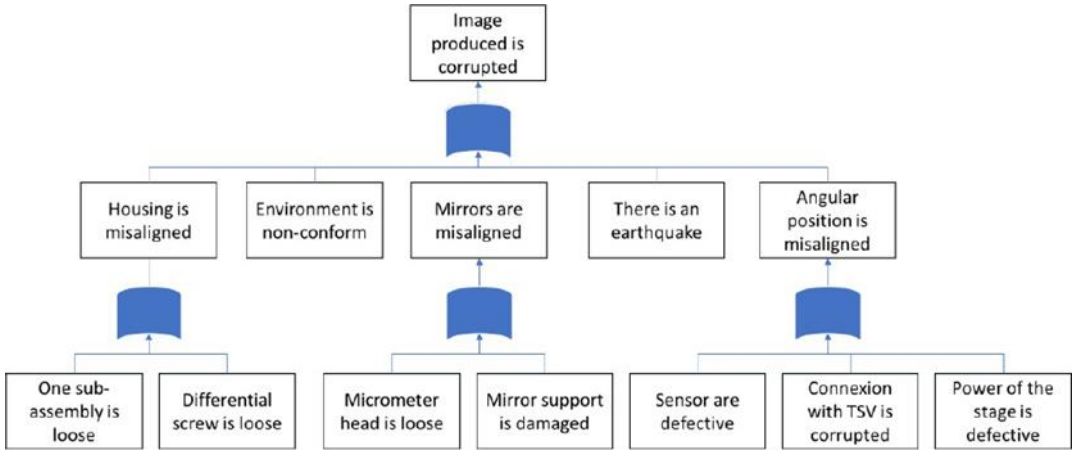

Figure 12.5: Functional analysis of the derotator

12.6 Labview Integration

The motor is controlled by the motion controller XPS-D2 that integrates XPS-DRV03 PWM drive module. It is a fully integrated solution that allows to quickly use the motor in control position. It allows to tune the controller but also create data acquisition. XPS controller comes with .NET drivers that allow to have a programming infrastructure for Microsoft building and then create desktop applications. There are several possibilities to use the API from VisualStudio, Matlab, Labview, Python...

Labview is chosen for programming. The developed programs allow to move the rotational stage with desired velocity to a desired position. Currently the velocity or position information are defined by the user. This mode on interface will be used for maintenance purpose or it will serve be used by authorized stuff only.

In daily routine, the derotator will communicate with the Telescope Control System and that upper controller send commands to derotator. Operator will not manually control the derotator. The speed information will be feed in hard real time via Ethercad port from telescopes plc to XPS motion controller. Since the Telescope Control System is not released yet, such adaptation couldn’t take place.

The basis of the controller is designed. It can execute commands for positioning with desired speed and acceleration. The only thing will be change about the controller is velocity data will be sent by telescope plc instead of defining manually.

12.7 Performance Tests

This section aims to show performance of the controller under different conditions. The tests are done in 2 different weather conditions and 2 different loading cases.

12.7.1 Loaded case

This subsection includes tests while the housing and counterweight are attached to the rotational stage. Figure 12.6 shows the test setup.

Figure 12.6: Loaded case

12.7.1.1 Tests at 13^0C

At this temperature, 3 main tests are performed.

Full range rotation test

On this test, starting point is -170^0 and rotation ends on $+170^0$ which means full rotation range of the rotational stage is used. Figure 12.7 shows the fix speed test which has 10^0/s speed and 32^0/sec^2 acceleration.

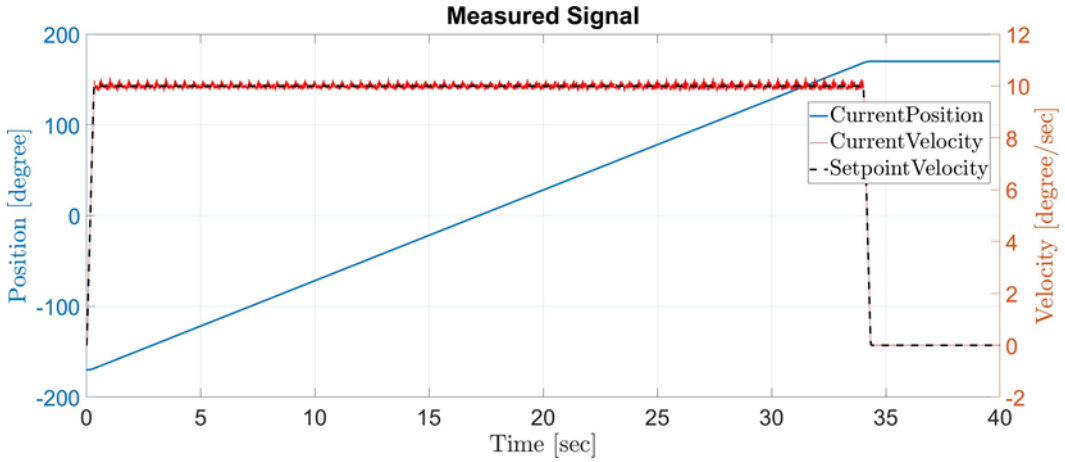

Figure 12.7: Speed of 10^0/s for loaded case

Figure 12.8 shows the fix speed test which has 0.4^0/s speed and $0.1^0/s^2$ acceleration.

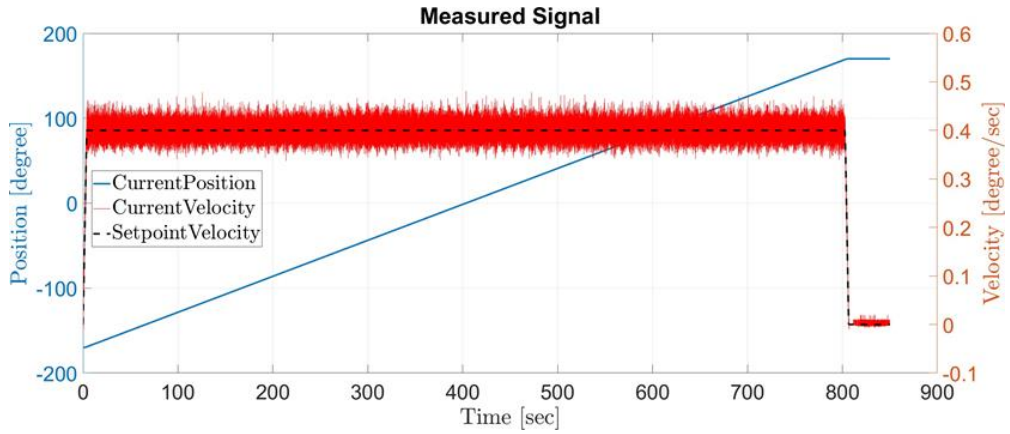

Figure 12.8: Speed of 0.4^0/s for loaded case

Different acceleration for fixed speed

The following 3 figures show 0.1^0/s fix speed and different acceleration tests. Figure 12.9 shows $10^0/s^2$ acceleration test.

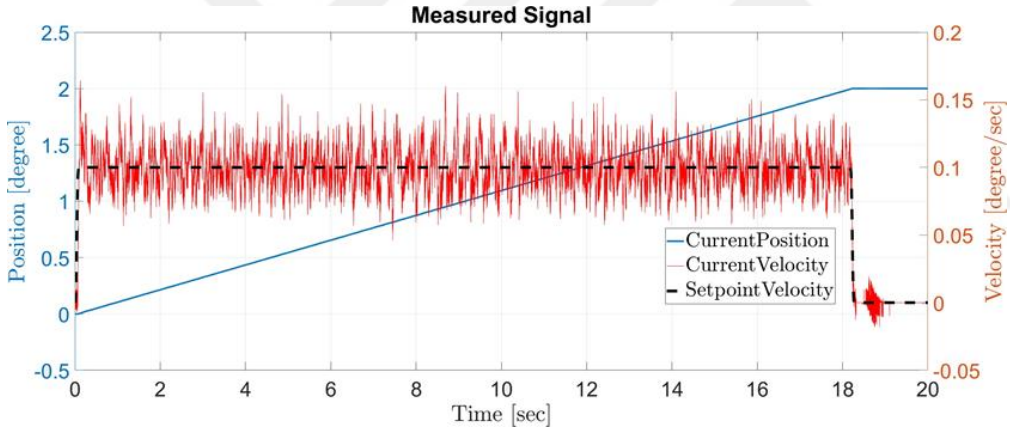

Figure 12.9: $10^0/s^2$ for Loaded case

Figure 12.10 shows $1^0/s^2$ acceleration test.

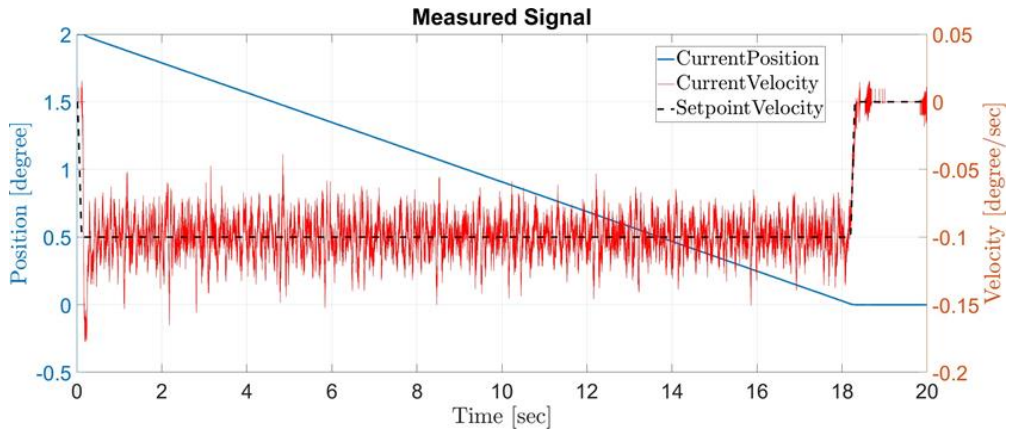

Figure 12.10: $1^0/s^2$ for Loaded case

Figure 12.11 shows $0.1^0/s^2$ acceleration test.

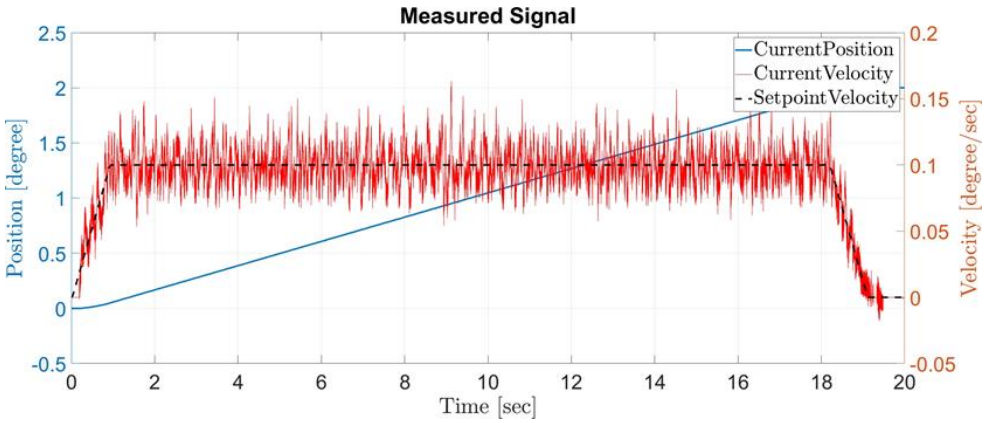

Figure 12.11: $0.01^0/s^2$ for Loaded case

Very slow speed tests

Lastly very slow speed tests are done for 2 different speeds. Figure 12.12 shows $0.01^0/s$ speed test.

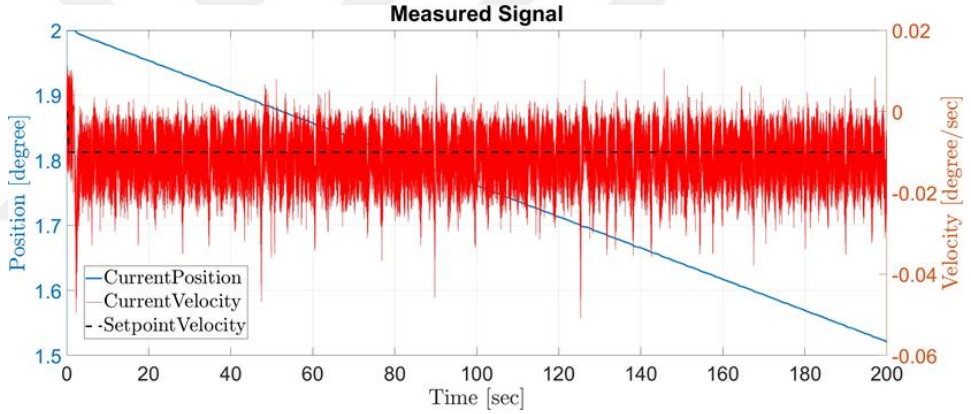

Figure 12.12: $0.01^0/s$ for loaded case

Figure 12.13 shows $0.0002^0/s$ speed test.

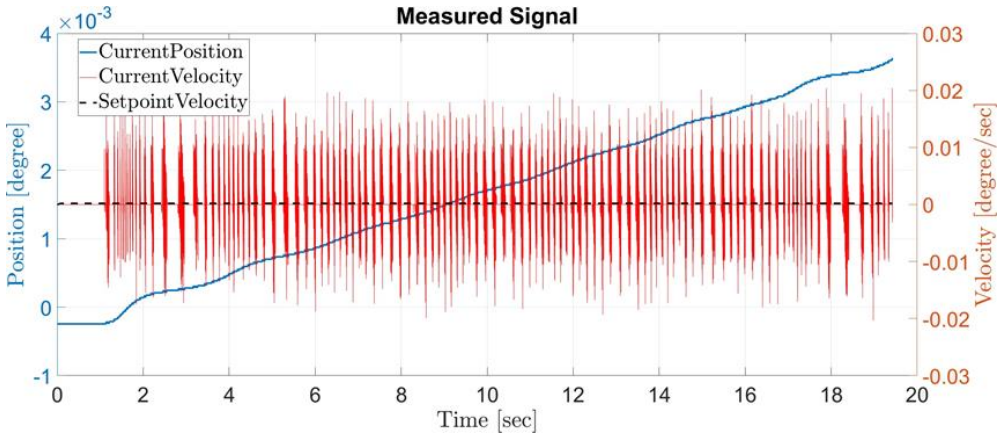

Figure 12.13: $0.0002^0/s$ for loaded case

12.7.1.2 Tests at 26^0C

Full range rotation test

Figure 12.14 shows the fix speed test which has 10^0/s speed and 32^0/sec^2 acceleration.

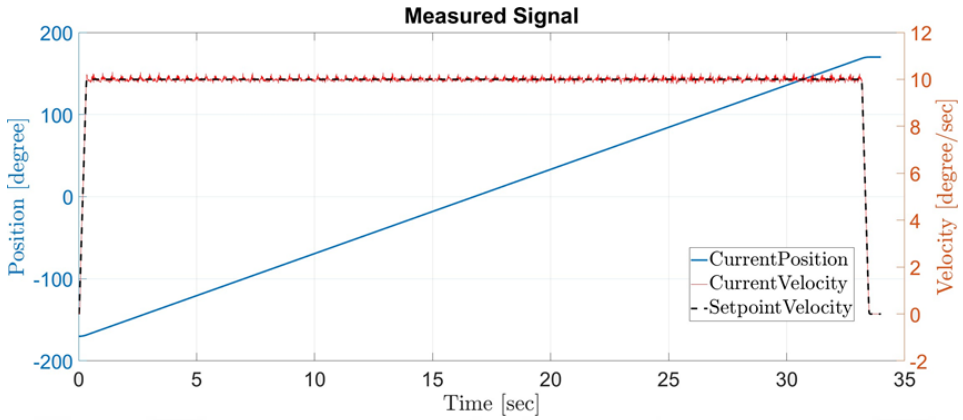

Figure 12.14: Speed of 10^0/s for loaded case at 26^0C

Figure 12.15 shows the fix speed test which has 0.4^0/s speed and 0.1^0/s^2 acceleration.

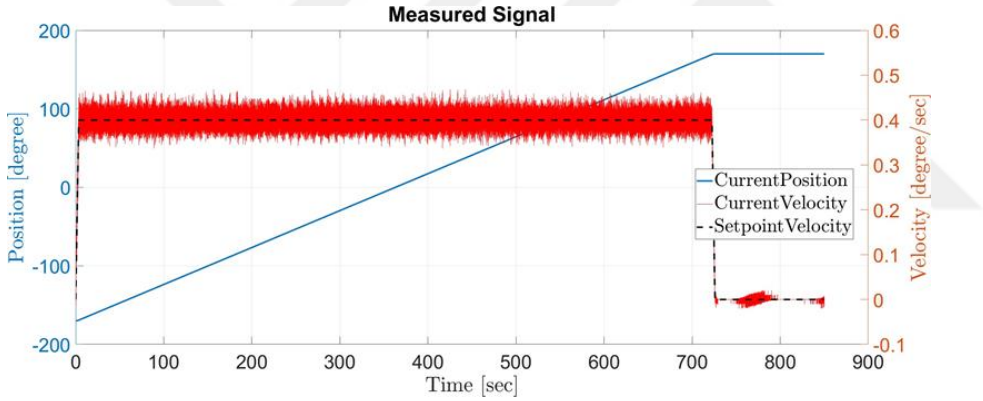

Figure 12.15: Speed of 0.4^0/s for loaded case at 26^0C

Different acceleration for fixed speed

0.1^0/s fix speed and different acceleration are tested. Figure 12.16 10^0/s^2 acceleration;

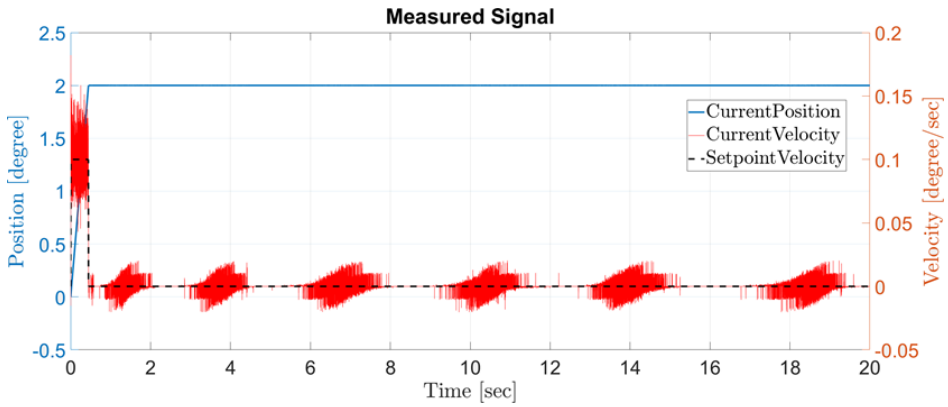

Figure 12.16: 10^0/s^2 for loaded case at 26^0C

Figure 12.17 shows $1^0/s^2$ acceleration test.

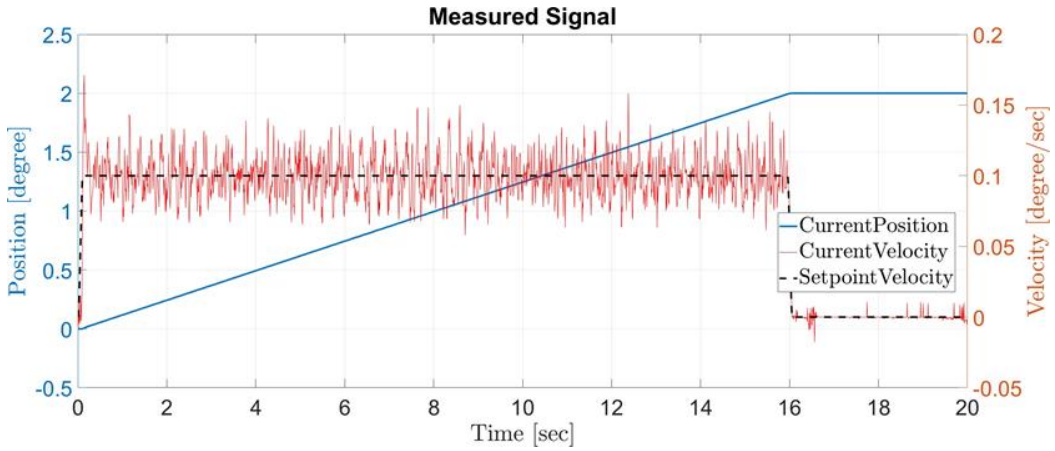

Figure 12.17: $1^0/s^2$ for loaded case at 26^0C

Figure 12.18 shows $0.1^0/s^2$ acceleration test.

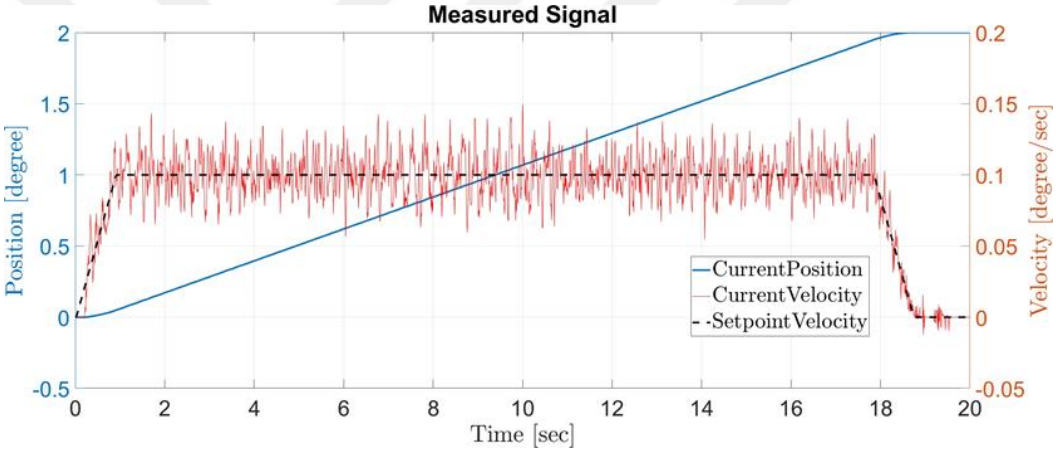

Figure 12.18: $0.1^0/s^2$ for loaded case at 26^0C

Very low speed tests

Ttests are done for 2 different speeds. Figure 12.19 shows $0.01^0/s$ speed test.

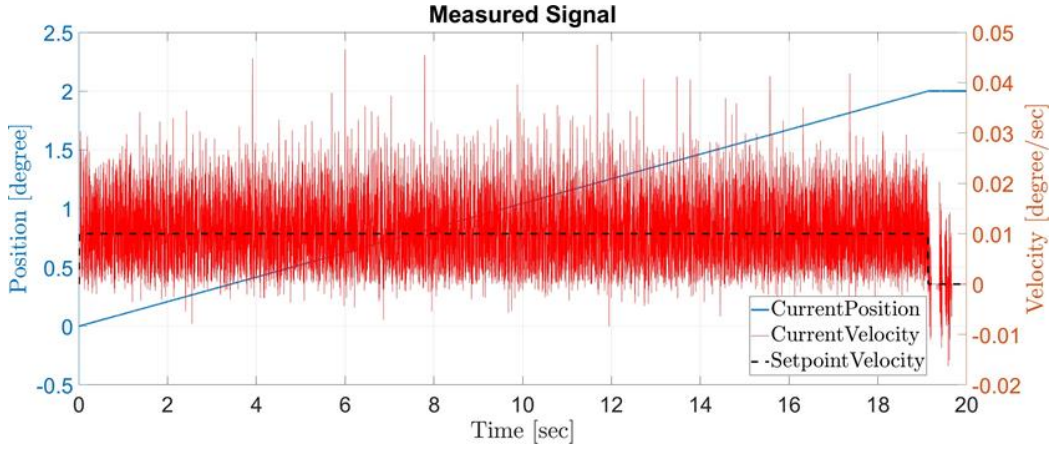

Figure 12.19: 0.01^0/sec for loaded case at 26^0C

Figure 12.20 shows 0.0002^0/s speed test.

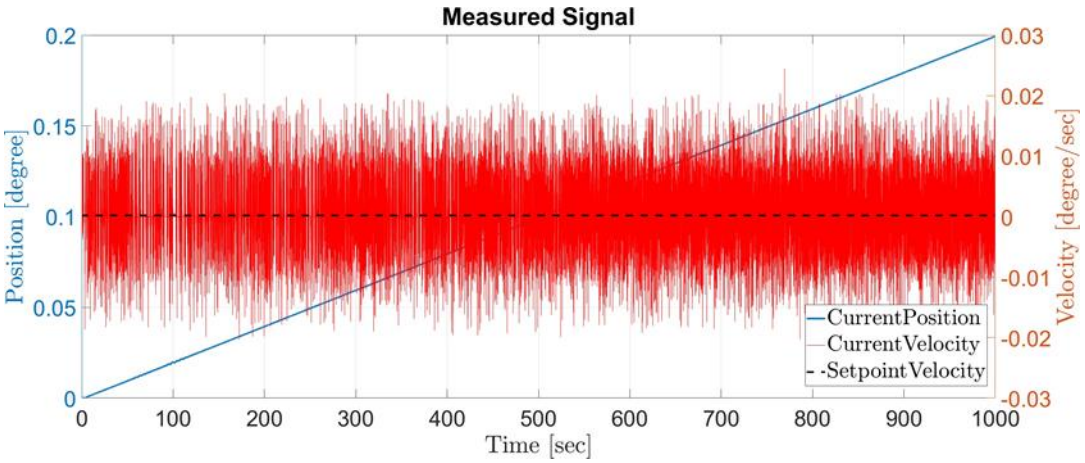

Figure 12.20: 0.0002^0/sec for loaded case at 26^0C

12.7.2 Not loaded case

This subsection includes tests while the housing and counterweight are not attached to the rotational stage. Figure 12.21 shows the test setup.

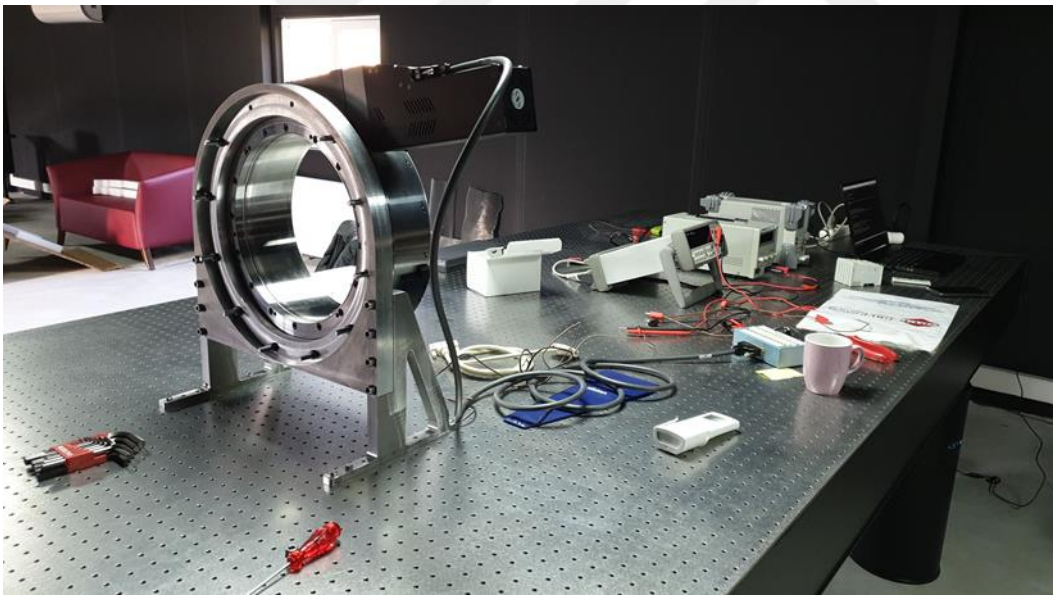

Figure 12.12: Not loaded case

12.7.2.1 Tests at 26^0C

Not loaded case is only performed for 26^0C. The point is comparing the outputs for different loading scenarios. The temperature difference comparison is done for loaded case, because it is simulating the real-life case.

Full range rotation test

Figure 12.22 shows the fix speed test which has 10^0/s speed and 32^0/sec^2 acceleration.

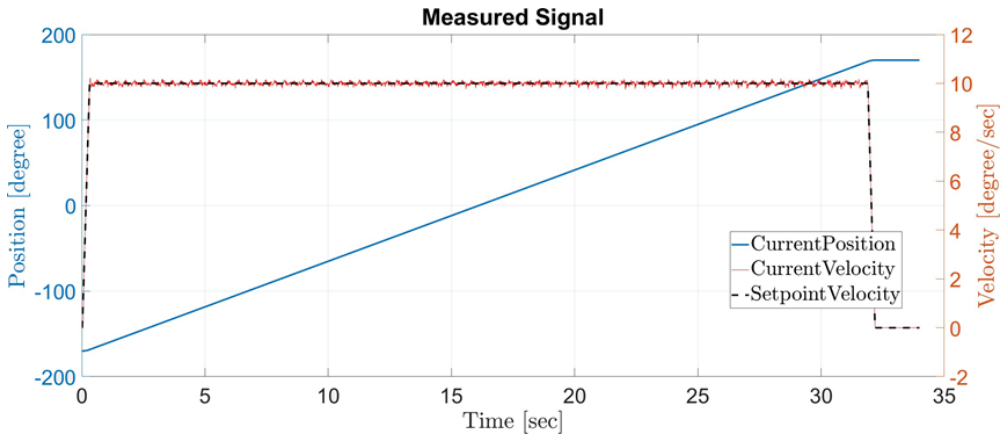

Figure 12.22: Speed of 10^0/s for loaded case at 26^0C

Figure 12.23 shows the fix speed test which has 0.4^0/s speed and 0.1^0/s^2 acceleration.

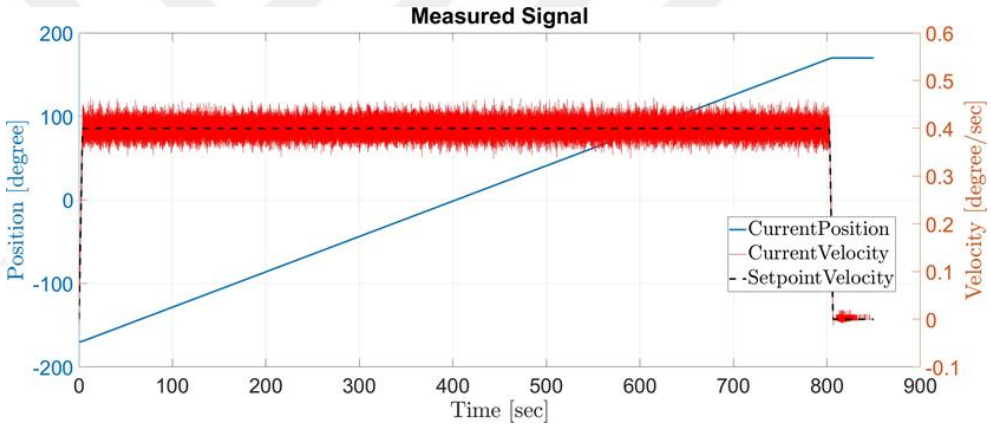

Figure 12.23: Speed of 0.4^0/s for loaded case at 26^0C

Different acceleration for fix speed

0.1^0/s fix speed and different acceleration are tested. Figure 12.24 10^0/s^2 acceleration;

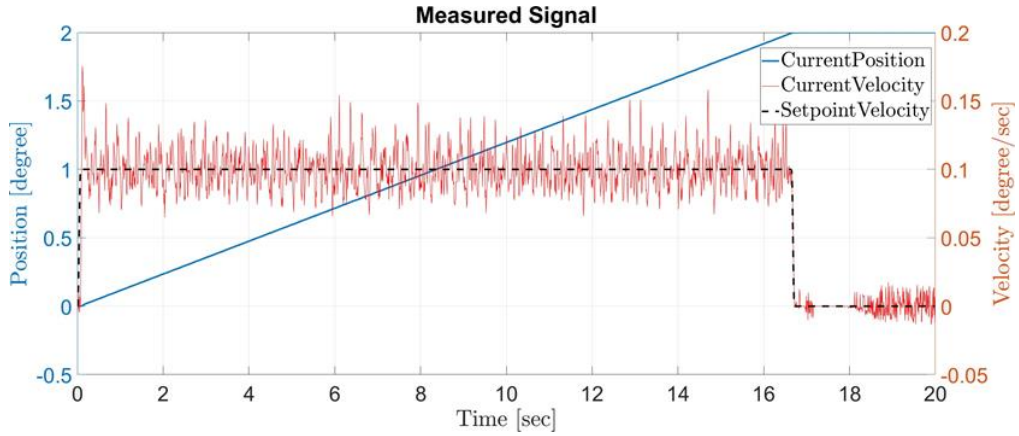

Figure 12.24: 10^0/s^2 for loaded case at 26^0C

Figure 12.25 shows $1^0/s^2$ acceleration test.

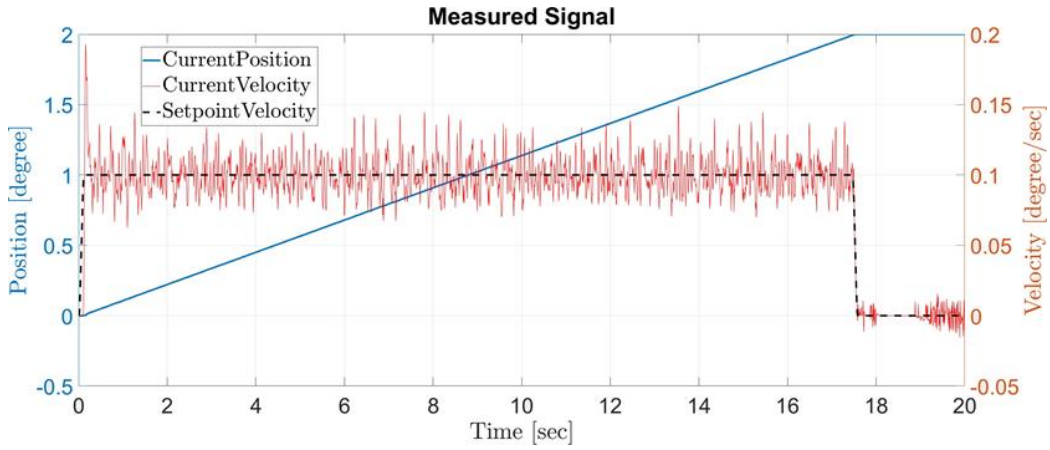

Figure 12.25: $1^0/s^2$ for loaded case at 26^0C

Figure 12.26 shows $0.1^0/s^2$ acceleration test.

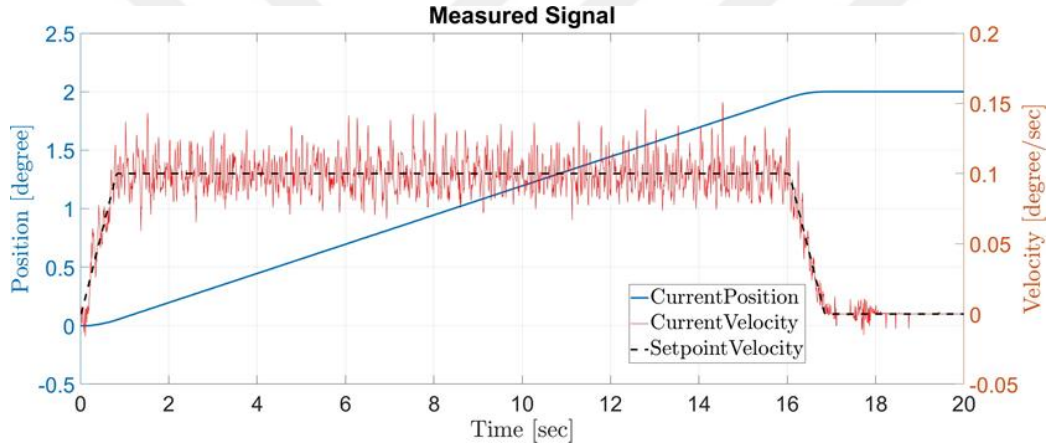

Figure 12.26: $0.1^0/s^2$ for loaded case at 26^0C

Very low speed tests

Ttests are done for 2 different speeds. Figure 12.27 shows $0.01^0/s$ speed test.

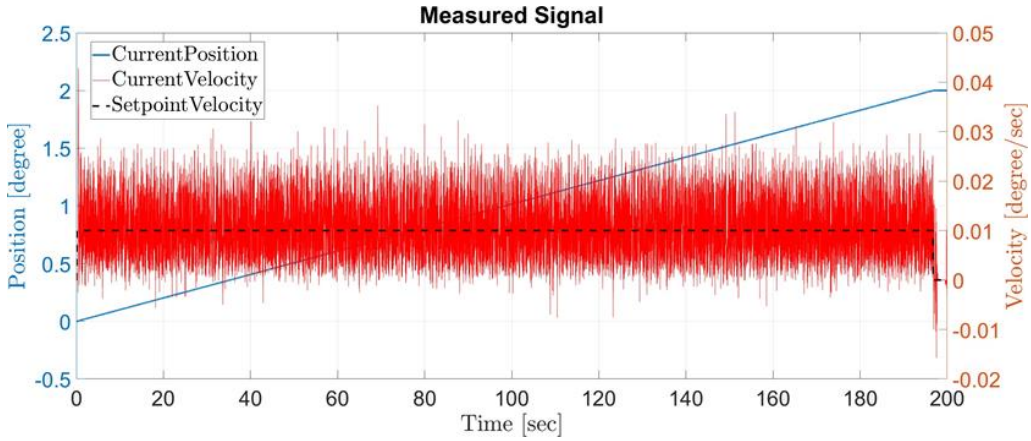

Figure 12.27: 0.01^0/sec for loaded case at 26^0C

Figure 12.28 shows 0.0002^0/s speed test.

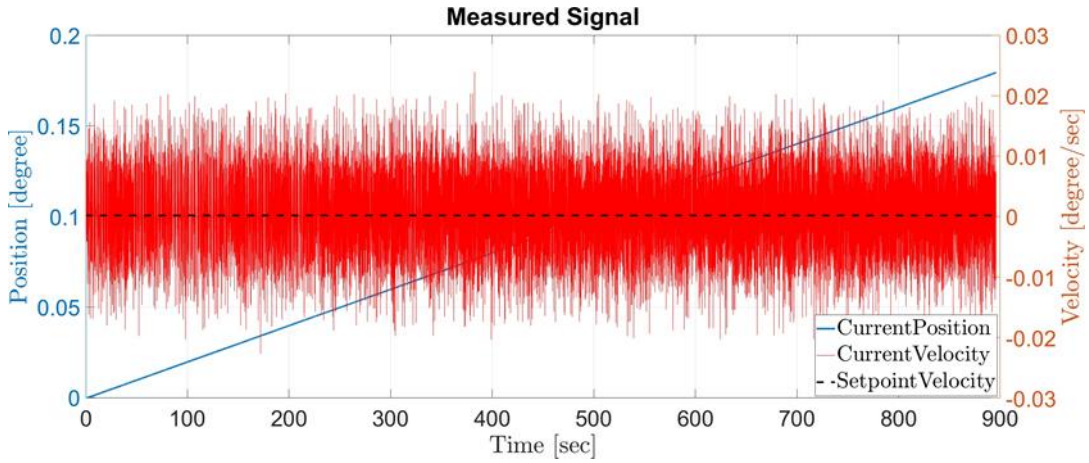

Figure 12.28: 0.0002^0/sec for loaded case at 26^0C

12.8 Comments on The Controller

The controller is tested under two different temperature conditions and two different loading conditions. 7 different tests are performed on combination of these conditions. The behavior of the system is identified on low and high-speed operations.

The position information is plotted on every curve. It actually describes the success of the controller. A smooth positioning curve is a must for such optomechanical device because of the long exposure. Different acceleration values slightly change the positioning accuracy. The maximal speed for derotator is calculated as 1.1^0/s. In this way, acceleration value is optimized. It is understood that $1.1^0/s^2$ acceleration value is allowable.

The tests show that the positioning accuracy is insensitive to weight and temperature changes. If it is intended to use for another optic systems where long exposure is not the case, it can operate on much higher speed.

13. CONCLUSION

In this thesis, an optomechanical device is designed and analyzed, manufactured, a controller is developed and tested in laboratory. This device will be used as a subsystem for 4m DAG Telescope. There are some technical specifications which are expected to met. These real-life challenges are exceeded with unique solutions.

The device has cantilever design and will be placed in the central hole of the telescope fork. The unique mechanical design has been completed and applied for two patents through European Patent Office and World Intellectual Property Organization. The cantilever design obligates to have very rigid body. It is provided by light weighted design and choosing relevant materials.

Due to the weather conditions of the telescope location, the derotator will be exposed to high humidity and it will be operational between ±15◦C. The material couples are matched considering such thermal conditions. FEM analysis is done for validation of mechanical relevance with the specifications. The developed internal stresses and flexures are in the margin of error.

The design aims to maximize the field of view for the allowable space of the derotator. Considering mechanical errors, an optomechanical design is done and mirror dimensions are set. The unique alignment mechanism is developed for reducing the mechanical errors.

The setting flange has ability of translating on x and y axis. It is connected to the support flange with ball joints which provides moving ability on rx and ry axis. In order to make fine alignment as much as possible, mirror mechanisms are connected to housing by semi kinematic joints. The mirrors can make tip and tilt turns by turning micrometers located in the joints. Considering the abilities of the derotator, an alignment procedure is developed. The procedure is confirmed in the lab by setting advised optical setup and running the derotators motor.

In order to control the motor, a control interface is developed. The user can place the derotator to the homing position or on a desired angle with desired speed. Lab

experiments are done to confirm that the controller is meet with the desired specifications. In order to provide a seamless observation, the Logic operations are defined.

13.1 Future Developments

Since the telescope control system is not shared yet, the logic operations couldnt applied to the derotator software. After the release, a communication protocol should be developed between telescope control system and derotator control system. The speed information must be feed in hard real time to the derotator controller. The infrastructure of the hard real time data transfer is done. However, it should be tested in real life situations when the telescope receives it’s first light on the last quarter of 2021.

REFERENCES

[1] **Howard S., Leon V., and David L.** (1955). Method of Measuring the Contrast Rendition of Optical Systems for Line Targets of Various Angular Subtenses, *J. Opt. Soc. Am. 45*, 886-890.

[2] **Lauroesch, T. J.** (1957). U.S. Patent No. US2873381A. Washington, DC: U.S. Patent and Trademark Office.

[3] **Stetson, K.A.** (1978). The use of an image derotator in hologram interferometry and speckle photography of rotating objects, *Experimental Mechanics 18*, 67–73. doi:BF02324502.

[4] **D. S.L.** (1974). A Compact Derotator Design, *Opt. Eng. 13* 130119. doi:12.7971671.

[5] **Sebastian B., Alexander D., Lars H. and Arne K.** (2006). Optical derotator for scanning vibrometer measurements on rotating objects, Proc. SPIE 6345, Seventh International Conference on Vibration Measurements by Laser Techniques: Advances and Applications 63450M. doi:12.693066.

[6] **Santiago B., Jörg-Uwe P., Ralf-Rainer R. and Friedrich M.** (2016). Design of a large image derotator for the E-ELT instrument MICADO, Proc. SPIE 9908, Ground-based and Airborne Instrumentation for Astronomy VI 99089H. doi:12.2231632.

[7] **Ünal A. C., Sarajlic M., Jolissaint L. and Keskin O.** (2018). In flange derotator design for the 4m DAG Telescope, Proc. SPIE 10700, Ground-based and Airborne Telescopes VII, 107003W. doi:12.2313912.

[8] **Keskin O.** (2011). *Point spread function reconstruction for next generation adaptive optics systems* (PhD thesis). University of Victoria, Victoria CANADA.

[9] **Brunelli A., Bergomi M., Dima M., Farinato J.** (2012) Tips and tricks for aligning an image derotator, Proc. SPIE 8446, Ground-based and Airborne Instrumentation for Astronomy IV 84464L. doi:12.926884.

[10] **Mark de Koe**, (2013) *A design study of a cryogenic high accurate derotator* (MSc Thesis), TU Delft, Delft Netherlands.

[11] **Fernando G., Andres M., Christopher D. and Stephen R** (2012) Mechanical design of NESSI: New Mexico Tech Extrasolar Spectroscopic Survey Instrument, Proceedings of SPIE - The International Society for Optical Engineering 8446. doi:10.1117/12.926282.

[12] **Pierre Y.** (2003). *The Design and Construction of Large Optical Telescopes.* Springer.

[13] **Paul R.** (2006). *Opto-Mechanical Systems Design*, CRC Press, Taylor and Francis Group.

[14] **Herbert R., Pierre-Yves M. and Gilbert G.** (2017). *Réflexion. Réfraction. Diffraction*, Techniques de l'Ingénieur, traité d'électronique.

[15] **Url-1** <*http://www.linternaute.com/photonumerique/dossier/aberrations/2.shtml*>. date retrieved 19.02.2019.

[16] **Url-2** <*http://wikipedia.org/wiki/Seeing* >, date retrieved 05.02.2019.

[17] **Url-3** <*http:// www.globalsecurity.org/military/library/policy/army/fm/6-2/Ch7.htm*>. date retrieved 05.02.2019.

[18] **Baudet J.** (2015). *Dérotateur de champ pours le télescope DAG, étude de faisabilité* (MSc Thesis), University of Applied Science Western Switzerland, HEIG-VD SWITZERLAND.

[19] **Schwertz, K. M., & Burge**, (2012) *Field guide to optomechanical design and analysis*, Publications SPIE.

[3] **Url-4** <*http://www.newport.com/p/RV350HAHLT*>, date retrieved 14.01.2017.

APPENDICES

APPENDIX A: Rotational speed computation
APPENDIX B: Motor datasheet

APPENDIX A

```
% Calculation of the derotation speed
clc;close all, clear all;
altDeg = [0:5:90];
azDeg = [-180:0.1:180];
altRad = deg2rad(altDeg);
azRad = deg2rad(azDeg);
latDeg = 0;
latRad = 0.6943;%deg2rad(latDeg);

omega_T_rad_h = 0.262
omega_T_rad_s = omega_T_rad_h/3600; %  [rad/s]

for i=1:length(altRad)
   for j=1:length(azRad)
       omega_DTR_rad(i,j) = -omega_T_rad_s*cos(latRad)...
       *(cos(azRad(j))/cos(altRad(i)));
       omega_DTR_deg(i,j) = rad2deg(omega_DTR_rad(i,j));
   end
end

xmin = 0;
xmax = 360;
ymin = 0;
ymax = 90;
zmin = -.1;
zmax = .1;

figure
mesh(azDeg, altDeg, omega_DTR_deg, 'LineStyle', 'none');
%title('Field rotation speed');
%colormap(hsv)
%colormap spring
%alpha(.3)
axis([xmin, xmax, ymin, ymax, zmin, zmax]);
%axis tight
%shading('interp');
colormap colorcube
xlabel('Azimuth [deg]');
ylabel('Altitude [deg]');
zlabel('Rotation speed [deg/s]');

figure;
omega_DTR2_deg = -omega_DTR_deg/2;

mesh(azDeg, altDeg, omega_DTR2_deg, 'EdgeColor', 'none'...
    , 'LineStyle', 'none');
title('Derotator rotation speed');
%colormap(hsv)
%colormap spring
%alpha(.3)
axis([xmin, xmax, ymin, ymax, zmin, zmax]);
%axis tight
%shading('interp');
colormap colorcube
xlabel('Azimuth [deg]');
ylabel('Altitude [deg]');
zlabel('Rotation speed [deg/s]');
```

APPENDIX B

For Motion, Think Newport™

RV Series

HIGH-PERFORMANCE PRECISION ROTATION STAGES

- Precision 80–350 mm diameter rotation stages
- Monolithic design ensures high structural stiffness
- Ideal for high-load application
- High-accuracy versions with direct reading encoder and better than 0.0001° (0.36 arcsec) resolution

Newport
Experience | Solutions

The RV Series rotation stages provide high-precision angular positioning accuracy combined with high load capacity. There are five stage sizes and six drive configurations available, optimizing load capacity, torque, speed and resolution for a variety of operating conditions.

All RV stages are constructed of tool steel, with rotation accuracy ensured by ground bearing surfaces. A double row of preloaded bearings allows for high off-center loads in a reduced footprint. The single monolithic design offers improved stiffness without compromising dynamic performance. The largest RV stage can bear up to 6500 N or rotate up to 80 °/s, while maintaining less than 4 µm eccentricity.

Precise rotation is ensured by a precision ground and hardened worm gear. A rotary encoder mounted on the worm gear shaft provides 0.001° position feedback resolution (0.00025° resolution with RVS80CC) on the standard configurations. For more demanding applications, the HAT and HAHLT options are available on the RV120 to RV350 models. These stages are equipped with a direct reading optical encoder attached to the moving platen for superior resolution and accuracy.

The selection of the drive configuration should be based on the precision and speed requirements relative to the inertia of the payload.

Motor Drive Versions

Stepper motor-driven stages are available in full step PE and ministep PP versions. The mini-step drive version (PP) enables high angular speed motions up to 20 °/s. The larger models, RV120PP to RV350PP, feature a worm mounted rotary encoder for improved accuracy and repeatability. The encoder also provides a method for detecting motor stalling, an important feature for applications with high acceleration ramps and high torques or payload inertias.

The RVS80PP does not use an encoder. Instead, position is attained by the number of commanded steps and micro-steps. The high output torque of the stepper motor, combined with extensive performance tests, ensures position accuracy as long as the recommended load, torque and payload inertia are not exceeded. The RVS80PP provides very high motion sensitivity with good linearity between commanded micro-steps and the actual motion of the stage at a very reasonable price. The full-step PE version is equipped with a reduction gear providing higher torque. This version is only available on the models RV120 to RV350 and is recommended for high inertia payloads and vacuum applications.

DC motor-driven stages are available in high speed (CC and HAT) and high torque (CCHL and HAHLT) versions. The CC and HAT versions enable speeds up to 80 °/s. The HAT features a high-resolution direct reading encoder and tachometer for superior repeatability, position stability and speed regulation. The CCHL and HAHLT versions are equipped with a reduction gear providing higher torque and payload inertia capacity. The HAHLT features a high-resolution direct reading encoder and tachometer for superior repeatability, position stability and speed regulation.

RVS80CC

RV120HAT-F

RV160PP

RV240CCHL

RV350HAHLT

Design Details

Base Material	Stainless Steel				
Bearings	Double row ball bearings				
Drive Mechanism	Ground worm gear with self compensating preload				
Feedback	RVS80CC: Worm mounted rotary encoder, 8,000 pts/rev, Index pulse RVS80PP: None. One full-step equals 0.01° RV120 to RV350, except for HAT and HAHLT versions: Worm mounted rotary encoder, 4,000 pts/rev, Index pulse HAT and HAHLT versions: Direct reading optical encoder on the rotating platen, 20 mm signal period				
Limit Switches	Optical, at ±170, can be disabled for continuous rotation (except HAT & HAHLT versions)				
Origin	Optical				
Cable Length	3 m cable included				
Vacuum Compatibility	Vacuum compatible versions are available up to 10^{-6} hPa using full-step motor (PEV6)				
Weight [lb (kg)]	RVS80	RV120	RV160	RV240	RV350
	4.0 (1.8)	14.3 (6.5)	19.8 (9)	35.3 (16)	57.5 (27)
	–	RV120HAT	RV160HAT	RV240HAT	RV350HAT
		17.6 (8)	24.2 (11)	41.9 (19)	72.8 (33)

Specifications

Travel Range (°)	360 continuous	With disabled limits, except HAT & HAHLT
	±170	HAT & HAHLT versions
Minimum Incremental Motion (°)	0.001	Except RVS80PP, HAT & HAHLT versions
	0.0002	RVS80PP
	0.00075	HAT versions
	0.0002	HAHLT versions
Uni-directional Repeatability, Guaranteed[1] (°)	0.002	Except RVS80CC, HAT & HAHLT versions
	0.001	RVS80CC
	0.001	RVS80PP
	0.0002	HAT & HAHLT versions
Bi-directional Repeatability, Guaranteed[1] (°)	0.004 or ± 0.002	Except RVS80, HAT & HAHLT versions
	0.003 or ± 0.0015	RVS80CC
	0.003 or ± 0.0015	RVS80PP
	0.0012 or ± 0.0006	HAT & HAHLT versions
Absolute Accuracy, Guaranteed[1] (°)	0.01 ° or ± 0.005	Except RVS80, HAT & HAHLT versions
	0.015 or ± 0.0075	RVS80CC
	0.015 or ± 0.0075	RVS80PP
	0.005 ° or ± 0.0025	HAT & HAHLT versions
Maximum Speed (°/s)	80	CC & HAT motor option, except RVS80CC
	40	RVS80CC
	20	PP motor option
	16	CCHL & HAHLT motor option
	2	PE motor option
Wobble, Guaranteed[1][2] (µrad)	40 or ± 20	RVS80
	20 or ± 10	RV120 & RV160
	16 or ± 8	RV 240 & RV350
Eccentricity, Guaranteed[1] (µm)	4 or ±2	
MTBF (h)	20,000	

[1] Shown are peak to peak, guaranteed specifications or ± half the value as sometimes shown. The typical specifications are about 2X better than the guaranteed values.

[2] To obtain arcsec units, divide the µrad value by 4.8.

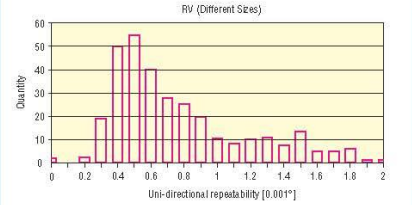

Uni-directional repeatability plot for RV Series stages. The typical (mean) uni-directional repeatability is 0.001°. The guaranteed value is 0.002°.

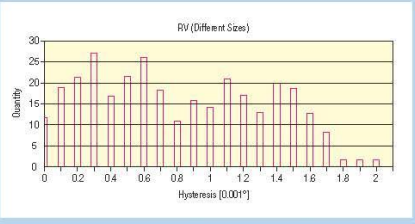

Reversal value (Hysterisis) plot for RV Series stages. The typical (mean) reversal value is 0.001°. The guaranteed value is 0.002°.

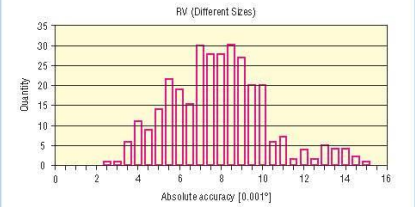

On-axis accuracy plot for RV Series stages. The typical (mean) on-axis accuracy is 0.001°. The guaranteed value is 0.002°.

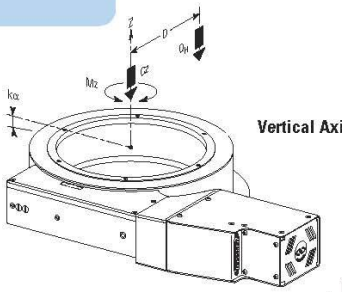

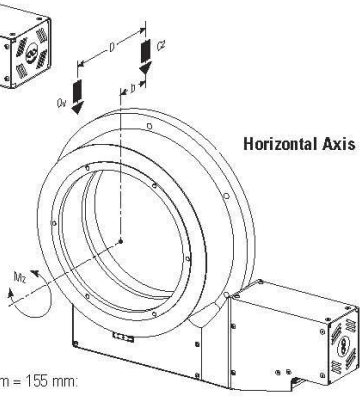

Load Characteristics

		RV80CC	RV120CC	RV160	RV240	RV350
Cz, Normal centered load capacity (N)		900	1800	2700	4000	6500
a, Construction parameter (mm)		30	40	50	70	100
b[1], (mm)	except HAT & HAHLT	39	53	57	59	73
	for HAT & HAHLT	71	75	77	91	
kα, Radial compliance (μrad/Nm)		3.5	1.5	0.6	0.3	0.1
Q_H, Off-center load, vertical rotation axis		$Q_H \leq Cz / (1 + D/a)$				
Q_V, Off-center load, horizontal rotation axis		$Q_V \leq Cz / 2 / (1 + D/a)$				

[1] *Construction parameter: Distance between the top surface of the RV stage and the bearing center.*

Example:
Q_V at a distance of 80 mm from the top surface for a RV160HAT rotation stage, D = 80 mm + 75 mm = 155 mm:

$$Q_V = 2700\ N / 2 / (1 + 155\ mm / 50\ mm) = 329\ N$$

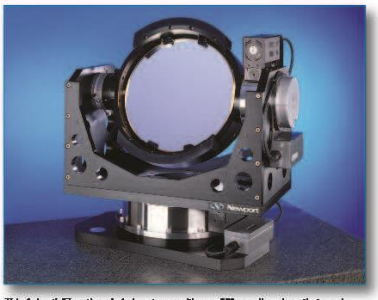

This Azimuth/Elevation gimbal system positions a 350 mm dia. mirror that can be *used for laser based qualification and characterization of precision optical sensors, LIDAR analysis, or target tracking.*

Torque and Payload Inertia

Model	Max. Torque Mz (N.m)	Max. Inertia Iz (kg.m²)	Max. Speed (°/s)
RVS80PP	2	0.5	20
RVS80CC	2	0.1	40
RV120PP	15	1	20
RV120PE	20	70	2
RV120CC	10	0.2	80
RV120CCHL	15	7	16
RV120HAT	4	0.9	80
RV120HAHLT	6	7	16
RV160PP	20	3	20
RV160PE	35	100	2
RV160CC	11	0.7	80
RV160CCHL	20	24	16
RV160HAT	6	1	80
RV160HAHLT	8	8	16
RV240PP	22	4	20
RV240PE	60	150	2
RV240CC	13	1.5	80
RV240CCHL	30	38	16
RV240HAT	7	1.1	80
RV240HAHLT	10	10	16
RV350PP	25	4	20
RV350PE	80	220	2
RV350CC	14	1.8	80
RV350CCHL	30	56	16
RV350HAT	7	1.2	80
RV350HAHLT	10	10	16

This table lists the maximum torque and the maximum payload inertia for all RV rotation stages. The maximum payload inertia equals the maximum kinetic energy that the rotation stage can absorb in the event of a sudden stop at the maximum speed. Likewise, this is the maximum inertia to accelerate from stop to the maximum stage speed in 250 ms. Some RV stages can handle higher payload inertias at reduced speed. For detailed information, please contact a Newport Applications Engineer.

Compatible Motion Controllers/Drivers

Family	Max. Power Consumption (W)	XPS [1] Driver Module	Compatibility ESP301 [1]	SMC100CC [1]	SMC100PP [1]
RV120CC to RV350CC	130	XPS-DRV03			
RV120CCHL	40	XPS-DRV03	✓		
RV160CCHL to RV350CCHL	130	XPS-DRV03			
RV120HAT to RV350HAT	170	XPS-DRV03			
RV120HAHLT to RV350HAHLT	170	XPS-DRV03			
RV120PE to RV350PE	60	XPS-DRV01	✓		
RV120PP to RV350PP	60	XPS-DRV01	✓		
RVS80CC	40	XPS-DRV01	✓	✓	
RVS80PP	20	XPS-DRV01	✓		✓ [2]

[1] *Enhanced System Performance (ESP) Controller.*

[2] *Compatible, but MIM is 1/20 th of a full step.*

Dimensions

RVS80 Models

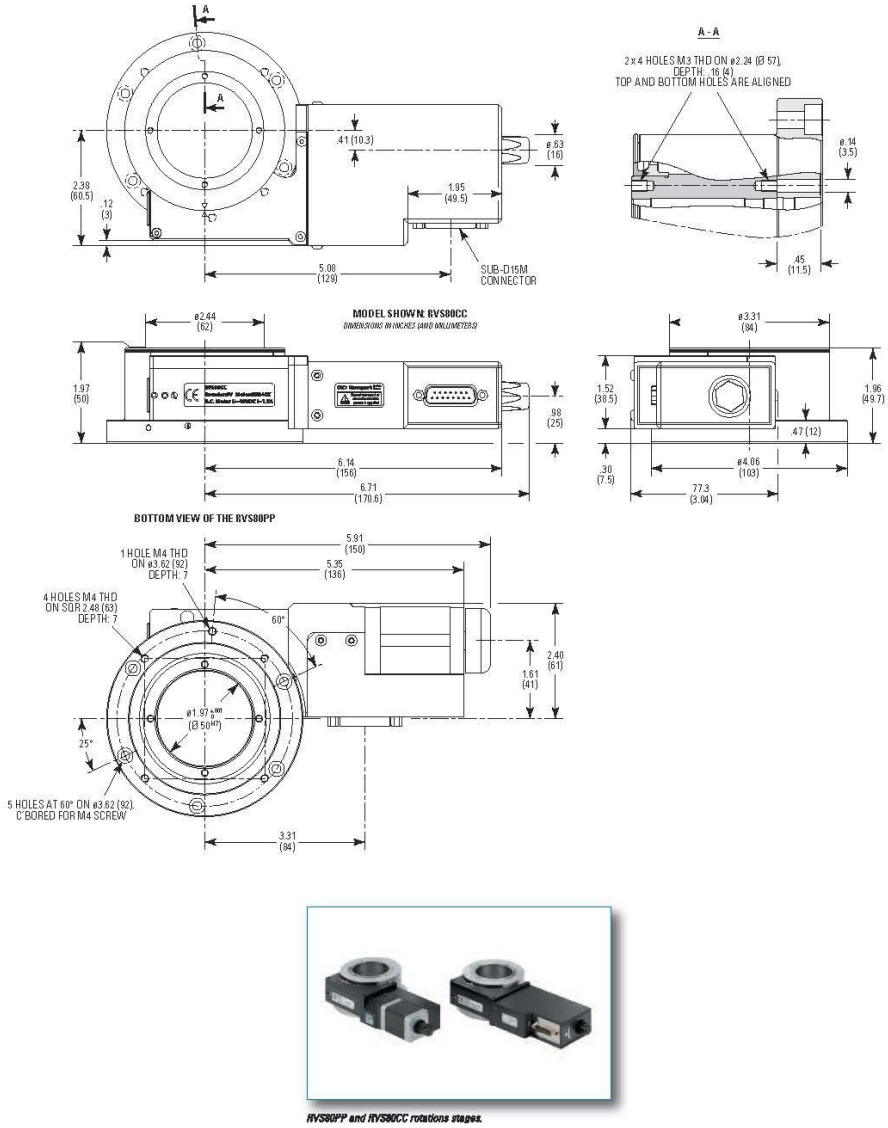

RVS80PP and RVS80CC rotations stages.

RV120 to RV350 Models

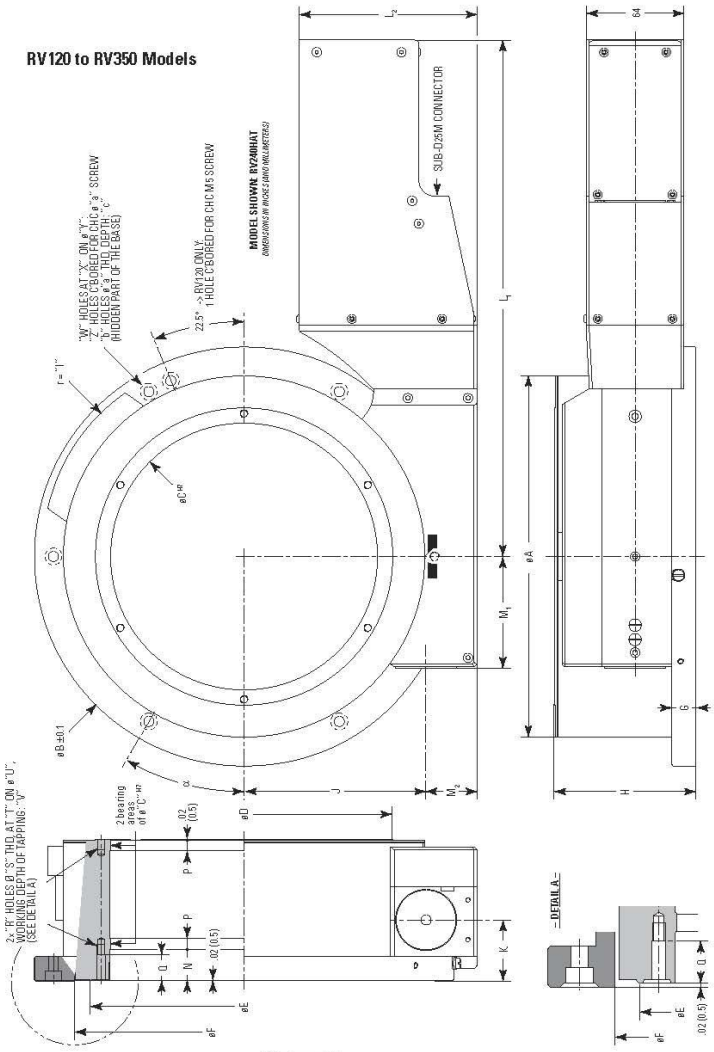

MODEL	A	B	C	D	E	F	G	H	I	J	K	N	P	Q
RV120	4.96 (126)	6.10 (155)	3.07 (78)	3.66 (93)	3.90 (99)	4.55 (115.5)	.55 (14)	3.39 (86)	3.15 (80)	2.49 (63)	1.34 (34)	.75 (19)	16 (4)	.59 (15)
RV160	6.42 (163)	7.56 (192)	4.33 (110)	5.165 (129)	5.28 (134)	5.98 (152)	.55 (14)	3.50 (89)	3.86 (98)	3.21 (81.5)	1.42 (36)	.73 (18.5)	20 (5)	.57 (14.5)
RV240	9.33 (237)	10.83 (275)	6.89 (175)	7.64 (194)	8.03 (204)	8.74 (222)	.63 (16)	3.66 (93)	5.22 (132.5)	4.70 (119.5)	1.58 (40)	.80 (20.3)	28 (7)	.65 (16.6)
RV350	14.02 (356)	15.55 (395)	11.02 (280)	11.88 (302)	12.40 (315)	13.06 (331.5)	.69 (17.5)	4.25 (108)	7.44 (189)	7.05 (179)	1.97 (50)	.84 (21.3)	31 (8)	.68 (17.3)

MODEL	R	S	T	U	V	W	X	Y	Z	a	b	c	α
RV120	4	M4	90°	3.44 (87.5)	24 (6)	6	60°	5.39 (137)	5	M5	1	7	17.5°
RV160	6	M5	60°	4.72 (120)	28 (7)	6	60°	6.85 (174)	5	M5	1	7	25°
RV240	6	M5	60°	7.38 (187.5)	28 (7)	6	60°	9.84 (250)	5	M6	1	10	30°
RV350	6	M6	60°	11.61 (295)	28 (7)	12	30°	14.65 (372)	10	M8	2	12	10°

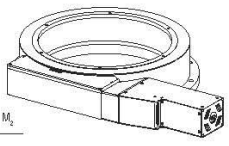

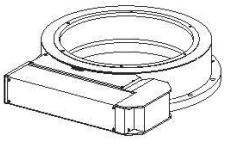

ROTATION STAGE, DIRECT MOTOR

MODEL	L_1 PP	PE	CC	CCHL	M_1	L_2	M_2
RV120	9.90 (251.5)	9.90 (251.5)	9.90 (251.5)	11.87 (301.5)	1.79 (45.5)		
RV160	10.39 (264)	12.36 (314)	10.39 (264)	12.36 (314)	2.13 (54)	4.61 (117)	1.32 (33.5)
RV240	11.38 (289)	13.35 (339)	11.38 (289)	13.35 (339)	2.89 (73.5)		
RV350	12.40 (315)	14.37 (365)	12.40 (315)	14.37 (365)	4.13 (105)		

ROTATION STAGE, FOLDED MOTOR

MODEL	L_1	M_1	L_2	M_2
RV120	6.12 (155.5)	2.15 (54.5)		
RV160	6.61 (168)	2.48 (63)	6.32 (160.5)	4.35 (110.5)
RV240	7.60 (193)	3.25 (82.5)		
RV350	8.62 (219)	4.49 (114)		

RVHA & RVHAT Models

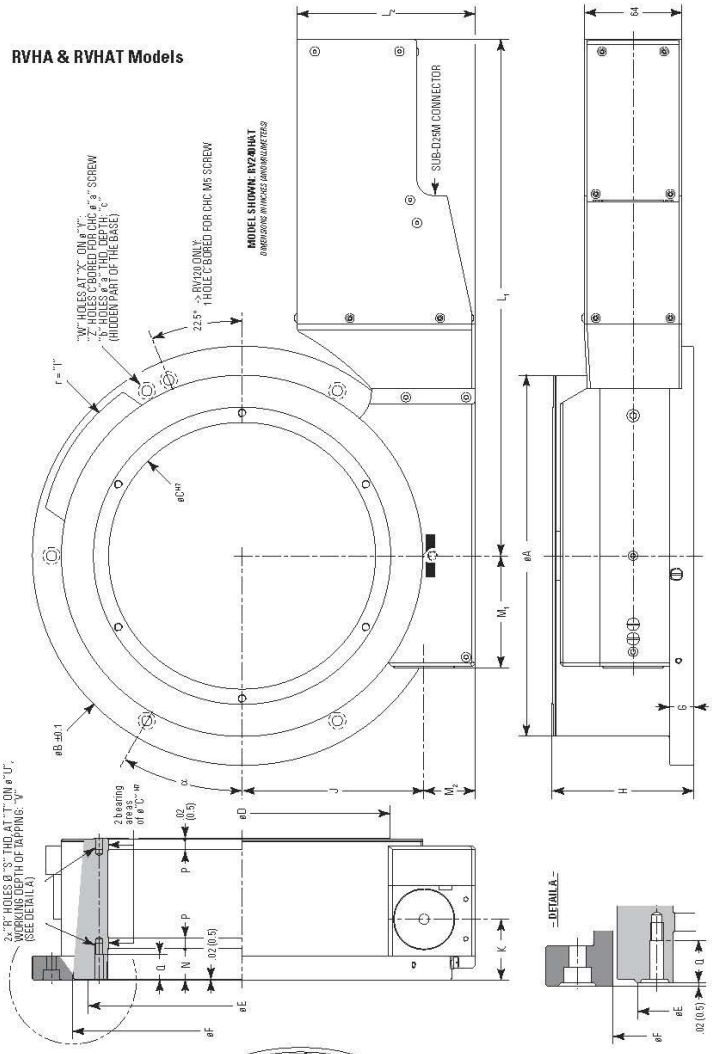

MODEL	A	B	C	D	E	F	G	H	I	J	K	N	P	Q
RV120	4.96 (126)	6.10 (155)	3.07 (78)	3.66 (93)	3.90 (99)	4.55 (115.5)	.55 (14)	3.39 (86)	3.15 (80)	2.48 (63)	1.34 (34)	.75 (19)	.16 (4)	.59 (15)
RV160	6.42 (163)	7.56 (192)	4.33 (110)	5.08 (129)	5.28 (134)	5.98 (152)	.55 (14)	3.50 (89)	3.86 (98)	3.21 (81.5)	1.42 (36)	.73 (18.5)	.20 (5)	.57 (14.5)
RV240	8.33 (237)	10.63 (275)	6.89 (175)	7.64 (194)	8.03 (204)	8.74 (222)	.63 (16)	3.66 (93)	5.22 (132.5)	4.79 (119.5)	1.58 (40)	.80 (20.3)	.28 (7)	.65 (16.6)
RV350	14.02 (356)	15.55 (395)	11.02 (280)	11.81 (302)	12.40 (315)	13.05 (331.5)	.69 (17.5)	4.25 (108)	7.44 (189)	7.05 (179)	1.97 (50)	.84 (21.3)	.31 (8)	.68 (17.3)

MODEL	R	S	T	U	V	W	X	Y	Z	a	b	c	α
RV120	4	M4	90°	3.44 (87.5)	.24 (6)	6	60°	5.39 (137)	5	M5	1	7	17.5°
RV160	6	M5	60°	4.72 (120)	.28 (7)	6	60°	6.85 (174)	5	M5	1	7	25°
RV240	6	M5	60°	7.38 (187.5)	.28 (7)	6	60°	9.84 (250)	5	M6	1	10	30°
RV350	6	M6	60°	11.61 (295)	.28 (7)	12	30°	14.65 (372)	10	M8	2	12	10°

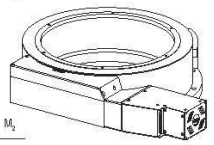

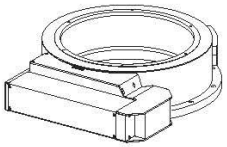

ROTATION STAGE, DIRECT MOTOR

MODEL	L_1 HAT	L_1 HAHLT	M_1	L_2	M_2
RV120	11.87 (301.5)	11.87 (301.5)	1.79 (45.5)		
RV160	12.36 (314)	14.06 (357)	2.13 (54)	4.61 (117)	1.32 (33.5)
RV240	13.35 (339)	15.04 (382)	2.89 (73.5)		
RV350	14.37 (365)	16.06 (408)	4.13 (105)		

ROTATION STAGE, FOLDED MOTOR

MODEL	L_1	M_1 HAT-F	M_1 HAHLT-F	L_2	M_2
RV120	6.12 (155.5)	2.15 (54.5)	3.13 (79.5)		
RV160	6.61 (168)	2.48 (63)	4.23 (107.5)	6.32 (160.5)	4.35 (110.5)
RV240	7.60 (193)	3.25 (82.5)	3.25 (82.5)		
RV350	8.62 (219)	4.49 (114)	4.49 (114)		

Ordering Information

Direct Motor Versions	Models				
Mini-step	RVS80PP	RV120PP	RV160PP	RV240PP	RV350PP
Full-step	–	RV120PE	RV160PE	RV240PE	RV350PE
Full-step & vacuum preparation	–	RV120PEV6	RV160PEV6	RV240PEV6	RV350PEV6
	Vacuum compatible to 10^{-6} hPa. In this case, max. speed and load capacity have to be divided by two.				
DC	RVS80CC	RV120CC	RV160CC	RV240CC	RV350CC
HAT: DC & integral optical encoder	–	RV120HAT	RV160HAT	RV240HAT	RV350HAT
CCHL: DC & gear reduction	–	RV120CCHL	RV160CCHL	RV240CCHL	RV350CCHL
HAHLT: CCHL version & integral optical encoder	–	RV120HAHLT	RV160HAHLT	RV240HAHLT	RV350HAHLT
Folded motor versions					
	Except RVS80, add -F for folded motor versions.				

Note: For higher capacity rotary stages, please call an Applications Engineer.

Accessories

Newport's EQ120 and EQ180 brackets (to order separately) are ideal for mounting our ILS or IMS Series of linear stages and RV80 to RV160 rotation stages for stable and stiff muti-axis positioning systems.

Model	Description
EQ120	Right-Angle Bracket for ILS and RV
EQ180	Right-Angle Bracket for IMS, RV120 and RV160

EQ180 bracket on an IMS stage, with an RV160 in vertical configuration.

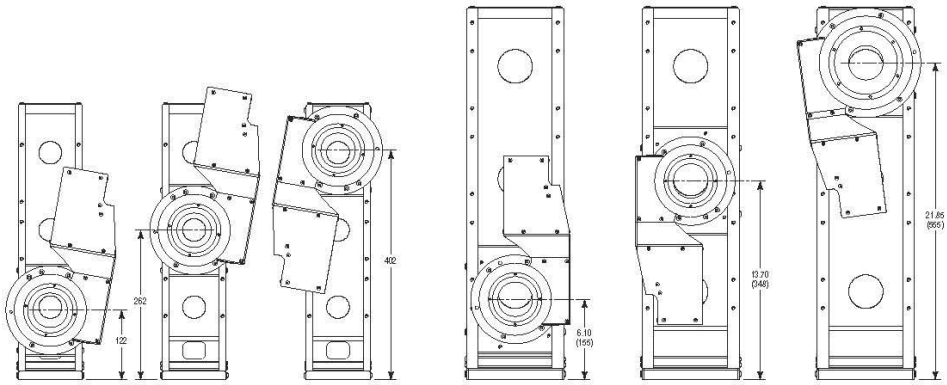

Newport Experience | Solutions

Newport Corporation, Global Headquarters
1791 Deere Avenue, Irvine, CA 92606, USA
www.newport.com
PHONE: 1-800-222-6440 1-949-863-3144 FAX: 1-949-253-1680 EMAIL: sales@newport.com
Complete listings for all global office locations are available online at www.newport.com/contact

	PHONE	EMAIL		PHONE	EMAIL
Belgium	+32-(0)0800-11 257	belgium@newport.com	Irvine, CA, USA	+1-800-222-6440	sales@newport.com
China	+86-10-6267-0065	china@newport.com	Netherlands	+31-(0)30 6592111	netherlands@newport.com
France	+33-(0)1-60-91-68-68	france@newport.com	United Kingdom	+44-1235-432-710	uk@newport.com
Japan	+81-3-3794-5511	spectra-physics@splasers.co.jp	Germany / Austria / Switzerland	+49-(0)6151-708-0	germany@newport.com
Taiwan	+886-(0)2-2508-4977	sales@newport.com.tw			

RV_DSE (10/13)

CURRICULUM VITAE

Name Surname **:** Ali Cem Ünal

Place and Date of Birth **:** İstanbul 13 JUNE 1989

E-Mail **:** alicemunal@yahoo.com

EDUCATION **:**

- **B.Sc.** **:** 2013, Isik University, Engineering Faculty, Mechanical engineering Department

PROFESSIONAL EXPERIENCE AND REWARDS:

- Student assistant at Isik University Mechanical Engineering Department from 2012 to 2013
- Research assistant at Isik University Mechanical Engineering Department from 2013 to 2016
- Mechanical engineer at Isik University Center of Optomechatronics Application and Research from 2016 to now on
- Certificate of honour for graduation from FMV Isik University at 2013
- Graduate ranking first in class from Bachelor Science
- Best Presentation Award at 2019 IEEE 10th International Conference on Mechanical and Aerospace Engineering (ICMAE)

PUBLICATIONS, PRESENTATIONS AND PATENTS ON THE THESIS:

- **Ali Cem Unal** 2018 In flange derotator design for the 4m DAG Telescope. 2018 SPIE. DOI:10.1117/12.2313912
- **Onur Keskin, Ali Cem Unal** Optical field derotator mounted on the Nasmyth flange with Piezo Actuators. Patent number: eu EP18020210.3
- **Onur Keskin, Ali Cem Unal** Optical field derotator mounted on the Nasmyth flange. Patent number: eu EP180202209.5

- **Onur Keskin, Ali Cem Unal** PCT/IB2019/054009

OTHER PUBLICATIONS, PRESENTATIONS AND PATENTS:

- **Ali Cem Unal** 2019 Adaptive Backstepping Approach for 2-DOF Telescopes Despite Unknown Wind Disturbance publication. 2019 IEEE 10th Inter- national Conference on Mechanical and Aerospace Engineering (ICMAE). DOI:10.1109/ICMAE.2019.8880967
- **Ali Cem Unal** 2019 Wind Disturbance Cancellation for Alt-Azimuth Telescopes. 2019 Astrorob (Presentation)
- **Onur Keskin, Ali Cem Unal** Modelling and Simulation studies on Adaptive Controller for Alt-Azimuth Telescopes Despite Unknown Wind Disturbance and Mass. *Advances in Mechanical Engineering*. DOI:10.1177/1687814020954767